

MASTER

Deconvolution of radiometric imaging data by means of spatial filter design

Lennartz, C.H.F.

Award date:
1995

[Link to publication](#)

Disclaimer

This document contains a student thesis (bachelor's or master's), as authored by a student at Eindhoven University of Technology. Student theses are made available in the TU/e repository upon obtaining the required degree. The grade received is not published on the document as presented in the repository. The required complexity or quality of research of student theses may vary by program, and the required minimum study period may vary in duration.

General rights

Copyright and moral rights for the publications made accessible in the public portal are retained by the authors and/or other copyright owners and it is a condition of accessing publications that users recognise and abide by the legal requirements associated with these rights.

- Users may download and print one copy of any publication from the public portal for the purpose of private study or research.
- You may not further distribute the material or use it for any profit-making activity or commercial gain

7026

**EINDHOVEN UNIVERSITY OF TECHNOLOGY
FACULTY OF ELECTRICAL ENGINEERING
TELECOMMUNICATIONS DIVISION**

*Deconvolution of radiometric imaging data
by means of spatial filter design*

by

C.H.F. Lennartz

Report of graduation work,
performed from November 1992 to August 1993.

Supervisors: *prof.dr.ir. G. Brussaard*
dr.ir. M.H.A.J. Herben
dr.ir. P.J.I. de Maagt

*The Faculty of Electrical Engineering of the Eindhoven University of Technology disclaims
all responsibility for the contents of training and graduation reports.*

Abstract

Microwave radiometry can be used to gather information about the sky brightness temperature distribution. The radiometer antenna however acts as a spatial low-pass filter resulting in resolution loss; moreover, the receiver adds noise to the image, so the output of the radiometer receiver will be a smoothed and noise-contaminated image of the object.

With knowledge of the antenna transfer function, the image can be deconvolved to obtain a better estimate of the brightness temperature. Since the antenna filtering process is nothing more than a spatial convolution, a filter (designed in the frequency domain) seems very promising.

The situation has been analyzed for a one-dimensional case. The objects that have been used were a deterministic worst-case example to test the algorithm's stability and a pseudo-random simulation of a cloudy sky, based on previous radiometer measurements.

The first conclusion that can be made is that without special extrapolation methods, object frequencies higher than the antenna cut-off frequency cannot be restored.

Simply inverting the antenna influence gives rise to very disturbing noise problems since the noise is treated as the image when the image frequency content is low.

The Wiener method is a statistical deconvolution method yielding a "smoothed" inverse filter. This technique leads to better results, especially when specific constraints are used. The Backus-Gilbert approach is practically the same method, but starting with a more specified criterion. Error analysis shows that noise still is the main evil in the pursuit of resolution enhancement and reconstruction accuracy. The proposed frequency-domain method appears to be equivalent with several matrix reconstruction techniques.

The realization of the Wiener filter into a FIR digital filter did not result in loss in deterioration of the algorithm's reconstruction quality.

The compromising part in this method is that the object-signal-to-receiver-noise ratio has to be known. This is a problem in cases where the interesting part of the signal is only present in a small interval (single-event cases); an adaptive filtering technique, which adapts the FIR filter to the received signal-to-noise ratio, proved to result in very accurate reconstructions.

An important conclusion that is reached is that increasing system resolution by increasing antenna size does not by definition lead to higher reconstruction accuracy, due to noise.

This feasibility study for one-dimension opens the way to a two-dimensional reconstruction technique to obtain enhanced real two-dimensional images.

Acknowledgements

The author wishes to thank prof.dr.ir. G. Brussaard for his fundamental guidance, dr.ir. M.H.A.J.Herben for his clarifying support and dr.ir. P.J.I. de Maagt for introducing me into the fascinating world of microwave imaging.

Contents

Chapter	Page
1. Introduction.	2
2. The radiometer imaging system.	5
3. Inverse filtering.	10
3.1. Definitions and assumptions.	10
3.2. Image forming and restoration.	12
3.3. Deconvolution using inverse filtering.	18
3.4. The possibility of bandwidth extrapolation.	22
4. Statistical filtering approach.	27
4.1. Wiener filter.	27
4.2. Sharpness-constrained Wiener filter.	37
4.3. Backus-Gilbert optimization approach.	40
4.4. Information aspect of optimum filtering.	44
5. Real time digital filter implementation.	46
5.1. Atmospheric brightness temperature simulation.	46
5.2. Infinite impulse response filtering.	52
5.3. Finite impulse response filtering.	58
5.4. The reconstruction error.	65
6. Adaptive filtering.	69
7. Conclusions and recommendations.	80
8. References.	83
Appendix A : Matrix technique analogy.	87
A.1. Minimum variance estimation.	87
A.2. Analogy with the De Maagt method.	90

Chapter 1

Introduction

Each and every object in the universe emits, absorbs and reflects radiation. The emitted and reflected radiation can be used to gain information about the object. Before the radiation can be detected though, it will have to pass through a medium, which is the atmosphere, by which it will be modified. The gathering of information from objects in the atmosphere by detecting the emitted and reflected radiation is called remote sensing.

The main distinction that can be made in remote sensing techniques is between passive and active remote sensing, dependent of whether the radiation received finds its origin in self-emission (noise) or it originates from reflection of radiation at the object from an artificial source (radar).

Passive remote sensing can be very useful in evaluating the performance of a future satellite link at higher frequency bands (i.e. 20 and 30 GHz). The atmospheric attenuation at these frequencies will limit the availability of the link. Setting up a link to study this attenuation is an expensive tool, which is not necessary when the sky brightness temperature, which can be measured by a passive remote sensing system, gives good insight into atmospheric attenuation. The common and most powerful tool for this is *microwave radiometry*.

The benefit of using microwaves in remote sensing is their ability to penetrate through clouds and rain.

The temporal variations of the antenna noise temperature can be translated into variations of the attenuation and thus into cumulative statistics to predict the performance of a future satellite link. The variations of the noise temperature also give information about the shape of an object when this object moves through the beam of the radiometer antenna. The disadvantage of the use of microwaves here is the fact that their wavelength is much larger than infrared or visible wavelengths which leads to an inherent lower spatial resolution. Recent methods have shown, however, that for a range of

applications spatial resolution in the order of the physical dimensions of the object can be obtained, opening the door for applications of microwave radiometry.

The determination of the spatial characteristics of an object using its radiative characteristics is called *microwave imaging*. As already stated, the radiometer antenna noise temperature tracks the sky brightness temperature when the object moves through the antenna pattern. It is assumed that the scene is frozen, i.e. that the shape of the object does not alter during the transition through the antenna beam.

The radiometer, consisting of the receiving antenna and the radiometer receiver, produces an output which is proportional to the antenna noise temperature. The antenna however acts as a spatial low-pass filter because of the not finite width of the main lobe of the antenna gain function and its non-zero sidelobes. A very striking property is that this low-pass character is very abrupt: the antenna transfer function drops very quickly and above a certain spatial frequency can be considered negligible. Highly fluctuating details in the brightness temperature can therefore not be followed and final resolution is limited to the antenna resolution. The goal of the imaging system is to obtain detailed information about the object without the necessity of very large antennas.

When the scene moves through the antenna beam, the antenna noise temperature is nothing but a convolution of the antenna gain function and the sky brightness temperature. Reconstruction of the object, intuitively speaking, is then simply the inversion of the convolution process, deconvolution. The problem, though, is the noise added to the radiometer signal. The reconstruction using the pure inverse process is called inverse filtering, but this method leads to serious blurring of the reconstruction because the inverting process amplifies the noise for the frequencies that were strongly attenuated by the antenna, because they have to be amplified in order to gain resolution.

This report deals with this deconvolution process of radiometric image data. The ultimate goal of the deconvolution analysis is to dispose of a ground-based or space-borne imaging radiometer with an on-board real-time two-dimensional DSP deconvolution filter to make atmosphere and earth observations. That goal is still a long way from here, but the analysis in one dimension is not far from being complete.

The principle of the imaging system will be analyzed in Chapter 2, translating the antenna noise temperature equation to a two-dimensional convolution. To gain clearer insight into fundamentals of the deconvolution, it is assumed that the brightness temperature is only one-dimensionally varying so the problem is restricted to one dimension.

Convolution calls for Fourier analysis. Therefore deconvolution is firstly analyzed in the Fourier domain, assuming infinite time series to account for Fourier transformations. Pure inverse filtering is treated in Chapter 3, to indicate that this intuitive method will not be the best. The object to be restored is chosen to be a worst-case situation with discontinuities which have caused most

reconstruction methods to fail completely.

The main limitation is that frequencies beyond the above-mentioned cut-off frequency cannot be regained in principle, because they are simply not present. There are methods however to reconstruct these frequencies, using bandwidth extrapolation methods. These will be treated at the end of the inverse filtering treatment.

Chapter 4 analyzes the deconvolution in a statistical way. Several methods to minimize the reconstruction error are presented and illustrated. The basic method leads to a filter called the *Wiener filter*, which is encountered every time a minimum mean-square estimation is discussed. Therefore the link will be laid to other techniques, using a finite time series matrix approach, which lead to comparable results.

When the object is hard to reconstruct, for example because it has sharp edges, constraints have to be met in the criterion on which the reconstruction is based. Sharpness control is a constraint that is handled together with the pure Wiener filtering.

A comparable method which uses a more specified criterion is the *Backus-Gilbert* approach, allowing the user to make a trade-off between resolution and noise suppression.

At the end of the chapter the noticeable relation between the optimum mean-square filter and an information theory approach of image data is indicated.

The treatment of the real-time processing starts in Chapter 5. Firstly, a new scene is generated that agrees with radiometer measurements performed on cloudy skies, after worst-case analysis had been done. The Fourier-domain designed reconstruction filter is then transformed into a digital filter, having two possible realizations, Infinite Impulse Response filters or Finite Impulse Response filters. Benefits and drawbacks of both methods will be investigated.

The major disadvantage of all the above-mentioned methods is that a-priori knowledge of the object to be restored or estimation of it is necessary to design the filter. This problem can be partly solved by performing the reconstruction adaptively. This is done in Chapter 6.

Conclusions and recommendations for further, two-dimensional study are presented in the last chapter.

Chapter 2

The Radiometer Imaging System.

The radiometer imaging system is nothing but a scanning antenna pointed at the so-called *object* that is to be observed. If the sky brightness temperature spatial distribution is to be monitored, the radiometer antenna is pointed towards the sky. If the scene moves with known velocity in a certain direction, the scanning can be reduced to the direction perpendicular to the object movement to achieve a two-dimensional scan.

The output of the imaging system is the *image*, the antenna noise temperature, and its relation to the original object is given by the following relation:

$$T_A = \frac{1}{4\pi} \int_{4\pi} T(\Omega) G(\Omega) d\Omega \quad (2.1)$$

where T_A is the antenna noise temperature, $T(\Omega)$ the brightness temperature distribution of the object and $G(\Omega)$ the antenna radiation pattern.

The object is usually described in a Cartesian coordinate system, while antenna system quantities and relations are usually defined in a spherical coordinate system, so Eq.(2.1) has to be transformed. Figure 2.1 on the next page depicts the antenna configuration and the object and image configuration.

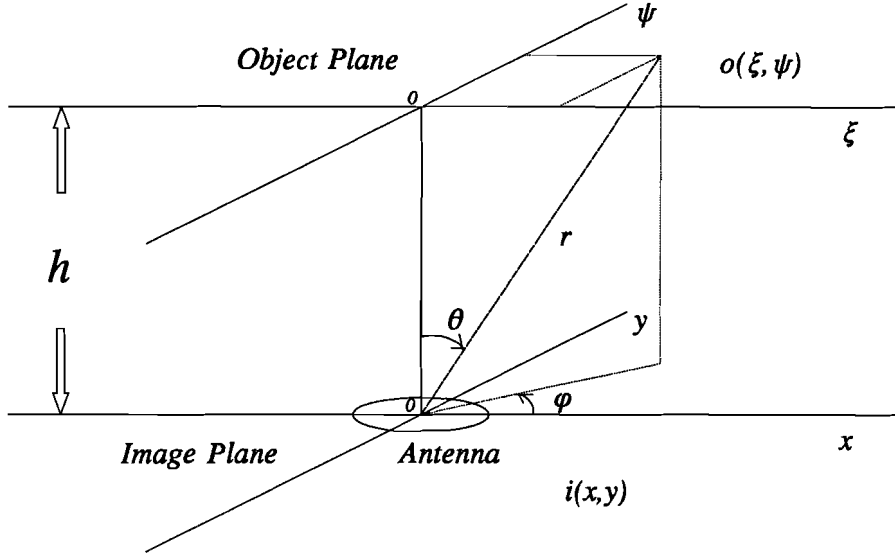


Figure 2.1 : The system configuration.

The angles θ and φ have to be transformed to the Cartesian coordinates ξ and ψ to obtain the antenna radiation pattern "footprint" in the object plane. It is reasonable to assume that the antenna used has a rotationally symmetric radiation pattern, so it is only dependent of θ .

From Figure 2.1 the following relation can be obtained:

$$\sin \theta = \sqrt{\frac{\xi^2 + \psi^2}{\xi^2 + \psi^2 + h^2}} \approx \frac{1}{h} \sqrt{\xi^2 + \psi^2} \quad \text{and} \quad \sin(\varphi) = \frac{\psi}{\sqrt{\psi^2 + \xi^2}} \quad (2.2)$$

The approximation can be made since the beamwidth of the antenna will be very small compared to the altitude h of the object.

The antenna pattern used for this feasibility study will be the pattern of a uniformly illuminated parabolic reflector antenna which can be modeled adequately by the following equation:

$$G(\theta) = 4 \left(\frac{\pi D}{\lambda} \right)^2 \left(\frac{J_1(u)}{u} \right)^2 \quad (2.3)$$

In this equation $J_1(u)$ is the first order Bessel function of the first kind and its argument u equals

$$u = \frac{\pi D}{\lambda} \sin \theta \quad (2.4)$$

where D is the diameter of the reflector and λ is the wavelength.

Combining equations (2.2), (2.3) and (2.4) will lead to the antenna radiation pattern as a function of the object-plane coordinates, depicted in figure 2.2.

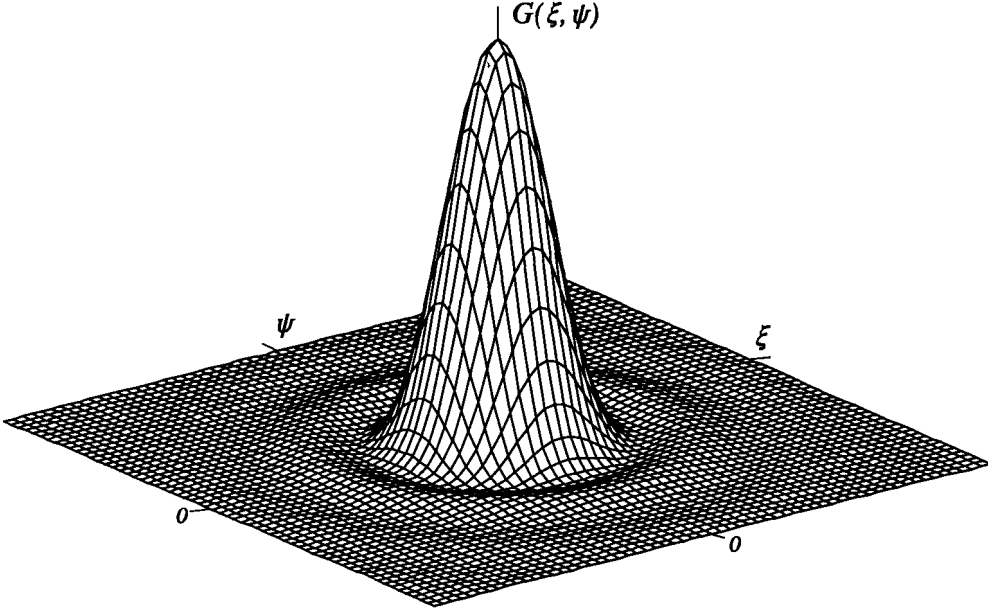


Figure 2.2 : The antenna radiation pattern in the object plane.

In the spherical coordinate system the solid angle $d\Omega$ equals dA/r^2 in which dA can be approximated by $d\xi d\psi$ in the object plane and $r^2 = \xi^2 + \psi^2 + h^2 \approx h^2$ (for the same reason as in Eq.(2.2)).

With these approximations, Eq(1.1) is transformed to the Carthesian coordinate system as follows:

$$T_A = \int_{-\infty}^{\infty} \int_{-\infty}^{\infty} T(\xi, \psi) \frac{G(\xi, \psi)}{4\pi h^2} d\xi d\psi \quad (2.5)$$

In the sky-observing case the scene moves, so T_A will be a function of time. If the object moves in the object plane with its drift velocity, supposing a non-moving antenna, it is of course exactly the same situation as if the antenna is moved along the image plane in the opposite direction but with the same velocity as the sky scene, supposing a non-moving object. Therefore the object is observed at a position (x, y) in the image plane.

From Figure 2.1 and Eq.(2.5) it can be seen that at position (x, y) the image distribution is modeled by:

$$T_A(x, y) = \int_{-\infty}^{\infty} \int_{-\infty}^{\infty} T(\xi + x, \psi + y) \frac{G(\xi, \psi)}{4\pi h^2} d\xi d\psi \quad (2.6)$$

Apparently the antenna noise temperature is the convolution of the sky brightness temperature and

the antenna radiation pattern, like in every imaging system [5,14,21,25,28]

The generally used form of convolution can be obtained by rearranging the arguments in the integrand:

$$T_A(x,y) = \int_{-\infty}^{\infty} \int_{-\infty}^{\infty} T(\xi,\psi) \frac{G(x-\xi,y-\psi)}{4\pi h^2} d\xi d\psi \quad (2.7)$$

Apparently, the antenna is a spatial filter and Fourier analysis and filtering will be a very suitable method to handle imaging problems.

In this study the imaging system will be analyzed as if the sky brightness temperature would only vary in one direction, ξ , to facilitate understanding of the fundamentals of the filtering approach.

The expression for the antenna noise temperature (2.7) will then change as follows:

$$T_A(x) = \int_{-\infty}^{\infty} T(\xi) G'(x-\xi) d\xi \quad (2.8)$$

The new one-dimensional radiation pattern $G'(\xi)$ is the integrated two-dimensional radiation pattern $G(\xi,\psi)$:

$$G'(\xi) = \int_{-\infty}^{\infty} \frac{G(\xi,\psi)}{4\pi h^2} d\psi \quad (2.9)$$

The aim is to have as much resolution as possible with an antenna as small as possible. The following parameters have been used to model the system:

- The diameter of the antenna D is 1 meter.
- The frequency used is 30 GHz, so the wavelength λ is 0.01 meter.
- The height h of the object plane is 1 km.

With these values, the radiation pattern $G'(\xi)$, or the imaging filter impulse response, will be as depicted in figures 2.3 (normalized, in dB's) and 2.4 on the next page. The high altitude of the object causes the pattern to have such low values.

As expected, the integrated radiation pattern is a smoothed version of the two-dimensional radiation pattern.

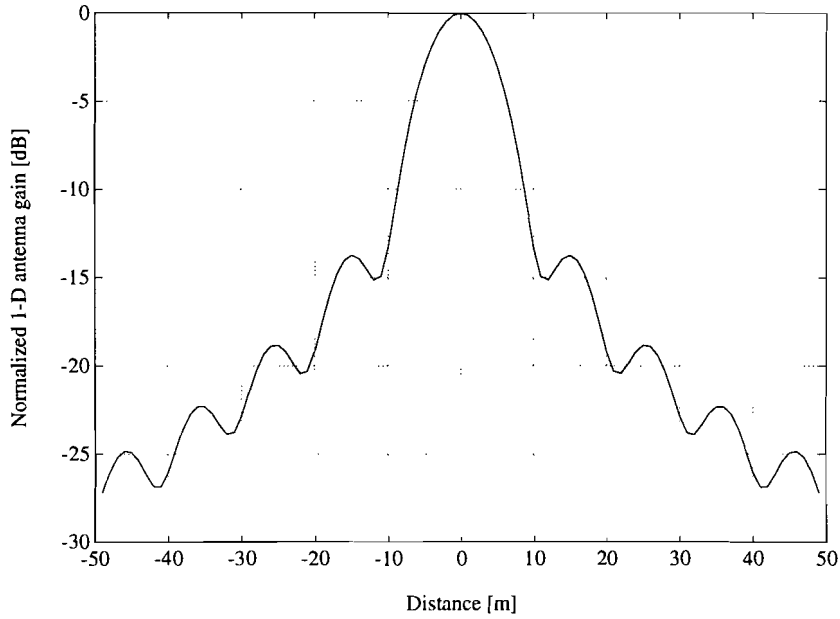


Figure 2.3 : *The integrated radiation pattern.*

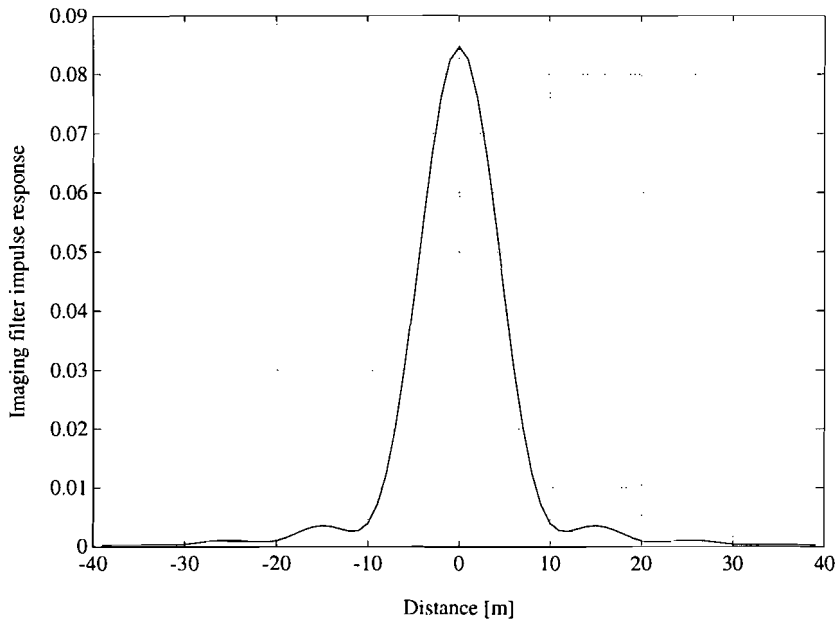


Figure 2.4 : *The imaging filter impulse response.*

The problem with this configuration is that the altitude h of the object has to be known to calculate the radiation pattern as a function of the Cartesian coordinates ξ and ψ , and the velocity of the object to convert the received antenna noise temperature as a function of time to a function of spatial coordinates. This can be solved by defining the object and image in a spherical coordinate system, i.e. as if the object would move over the surface of a sphere. In this study the Cartesian coordinate system is applied because its visualization is clearer and thus will not be hindering in gaining insight in the spatial filtering fundamentals.

Chapter 3

Inverse Filtering

The first method that comes to mind to undo the effect of the imaging filter is to invert the antenna influence so that the overall result will be unchanged.

This simple intuitive method is called *inverse filtering* and it can be done in many ways. This chapter will deal with the frequency domain approach of inverse filtering in the restoration of a band-limited image. This limited bandwidth together with the presence of receiver-added noise will appear to be the bottleneck in performing the reconstruction with as much accuracy as possible.

At the end of the chapter it will be discussed how the problem of bandwidth limitation can be overcome.

But first some definitions and an introduction are presented.

3.1 Definitions and assumptions.

The transformation of a signal $g(x)$ into the (spatial) frequency domain is the Fourier transform

$$G(\omega) = \int_{-\infty}^{\infty} g(x) \exp(-j\omega x) dx \quad (3.1)$$

And the inverse transform is given by

$$g(x) = \frac{1}{2\pi} \int_{-\infty}^{\infty} G(\omega) \exp(j\omega x) d\omega \quad (3.2)$$

The radial frequency ω , in rad/m, and the repetition frequency f , in 1/m, of which the relation is $\omega = 2\pi f$, will both be used, whichever is more convenient.

In case of a stochastic signal, the power spectrum of the signal is given by the ensemble average of the squared modulus of the Fourier transform of all possible realizations [14]:

$$\Phi(\omega) = \langle |G(\omega)|^2 \rangle \quad (3.3)$$

In this chapter it will be assumed that all signals are random, stationary, ergodic, and their measurement series are infinite, so continuous Fourier spectral analysis will be justified.

The following definitions are used [14]:

$$\text{Rect}(x/a) = \begin{cases} 1 & \text{for } |x| \leq a \\ 0 & \text{for } |x| > a \end{cases} \quad (3.4)$$

and

$$\text{sinc}(x) = \frac{\sin x}{x} \quad (3.5)$$

The relationship between the two is that the Fourier transform of $\text{Rect}(x/a)$ is $2a \text{sinc}(\omega a)$.

If the signal is bandlimited, i.e. $F(\omega) = 0$ for $|\omega| > \Omega$, then the following relations are valid:

$$g(x) = \sum_{n=-\infty}^{\infty} g\left(\frac{n\pi}{\Omega}\right) \text{sinc}(\Omega x - n\pi) \quad (3.6)$$

$$G(\omega) = \frac{\pi}{\Omega} \sum_{n=-\infty}^{\infty} g\left(\frac{n\pi}{\Omega}\right) \exp(-jn\pi \frac{\omega}{\Omega}) \quad (3.7)$$

Equation (2.6) is sometimes called the "perfect interpolation formula": if only a set of samples spaced by π/Ω are known, the whole signal can be reconstructed.

3.2 Image forming and restoration.

When an imaging radiometer is used, the two quantities that have to be considered are the sky brightness temperature and the antenna noise temperature.

A possible (but not likely) realization of the object is depicted in figure 3.1.

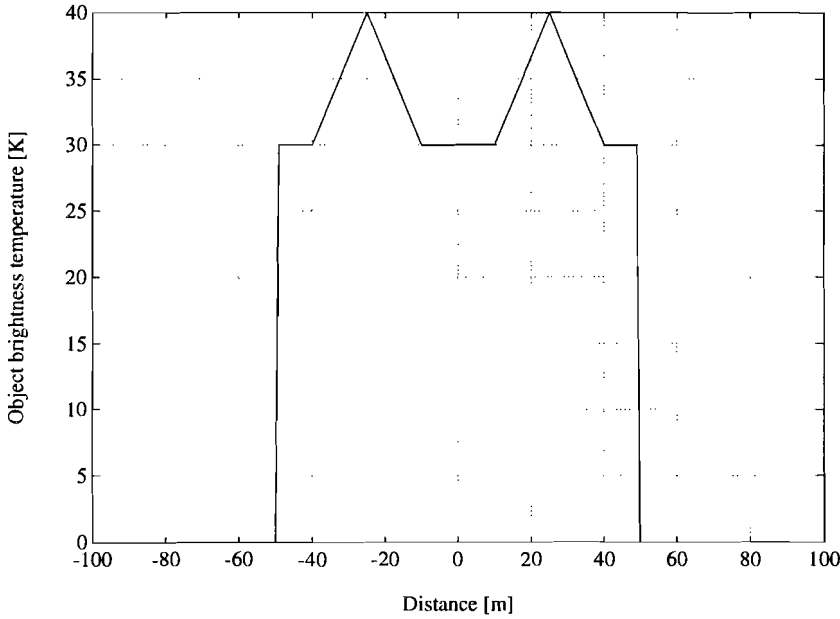


Figure 3.1 : *The object brightness temperature.*

This signal is defined from -1024 m to 1024 m with a sample distance of 1 m, but is only shown for a small area, because the object is assumed zero outside.

This kind of object represents the worst case for reconstruction algorithms because of its discontinuities, so it will be a good test for the spatial filtering technique.

The 2048 point Fast Fourier Transform of this signal is shown in figure 3.2 on the next page.

In this example and in all the examples to follow, a sampling spatial distance of 1 m and a sampling frequency distance of $1/2048 \text{ m}^{-1}$ in the spatial frequency domain is used.

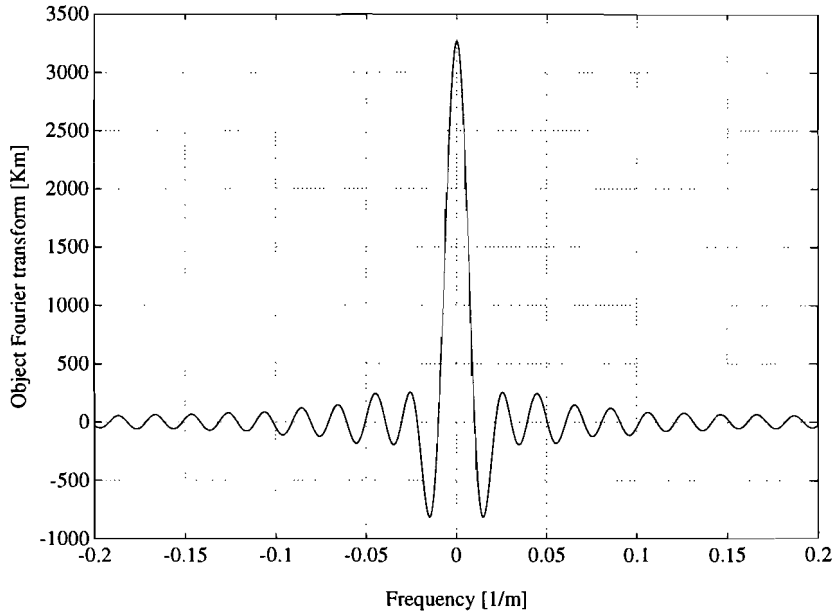


Figure 3.2 : The Fourier transform of the object.

The relation between the sky brightness scene and the antenna noise temperature is a convolution according to Chapter 2. The radiometer receiver adds noise to the convolved signal, which will be the main problem in the image restoration.

The sky brightness temperature, the *object*, will from now on be denoted with $o(x)$, the one-dimensional antenna diagram with $s(x)$, also called the *point spread function* or imaging impulse response, and the antenna noise temperature, the *image*, with $i(x)$. The noise is represented by $n(x)$ and the reconstruction, i.e. the estimate of the object by $\hat{o}(x)$. The total imaging system will then look like depicted in figure 3.3.

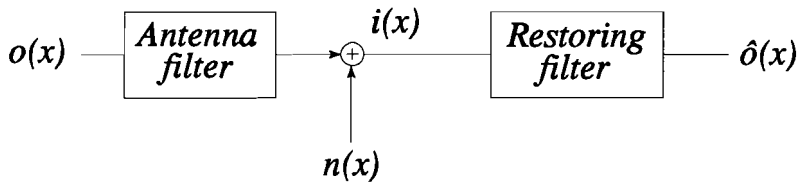


Figure 3.3 : The imaging system.

The image forming is then described as follows:

$$i(x) = \int_{-\infty}^{\infty} o(\xi)s(x-\xi)d\xi + n(x) \quad (3.8)$$

As already stated, this convolution relation lends itself perfectly for spectral analysis, because it leads to multiplication in the frequency domain:

$$I(\omega) = O(\omega)S(\omega) + N(\omega) \quad (3.9)$$

In this equation, $S(\omega)$ is the Fourier transform of the point spread function $s(x)$, which in this model equals $G'(x)$, the one-dimensionally integrated antenna radiation pattern $G(x,y)$.

When the model antenna discussed in Chapter 2 (figures 2.3 and 2.4) is assumed, this Fourier transform will look like illustrated in figure 3.4.

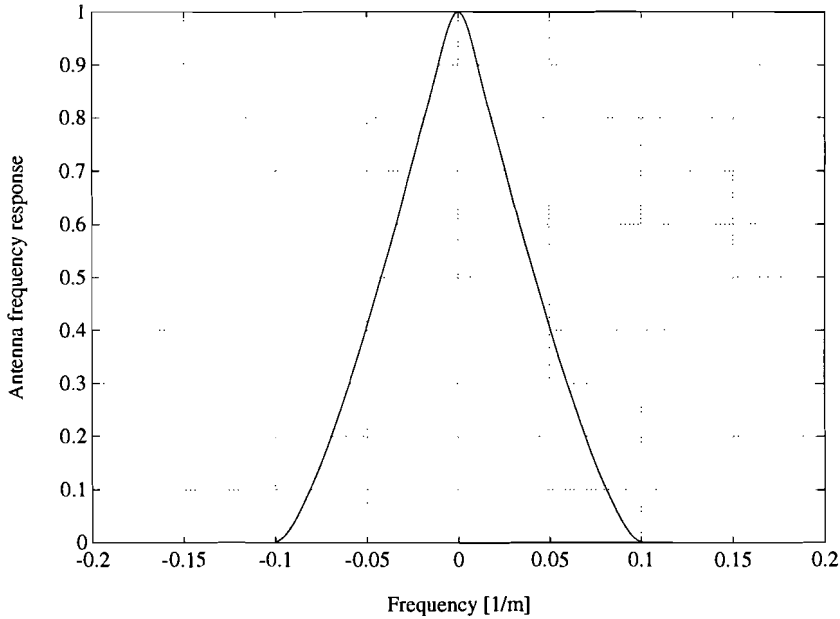


Figure 3.4 : The antenna frequency transfer function.

It is not surprising that the DC transfer is unity, since the antenna noise temperature equals the sky brightness temperature when the latter is uniformly distributed over the sky's surface.

An interesting feature of this antenna is the sharp transition at 0.1 m^{-1} ; it seems as if all frequency components above this frequency are zero, but the truth is that they are negligibly small.

To evaluate this feature deeper, the antenna transfer function is depicted in dB's in figure 3.5 on the next page.

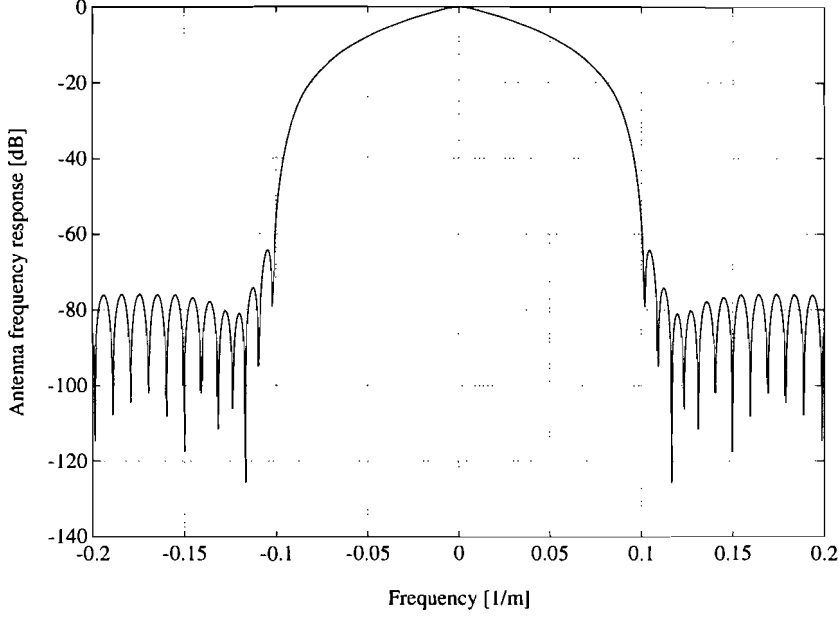


Figure 3.5 : The antenna frequency response in dB's.

Beyond 0.1 m^{-1} sidelobes appear with a level of almost -80 dB. Therefore, this frequency can be defined as the *cut-off frequency* f_c of the antenna filter.

This cut-off frequency appears to equal $D/\lambda h$, which is just the inverse 3 dB beamwidth of the antenna, which is λ/D , divided by the object altitude h .

The receiver-added noise is assumed to be Gaussian distributed white noise with a variance of 0.25 K^2 , equivalent to a radiometer detection error of 0.5 K .

The object is defined only in a strictly finite time interval, so it would not be correct to talk about *power* signals, which are infinitely long time series.

The energy of a time-limited signal (from $-X/2$ to $X/2$) is given by

$$E = \int_{-X/2}^{X/2} |o(x)|^2 dx \quad (3.10)$$

while the power of an infinite series is the limit

$$P = \lim_{X \rightarrow \infty} \frac{1}{X} \int_{-X/2}^{X/2} |o_X(x)|^2 dx \quad (3.11)$$

where $o_X(x)$ is a truncated form of the signal $o(x)$, if this were a power signal.

Thus, the *energy spectral density* of the signal in the regarded time-interval is to be used. The energy spectral density of a signal like $o(x)$ is just the squared modulus of its Fourier transform $|O(f)|^2$ according to Parseval's theorem [28] while the *power spectral density* is given by the limit

$$\lim_{X \rightarrow \infty} \frac{|O_x(f)|^2}{X} \quad (3.12)$$

This equation is the same as Eq.(3.3). This limit is necessary because the Fourier transform of an infinite signal diverges in general.

The noise, however, is an infinite time series, so the power concept can be applied there. Still we can talk about the energy of this noise in the regarded (spatial) interval. This noise energy content is then $0.25X \text{ K}^2\text{m}$, in which X is the interval regarded. In principle, this interval is 2048 m, because this comprises the whole (simulated) measurement series. In the rest of this case, when a signal-to-noise ratio will be calculated, it will be the *energy* signal-to-noise ratio.

An interesting point of discussion is the interval to be regarded because this kind of single-event cases where the interesting part of the object is of limited spatial extent whereas outside the event there is only very low or (in this case) zero signal content. If for example the whole interval of 2048 m is chosen the SNR will be approximately 20 times (13 dB) lower than when the event-interval from $x=-50 \text{ m}$ to $x=50 \text{ m}$ is used. The SNR is an important parameter in the reconstruction analysis and the reconstruction quality should not be affected by the interval chosen. When the signal would be present over the whole measurement interval, this problem would not occur.

The signal-to-noise ratio in this case will be chosen to be calculated for the interval $[-50 \text{ m}, 50\text{m}]$, so X will be 100.

The object energy in this interval is $1.1 \cdot 10^5 \text{ K}^2\text{m}$ (for this case it will be the same for every larger interval), which corresponds to a power (energy averaged over the interval) of $1.1 \cdot 10^3 \text{ K}^2$.

The noise power of 0.25 K^2 is independent of the interval chosen but its energy is not of course; this noise energy is $25 \text{ K}^2\text{m}$. The signal-to-noise ratio is then calculated to be 36 dB.

The image $i(x)$ is created by Eq.(3.8) i.e. Eq.(3.9) in the frequency domain, and the result is shown in figure 3.6.

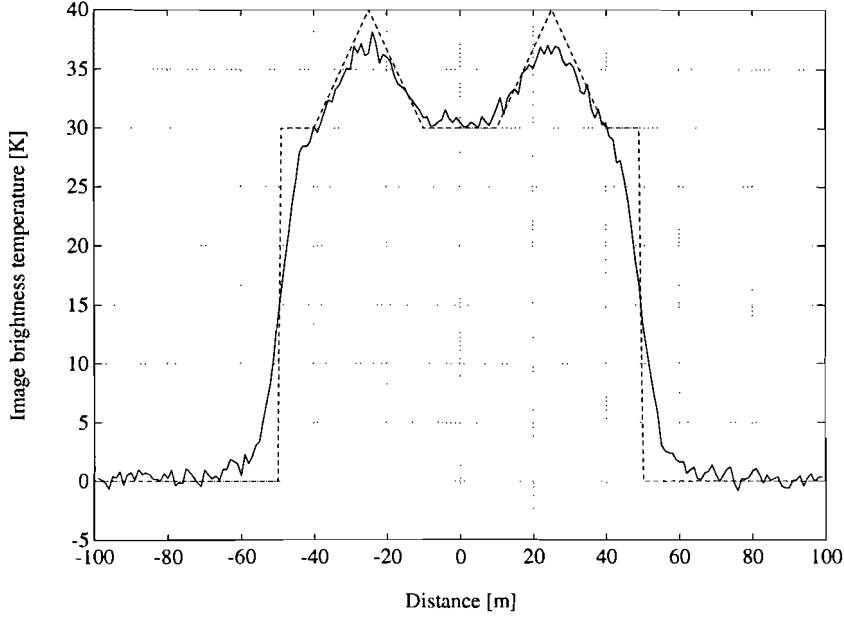


Figure 3.6 : The received image (---- object, — image)

A restoring filter $Y(\omega)$ is used to compensate the effects of the point spread function and to create the estimate $\hat{o}(x)$ of the object $o(x)$:

$$\hat{O}(\omega) = Y(\omega)I(\omega) = Y(\omega)S(\omega)O(\omega) + Y(\omega)N(\omega) \quad (3.13)$$

The overall "image blurring" filter is defined as

$$S_{net}(\omega) = S(\omega)Y(\omega) \quad (3.14)$$

Thus, the overall point spread function satisfies the following equation:

$$s_{net}(x) = \frac{1}{2\pi} \int_{-\infty}^{\infty} S(\omega)Y(\omega) \exp(j\omega x) d\omega \quad (3.15)$$

The *resolution distance* will be defined as the x-coordinate of the first zero of the overall point spread function [14].

Resolution can be defined in many ways, but since the overall point spread function usually closely resembles a sinc function, its zeros are a good measure for resolution.

The relation between the signal part of the estimate and the image is then as follows:

$$\hat{o}(x) = \int_{-\infty}^{\infty} o(\xi) s_{net}(x - \xi) d\xi \quad (3.16)$$

Obviously, the reconstruction would be ideal if $s_{net}(x)$ would be the delta function, since its first zero is then at zero so its resolution is infinitely small.

The question is, what is the resolution improvement that can be obtained using a restoring filter?

The imaging filter in practice cuts off all information above a certain frequency $\Omega = 2\pi f_c$ as discussed before, which means that all information beyond cut-off is lost, unless extrapolating methods will be used, so the best that can be done to save high-frequency components in terms of resolution is to generate a rectangular overall transfer function from $-\Omega$ to Ω . The net point spread function is then proportional to $\text{sinc}(\Omega x)$ of which the resolution distance is π/Ω .

The transfer function of the modelled imaging system is almost triangular from $-\Omega$ to Ω , according to figure 3.4, which means a convolution of two rectangular functions from $-\Omega/2$ to $\Omega/2$, so the point spread function will be proportional to $\text{sinc}^2(\Omega x/2)$ with a resolution distance of $2\pi/\Omega$. This means that the maximum resolution gain will be 2. This can also be seen by the fact that the effective bandwidth of the triangle is doubled from $\Omega/2$ to Ω by inverse filtering.

In the presence of noise this gain will be less than two due to the necessity of a lower cut-off frequency (see the next section).

This argumentation can be continued of course to for example the convolution of two triangular filters to a "parabolic" filter from $-\Omega$ to Ω . Its resolution will then be $4\pi/\Omega$, a gain factor of 4.

Generally speaking can be concluded that the resolution gain factor is dependent of the way in which high-frequency components are attenuated; still, a better resolution than π/Ω cannot be attained.

3.3 Deconvolution using inverse filtering.

Maximum resolution can, intuitively, speaking be reached when the overall transfer function is rectangular which will be the case when *inverse filtering* is applied. The imaging filter $Y(\omega)$ will then satisfy the following expression:

$$Y(\omega) = \text{Rect}(\omega/\Omega_p) \frac{1}{S(\omega)} \quad (3.17)$$

Since the transfer function $S(\omega)$ is usually zero or very small beyond a certain cut-off frequency Ω $Y(\omega)$ will be undefined for those frequencies or the noise will be very strongly amplified. Therefore the $Y(\omega)$ will be cut off above a suitably chosen frequency $\Omega_p < \Omega$.

The overall transfer function will then be equal to unity below cutoff and zero elsewhere, leading to $s_{net}(x) = 2\Omega_p \text{sinc}(\Omega_p x)$. The resolution distance is then π/Ω_p which will always be larger than the desired maximum π/Ω .

Apparently, the higher Ω_p , the higher the resolution, but the higher the noise amplification for frequencies near Ω , so a trade-off between resolution and accuracy becomes unavoidable.

This trade-off can be optimized by choosing an appropriate Ω_p . For this purpose, $e(x)$ is defined as the error between the object and its estimate:

$$e(x) = o(x) - \hat{o}(x) = \frac{1}{2\pi} \int_{-\infty}^{\infty} O(\omega) \exp(j\omega x) d\omega - \frac{1}{2\pi} \int_{-\Omega_p}^{\Omega_p} \left[O(\omega) + \frac{N(\omega)}{S(\omega)} \right] \exp(j\omega x) d\omega \quad (3.18)$$

The optimum Ω_p is chosen to minimize the mean squared error ϵ^2 :

$$\epsilon^2 = \left\langle \int_{-\infty}^{\infty} |e(x)|^2 dx \right\rangle \quad (3.19)$$

Substituting Eq.(3.18) in Eq.(3.19), assuming no correlation between object and noise, yields:

$$\epsilon^2 = 2 \int_{\Omega_p}^{\infty} \Phi_o(\omega) d\omega + 2 \int_0^{\Omega_p} \frac{\Phi_n(\omega)}{|S(\omega)|^2} d\omega \quad (3.20)$$

In this equation, $\Phi_o(\omega)$ and $\Phi_n(\omega)$ are the spectral densities of the object and the noise, respectively, according to expression (3.3).

It is obvious from (3.20) that the error is caused by the signal power outside the filtering band and the filtered noise power inside this band.

Differentiation of the mean squared error to Ω_p and setting the result to zero leads to:

$$\Phi_n(\Omega_p) = |S(\Omega_p)|^2 \Phi_o(\Omega_p) \Rightarrow |S(\Omega_p)|^2 = \frac{\Phi_n(\Omega_p)}{\Phi_o(\Omega_p)} \quad (3.21)$$

In words, the optimum cut-off frequency is the frequency for which the object spectral density after the antenna filtering equals the noise spectral density. This object spectral density can drop rather quickly due to the filter transfer $S(\omega)$, so the higher the noise spectral density the lower the intercept with the filtered object spectrum, the lower the cut-off frequency.

The problem of course is that the spectral densities are not exactly known. A good approximation can be obtained, however, by previous statistical observations, for example from other radiometer systems.

An approximation that is usually made is that the spectral signal-to-noise ratio in Eq.(3.21) is replaced by the overall signal-to-noise ratio, which means that below cut-off the object spectrum is considered white.

The inverse filtering principle will now be applied to the image of figure 3.6
The calculated inverse filter is illustrated in figure 3.7.

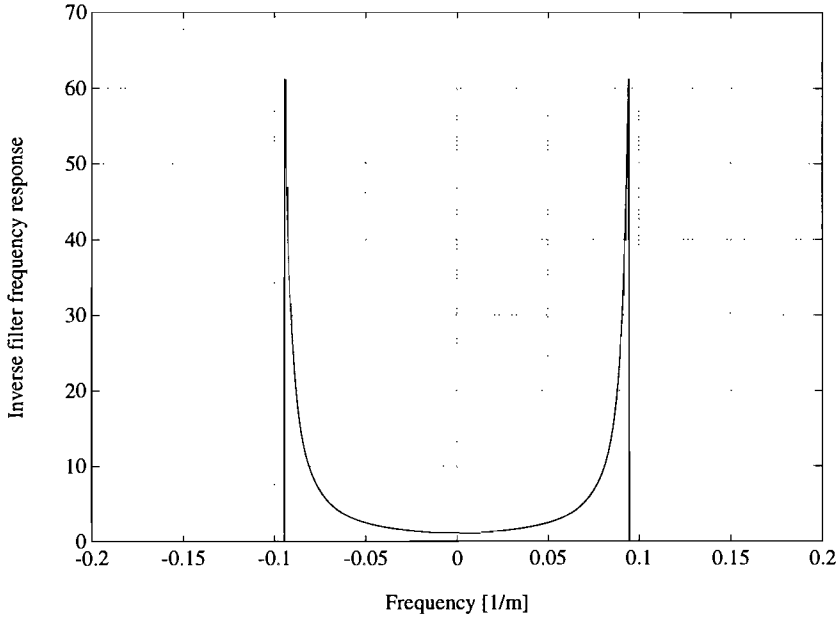


Figure 3.7 : *The inverse filter.*

The height of the peaks at Ω_p is \sqrt{snr} according to Eqs.(3.17) and (3.21).

When this filter is used to restore the object, its output will be as shown in figure 3.8 on the next page.

The reconstructed image is very blurred. This is caused both by the fact that the abrupt transition at Ω_p introduces the sidelobe effects of the corresponding sinc-function and the noise amplification due to the peaks of the inverse filter at Ω_p .

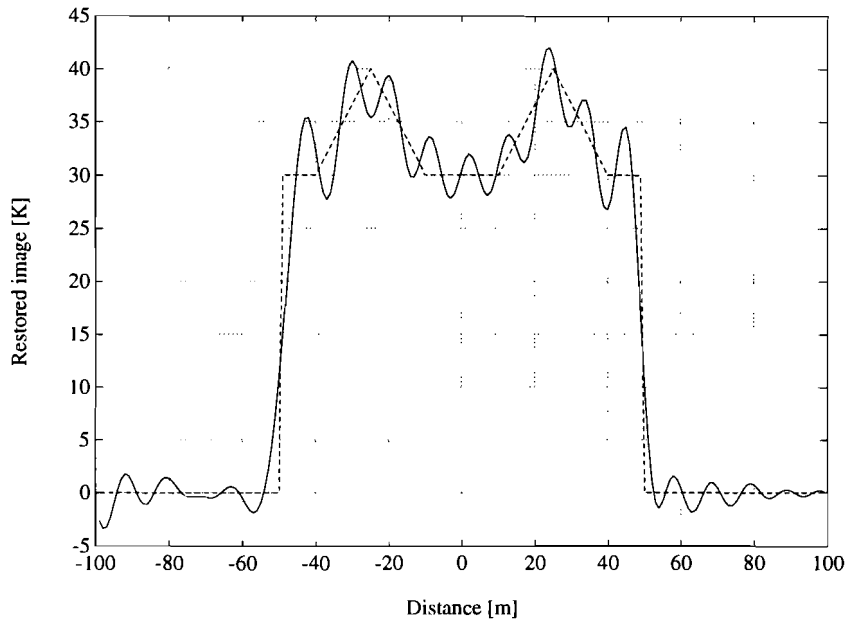


Figure 3.8 : The restored image using inverse filtering (---- object, — restoration).

The peaks are extremely high so it will be better to adapt (in this case, lower) the signal-to-noise ratio. When for example the whole measurement interval of 2048 m would be regarded, an *average* signal-to-noise ratio (averaged between the event area SNR of 36 dB and the non-event area which is only specified by a noise variance of 0.25 K^2) can be used, which actually takes into account that there is no signal but only noise outside the event.

This SNR will be 23 dB, exactly the beforementioned decrease of 13 dB.

The inverse filter based on this SNR is shown in figure 3.9

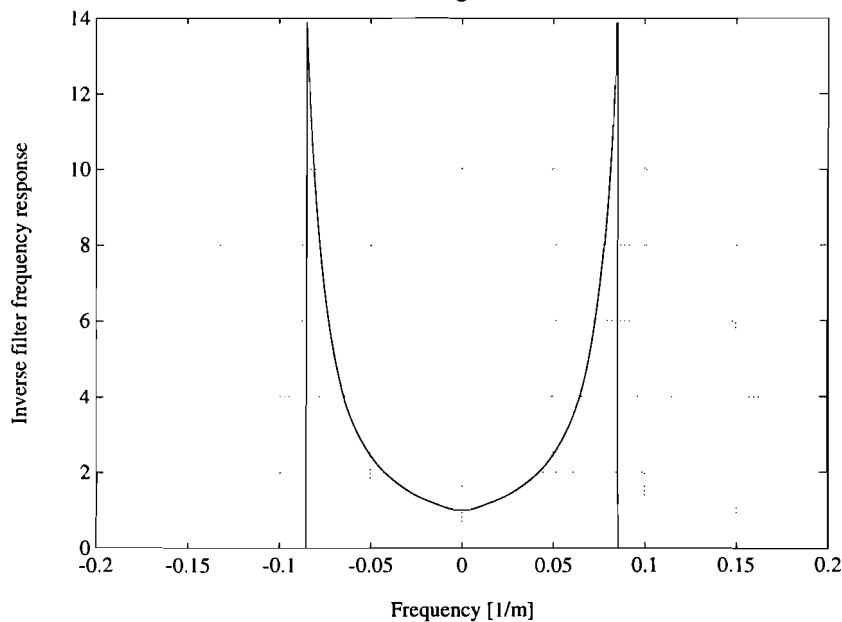


Figure 3.9 : The inverse filter for a SNR of 23 dB.

The result of the restoration based on this inverse filter is illustrated in figure 3.10.

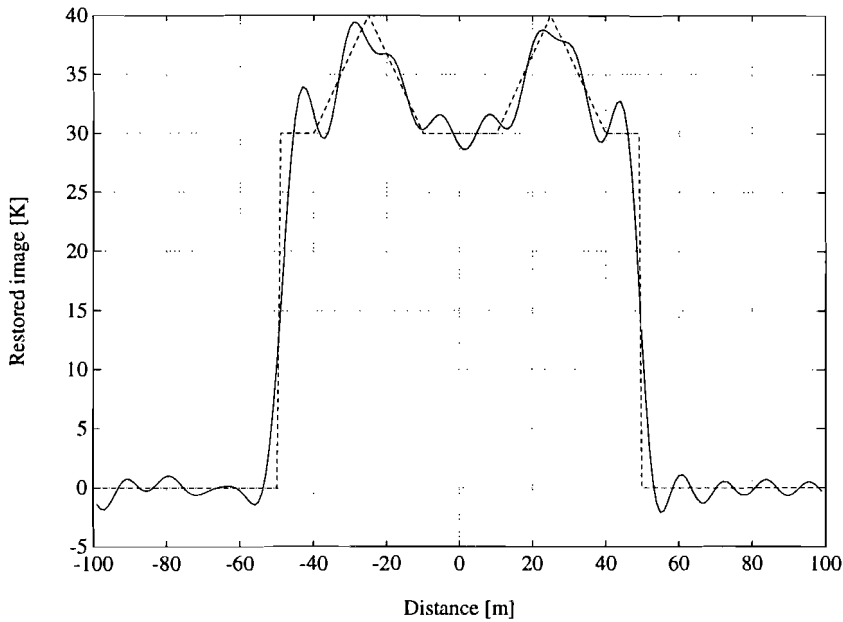


Figure 3.10 : The restored image using inverse filtering with a SNR of 23 dB
(--- object, — restoration).

The conclusion can be drawn that for this average SNR of 23 dB the reconstruction is better so this SNR will be used for coming restoration methods.

3.4 The possibility of bandwidth extrapolation.

The only possibility to increase the maximum resolution gain of 2 is to restore the frequencies beyond the cut-off frequency Ω [9,14,16,18,27,30]. Especially Ref.[18] gives the basis of this extrapolation. This basis is that every entire complex function (in this case the spectrum), can be known in the entire z -plane (i.e. for all frequencies) if its values within a certain region ($|\omega| < \Omega$) are known. The proof lies in the Taylor series of the entire function.

The method used in Ref.[14] will be evaluated though.

The question is, how much extrapolation is needed for a measurable effect?

To approach the problem, it is assumed that the object consists of two equally bright point sources:

$$o(x) = \delta(x - a/2) + \delta(x + a/2) \quad (3.22)$$

Let $\hat{o}_{ext}(x)$ denote the restored output due to perfect spectral restoration (full inverse filtering) within the cut-off bandwidth. The problem is to find the ratio Ω_p/Ω that just resolves the two points in the output. Rayleigh's assumption is that two points are just resolved when the dip in intensity between them is 20%.

The object spectrum is the Fourier transform of (3.22):

$$O(\omega) = 2\cos(a\omega/2) \quad (3.23)$$

After spectral cut-off beyond Ω_p , the restored object will be:

$$\hat{o}_{ex}(x) = \frac{\Omega_p}{\pi} \{ \text{sinc}[\Omega_p(x+a/2)] + \text{sinc}[\Omega_p(x-a/2)] \} \quad (3.24)$$

As mentioned above, the relative dip at $x=0$ has to be at least 20%:

$$\frac{\hat{o}_{ex}(0)}{\hat{o}_{ex}(a/2)} = \frac{2\text{sinc}(a\Omega_p/2)}{1+\text{sinc}(a\Omega_p)} = 0.2 \Rightarrow \Omega_p \approx \frac{3\pi}{2a} \quad (3.25)$$

For example, when the distance between the points is $a=\pi/\Omega$ then it follows that $\Omega_p=3\Omega/2$ to just resolve the two points.

It is assumed that the object is fully reconstructed within $\{-\Omega, \Omega\}$ with inverse filtering.

The question is now whether an extrapolating window $W(\omega)$ exists. This would require the product $W(\omega)O(\omega)$ over the *finite* interval $|\omega| \leq \Omega$ to act like $O(\omega)$ alone over the *infinite* interval, or

$$\int_{-\Omega}^{\Omega} W(\omega)O(\omega)\exp(j\omega x)d\omega \approx A \int_{-\infty}^{\infty} O(\omega)\exp(j\omega x)d\omega = Ao(x) \quad (3.26)$$

The object $o(x)$ is considered of limited spatial extent, so Eq.(3.26) would have to be satisfied only at values $|x| \leq X$.

Then, the solution is

$$W_N(\omega) = \sum_{n(\text{even})=0}^N (-1)^{n/2} \lambda_n(c)^{-3/2} \psi_n(c,0) \psi_n(c,2\omega X/\Omega) \quad (3.27)$$

The constant c is defined as $2X\Omega$.

The larger N is made, the better requirement Eq.(3.26) is satisfied, but the smaller multiplier A becomes.

In Eq.(3.27), the functions ψ_n and the numbers λ_n are the *prolate spheroidal wave functions* and their eigenvalues, developed by Slepian and others [30], and they have the following properties:

$$1. \int_{-\infty}^{\infty} \psi_i(t) \psi_j(t) dt = \begin{cases} 0, & i \neq j \\ 1, & i = j \end{cases} \quad i, j = 0, 1, 2, \dots \quad (3.28)$$

$$2. \int_{-T/2}^{T/2} \psi_i(t) \psi_j(t) dt = \begin{cases} 0, & i \neq j \\ \lambda_i, & i = j \end{cases} \quad i, j = 0, 1, 2, \dots \quad (3.29)$$

$$3. \lambda_i \psi_i(t) = \int_{-T/2}^{T/2} \frac{\sin \Omega(t-\tau)}{\pi(t-\tau)} \psi_i(\tau) d\tau, \quad i = 0, 1, 2, \dots \quad (3.30)$$

Equation (3.30) indicates that the functions ψ_i are eigenfunctions of the operation that limits in time (or space) to the interval $\{-1/2T, 1/2T\}$ (in this case $\{-X, X\}$) and in frequency (or radial frequency) to the interval $\{-\Omega, \Omega\}$. Obviously, both the ψ 's and the λ 's are functions of the product ΩT , in this case of ΩX , which explains the used definition of c .

The special case of $O(\omega) = 1$ for all frequencies ($o(x) = \delta(x)$) leads to the requirement that the finite F.T. of $W(\omega)$, the overall point spread function $s_{net}(x)$, has to be a delta function, when Eq.(3.26) is used. In fact, function $W_N(\omega)$ has been found to obey

$$s_{net}(x) = \frac{1}{2\pi} \int_{-\Omega}^{\Omega} W_N(\omega) \exp(j\omega x) d\omega = A \delta_N(x), \quad |x| \leq 2X \quad (3.31)$$

where $\delta_N(x)$ is an N -th-order approximation to the Dirac delta function,

$$\delta_N(x) = \sum_{n(even)=0}^N \lambda_n(c)^{-1} \psi_n(c, 0) \psi_n(c, x), \quad |x| \leq 2X \quad (3.32)$$

Plots of $W_{40}(\omega)$ and $\delta_{40}(x)$ for the case $N=40$ and $c=6.25$ are shown in figures 3.10 and 3.11 on the next page.

This window is symmetric about the origin. Over a wide region around the origin it is well approximated by a cosine curve. Both the frequency and amplitude of $W_{40}(\omega)$ increase rapidly as the cutoff frequency Ω is approached.

For comparison, the dashed curve is the net spread function for inverse filtering over the same frequency range as for $W_{40}(\omega)$. The dotted curve is the net spread function for inverse filtering over a frequency range of 6 times that of $W_{40}(\omega)$. Hence this window function acts to extrapolate the object spectrum by a factor of 6, for this c -value.

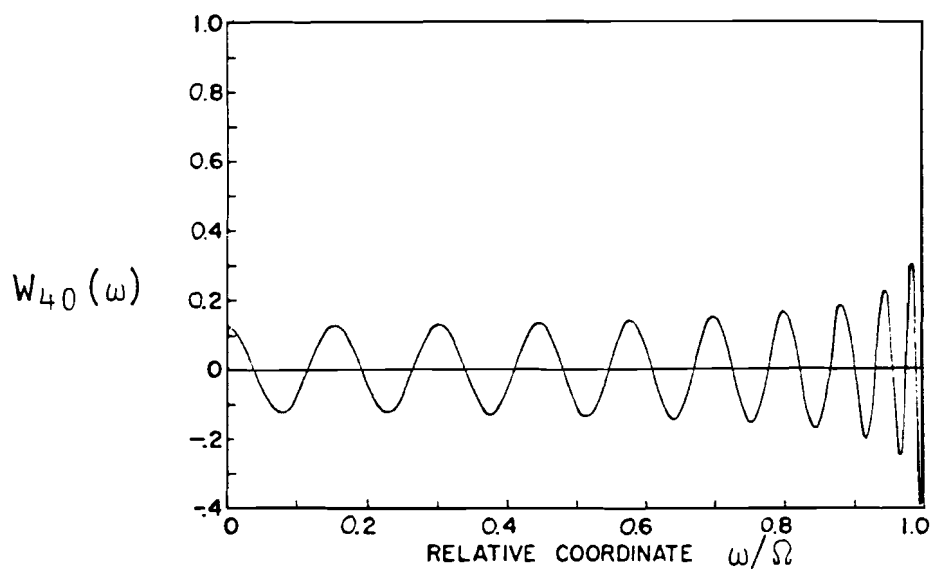


Figure 3.11 : Extrapolating window $W_{40}(\omega)$ for the case $c=6.25$.

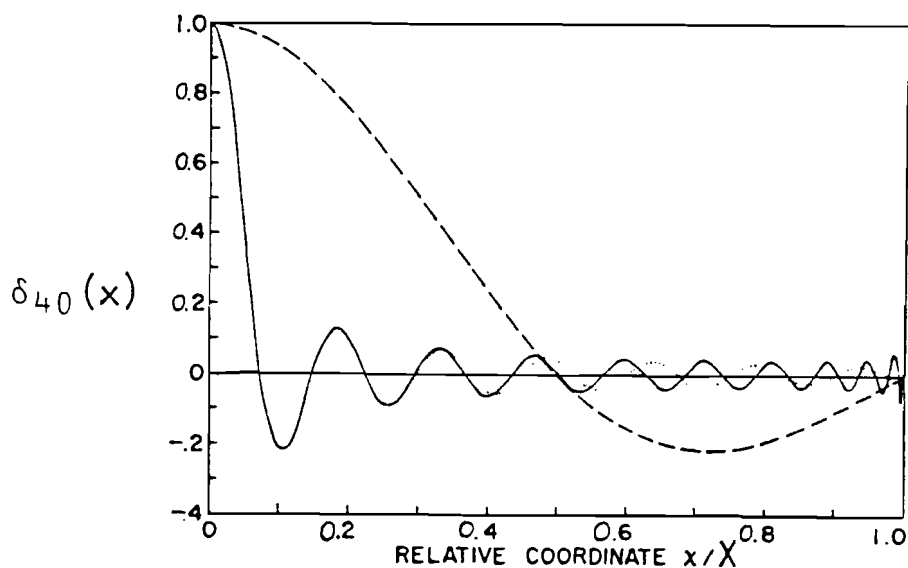


Figure 3.12 : The Fourier transform $\delta_{40}(x)$ (solid curve) of the window function.

The problem with actual use of this window function is that it extrapolates both the signal and the noise part of the input image; it amplifies the noise even more than is the case of normal inverse-filtering, because it allows the whole noise band in its output.

Another problem is that this approach can never be performed on-line because the whole signal has to be disposed of.

The application of this extrapolation technique to the situation discussed before led to too many computational problems so the given examples are the only illustrations that can be given.

It can be concluded that the prognostications of the practical use of this method are not very good so this discussion can be considered purely as an interesting illustration how the problem of bandwidth limitation can be handled, theoretically.

Chapter 4

Statistical Filtering Approach

In the previous section the approach to deconvolution of the data was rather intuitive. This section will deal with an optimization based on a more mathematical method. Firstly, the basic, unconstrained method is treated and successively some alterations or additions will be made. At the end, a relation between the derived optimum deconvolution filter and the Shannon information content of the image data will be analyzed.

4.1 Wiener filter.

The goal of the restoring filter is to reconstruct the object as accurately as possible in the presence of noise, i.e. to minimize the error between object and estimate. When looking for a method to minimize an error between to signals, one will automatically encounter the method of *Wiener filtering* [5,12,14,20,21,23,27,32,33].

Just like in the previous section, it is assumed that all signals used are random, stationary, ergodic and that they represent an infinite time series to justify continuous Fourier analysis.

The object of the Wiener filter is to minimize the mean square error between the true and the reconstructed object:

$$\epsilon^2 = \left\langle \frac{1}{2\pi} \int_{-\infty}^{\infty} |O(\omega) - \hat{O}(\omega)|^2 d\omega \right\rangle = \text{minimum} \quad (4.1)$$

The criterion becomes:

$$\frac{1}{2\pi} \int_{-\infty}^{\infty} \langle |O(\omega) - Y(\omega)I(\omega)|^2 \rangle d\omega = \text{minimum} \quad (4.2)$$

After elaborating this expression, making use of Eq.(2.9) and (2.3), and the fact that object and noise are uncorrelated, it follows that:

$$\begin{aligned} \epsilon^2 &= \frac{1}{2\pi} \int_{-\infty}^{\infty} \left\{ \Phi_o(\omega) - [Y^*(\omega)S^*(\omega) + Y(\omega)S(\omega)]\Phi_o(\omega) + |Y(\omega)|^2 [S(\omega)^2\Phi_o(\omega) + \Phi_n(\omega)] \right\} d\omega \\ &= \frac{1}{2\pi} \int_{-\infty}^{\infty} \left\{ |1 - Y(\omega)S(\omega)|^2 \Phi_o(\omega) + |Y(\omega)|^2 \Phi_n(\omega) \right\} d\omega = \frac{1}{2\pi} \int_{-\infty}^{\infty} \left\{ |1 - S_{net}(\omega)|^2 \Phi_o(\omega) + |Y(\omega)|^2 \Phi_n(\omega) \right\} d\omega \end{aligned} \quad (4.3)$$

This expression is comparable to expression for the error (Eq.(3.20) using inverse filtering.

The function $|1 - S_{net}(\omega)|^2$ is for inverse filtering unity except in the interval from $-\Omega_p$ to Ω_p , where it is zero and $|Y(\omega)|^2$ is in the case of inverse filtering nothing more than $1/|S(\omega)|^2$.

This error can be written, as in the usual treatment of Wiener filtering [20,33]:

$$\epsilon^2 = \int_{-\infty}^{\infty} \left\{ \left| Y(\omega) - \frac{S^*(\omega)\Phi_o(\omega)}{\gamma(\omega)} \right|^2 \gamma(\omega) + \frac{\Phi_o(\omega)\Phi_n(\omega)}{\gamma(\omega)} \right\} d\omega \quad (4.4)$$

with

$$\gamma(\omega) = |S(\omega)|^2 \Phi_o(\omega) + \Phi_n(\omega) \quad (4.5)$$

From this expression it is obvious that the filter $Y(\omega)$ that minimizes the mean-squared error is given by:

$$Y(\omega) = \frac{S^*(\omega)\Phi_o(\omega)}{|S(\omega)|^2 \Phi_o(\omega) + \Phi_n(\omega)} = \frac{S^*(\omega)}{|S(\omega)|^2 + \Phi_n(\omega)/\Phi_o(\omega)} \quad (4.6)$$

This is a common form for a filter that minimizes a mean-squared error, and it is called the *Wiener filter*. For a high signal-to-noise ratio, the Wiener filter approaches inverse filtering, which is no surprise.

The drawbacks of this method are that the power spectra are rarely known, and that the filter minimizes the error on the ensemble average, while the user may be interested in only a few restorations when the assumption of ergodicity is not valid.

The approximation made in the previous chapter, which was using the overall signal-to-noise ratio instead of the spectral signal-to-noise ratio, will therefore also be used here.

Figure 4.1 depicts the Wiener filter for the imaging antenna filter used and the average energy signal-to-noise ratio of 23 dB discussed in chapter 3, because the the real SNR based on the 100 m interval leads to serious blurring, which will be shown afterwards.

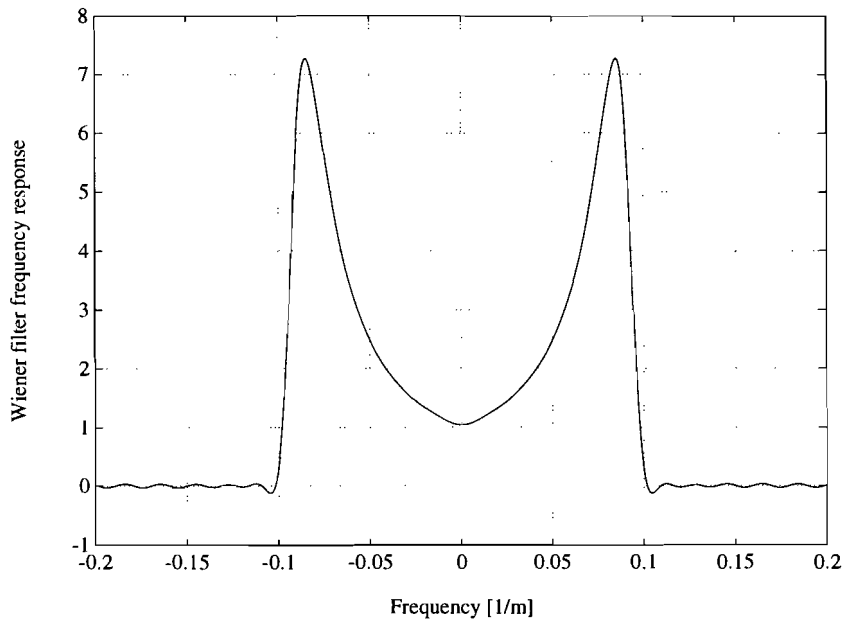


Figure 4.1 : The Wiener filter for a signal-to-noise ratio of 23 dB.

Apparently, the Wiener filter restores high-frequency components, attenuated by the imaging antenna. The peaks in this filter will increase and move closer to the cut-off frequency as the signal-to-noise ratio increases. The main difference compared to the inverse filter is that the Wiener filter does not exhibit an abrupt transition to zero at cut-off, but falls off in a continuous way.

It could be interesting to regard the correspondence between the peaks in the optimum inverse filter and the peaks in the Wiener filter,

The position of the peaks can be found by differentiating the Wiener filter and setting the result to zero, making use of the fact that $s(x)$ is even so $S(\omega)$ is real and of the above-mentioned approximation:

$$\frac{d}{d\omega} \left\{ \frac{S(\omega)}{S^2(\omega) + 1/snr} \right\} = \frac{dS(\omega)}{d\omega} \frac{1/snr - S^2(\omega)}{[S^2(\omega) + 1/snr]^2} = 0 \Rightarrow S(\omega) = \frac{1}{\sqrt{snr}} \vee \frac{dS(\omega)}{d\omega} = 0 \quad (4.7)$$

The second solution is $\omega=0$ because of the evenness of $S(\omega)$.

The first solution is exactly the same as Eq.(3.21) which means that the peaks in the optimum inverse filter and the peaks in the Wiener filter occur at the same frequencies.

The height of the peaks in the inverse filter case are found by substituting Eq.(3.21) in Eq.(3.17) which leads to a peak height of \sqrt{snr} , while substituting Eq.(4.7) in the Wiener filter described by Eq.(4.6), with the above-mentioned assumptions, yields a peak height of $1/2\sqrt{snr}$.

The Wiener filter can therefore be regarded as a "smoothed optimum inverse filter".

Figure 4.2 shows the overall imaging system filter $S_{net}(\omega)$, the antenna followed by the restoring filter, for a signal-to-noise ratio of 23 dB.

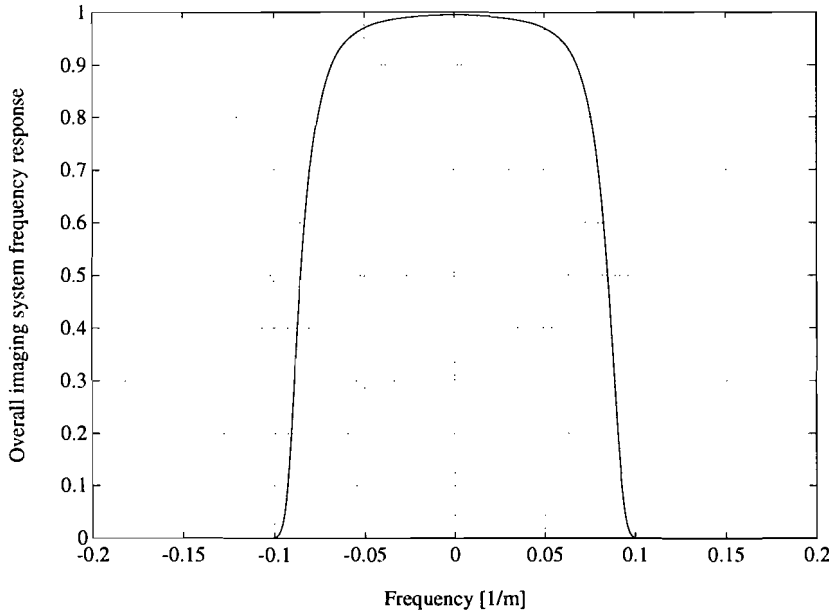


Figure 4.2 : The overall imaging system.

The higher the signal-to-noise ratio, the more rectangular the overall filter will be.

The overall point spread function, which is the impulse response, is the inverse Fourier transform of this overall transfer function.

Figure 4.3 depicts this impulse response together with the impulse response for a rectangular overall filter i.e. for an infinite signal-to-noise ratio.

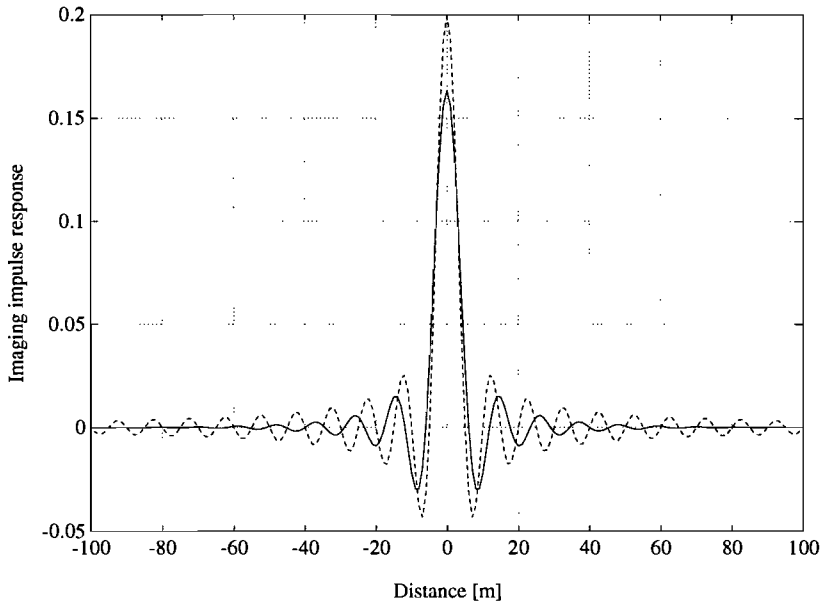


Figure 4.3 : The point spread function of the Wiener filtered system (---- rectangular, ——— Wiener).

It can be concluded that the ringing effect of the sinc function has been attenuated, while resolution loss can be kept to a minimum.

Unfortunately, the information beyond the cut-off frequency is still lost and can only be retrieved if extrapolation methods will be used.

The reconstructed image is shown in figure 4.4.

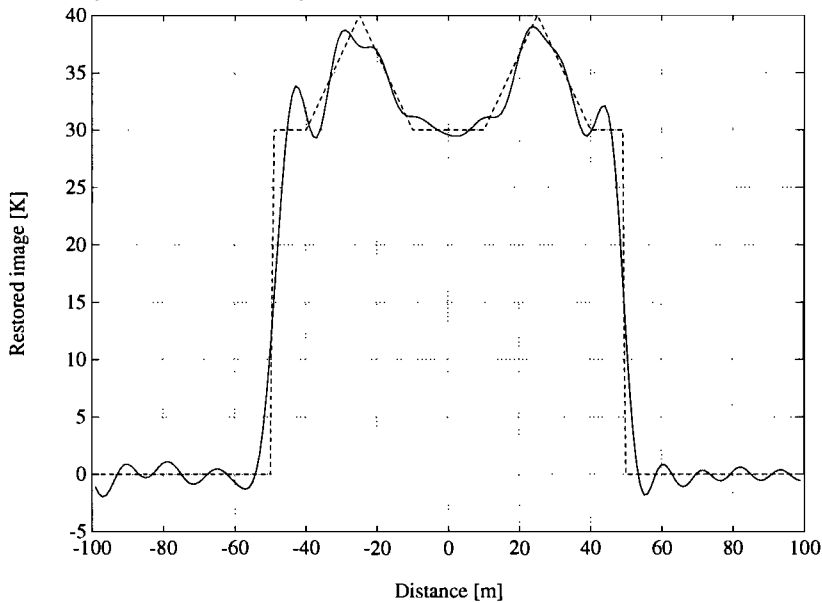


Figure 4.4 : The reconstructed image using Wiener filtering (---- object, ——— reconstruction).

Apparently, the oscillatory blurring in the reconstruction is still present, but less than in the case of inverse filtering. In the previous chapter the question arose whether this blurring was caused by the discontinuities in the object (high spectral components) or the abrupt transition in the overall filter, leading to a sinc overall point spread function. This last effect has clearly lost much of its influence, according to Figures 4.2 and 4.3 so the blurring is undoubtedly caused by the cutoff of the higher frequency components that make a sharp transition without ringing possible. The blurring outside the object is due to the noise that is amplified by the Wiener filter peaks.

The Wiener filtering technique for the real SNR of 36 dB based on the 100 m interval is also performed for illustration of the blurring.

The Wiener filter will look like shown in figure 4.5.

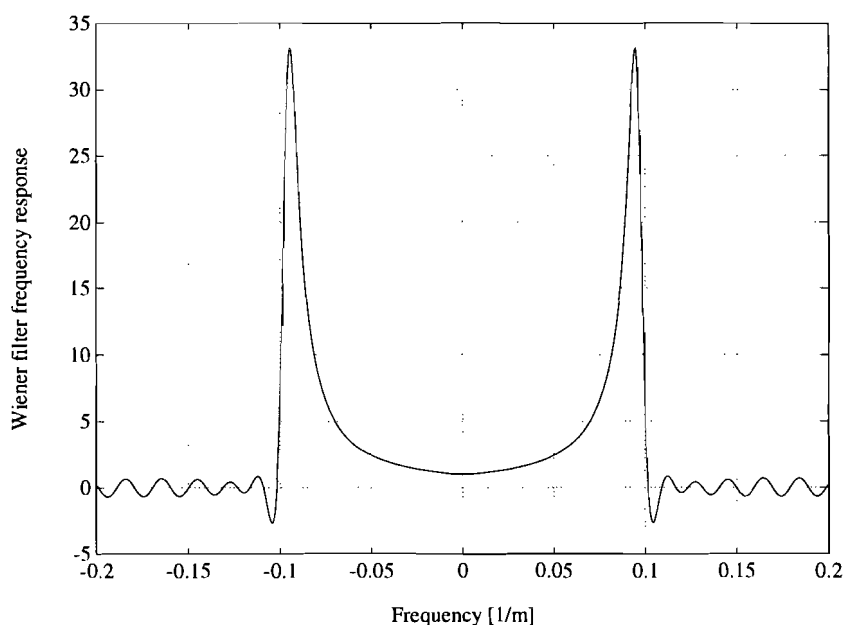


Figure 4.5 : The Wiener filter for a signal-to-noise ratio of 36 dB.

As expected, the peaks shift towards Ω and become higher with increasing SNR.

The resulting overall filter is illustrated in figure 4.6 on the next page.

It can be expected that the blurring present in the reconstruction shown in figure 4.4 will be strongly amplified, because of the increase and shift of the peaks, just like in the previously discussed case of inverse filtering.

The reconstruction for this SNR is shown in figure 4.7.

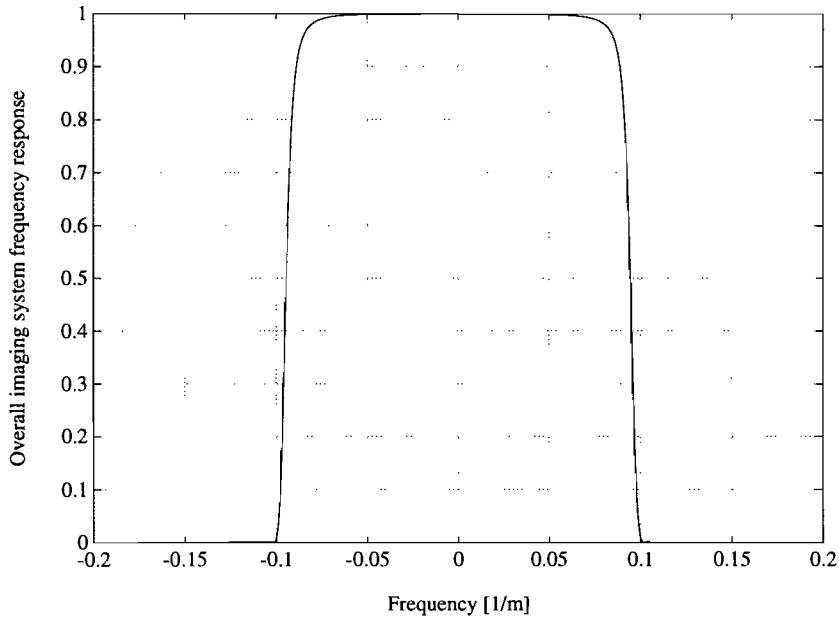


Figure 4.6 : The overall imaging filter for a SNR of 36 dB.

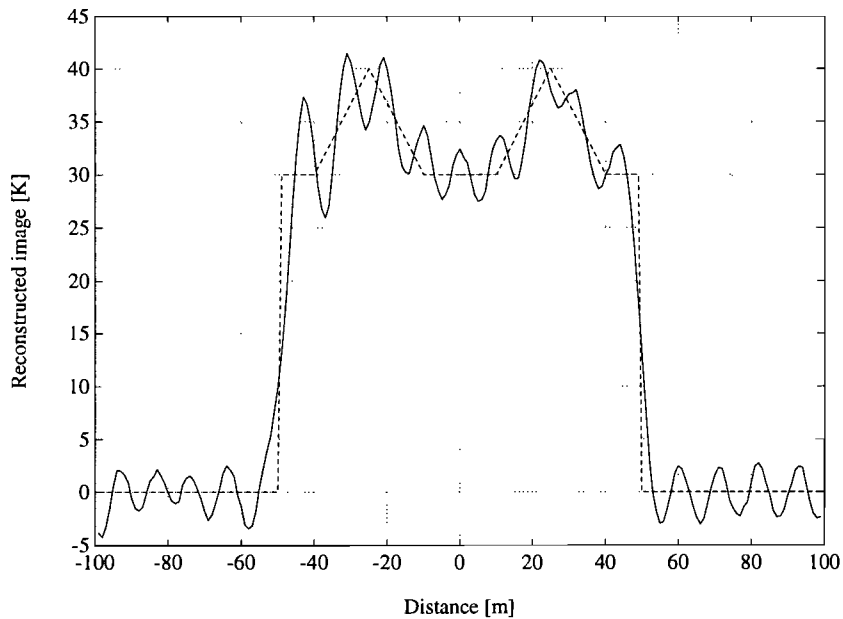


Figure 4.7 : The reconstruction for a signal-to-noise ratio of 36 dB (---- object, — reconstruction).

This reconstruction is very poor, even poorer than inverse filtering for the same case. This is probably caused by the fact that in the Wiener method noise frequencies between Ω_p and Ω are included.

It will also be interesting to see how the reconstruction improves when the signal-to-noise ratio truly increases by reducing the noise variance. To increase the (average) SNR used of 23 dB to 33 dB the noise variance has been decreased with 10 dB to 0.025 K^2 .

The resulting image is depicted in figure 4.8.

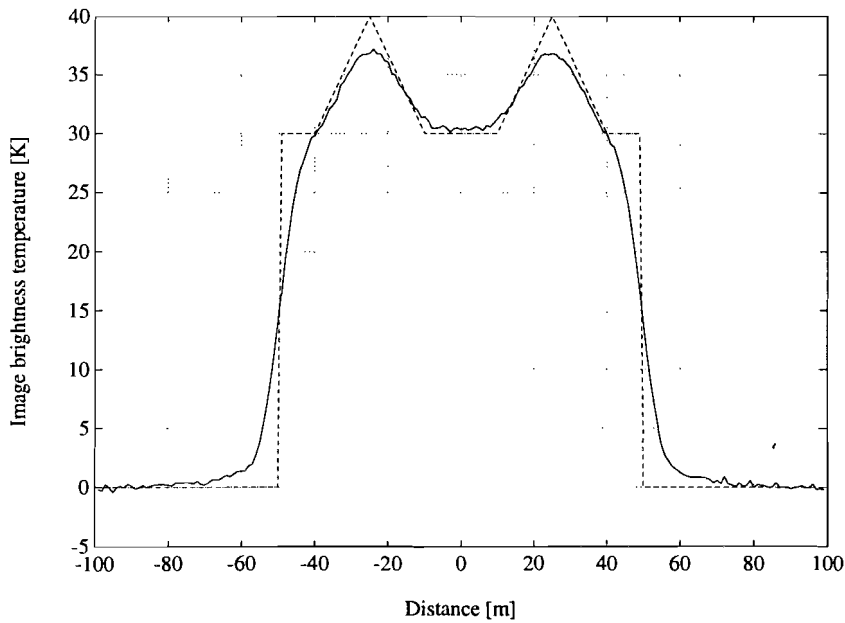


Figure 4.8 : The image for a increased SNR to 33 dB.

The reconstruction for this case is shown in figure 4.9.

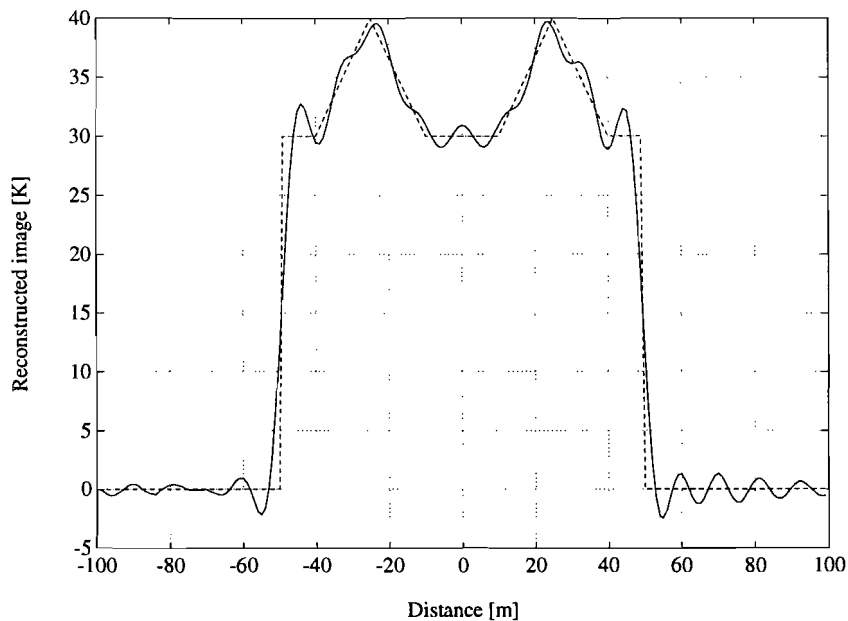


Figure 4.9 : The Wiener reconstruction for an increased SNR of 33 dB (---- object, ——— reconstruction).

It is clear to see that this reconstruction is better, but the ringing remains unavoidable.

Let's have a glance at the reconstruction error. The error between object and reconstructed object cannot be measured so the error between image $i(x)$ and estimated image $\hat{i}(x)$ will be regarded.

These quantities are described by the following expressions, in which the sign $*$ stands for the convolution process.

$$\begin{cases} i(x) = o(x) * s(x) + n(x) \\ \hat{i}(x) = \hat{o}(x) * s(x) \end{cases} \quad (4.8)$$

In the frequency domain this error is described as

$$I(\omega) - \hat{I}(\omega) = [1 - Y(\omega)S(\omega)]I(\omega) = \frac{1}{\zeta |S(\omega)|^2 + 1} I(\omega) \quad (4.9)$$

in which ζ is the signal-to-noise ratio.

The error transfer function $1 - Y(\omega)S(\omega)$ is illustrated in figure 4.10 for a SNR of 23 dB.

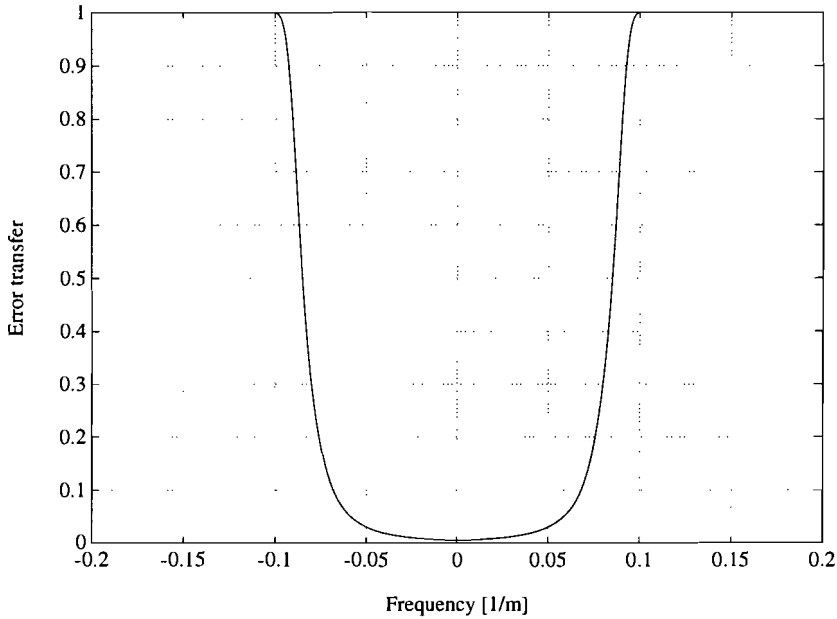


Figure 4.10 : The error transfer function.

This figure illustrates the fact that when the SNR is chosen right, the error is uncorrelated with the image, because the error transfer function eliminates the frequencies within the image band, so the error will consist mainly of noise. This error is illustrated in figure 4.11 on the next page.

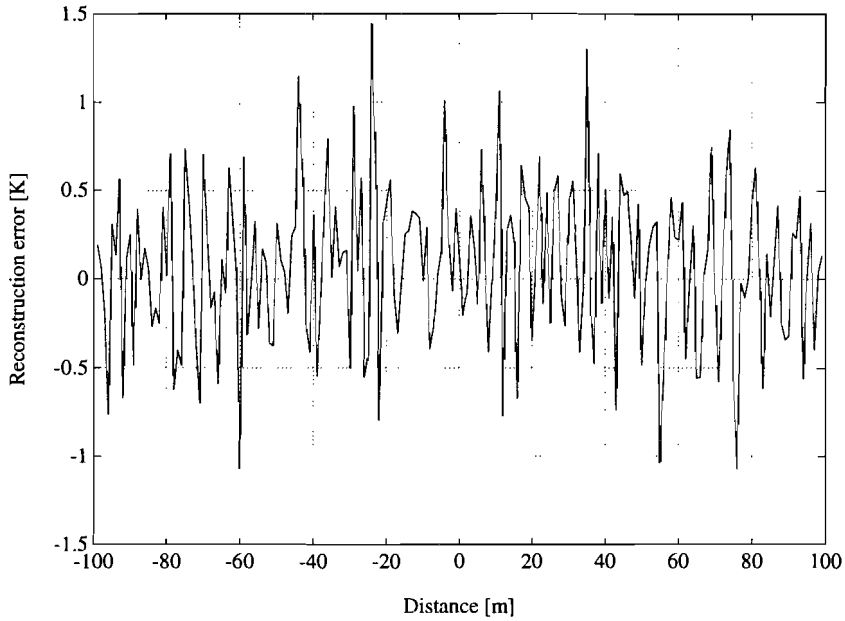


Figure 4.11 : *The reconstruction error with the right SNR.*

The correlation with the image is hardly to be seen, but it is still a little bit present because the error filter smoothly cancels out the image frequencies.

The error filter for a low estimate of the SNR is shown in figure 4.12.

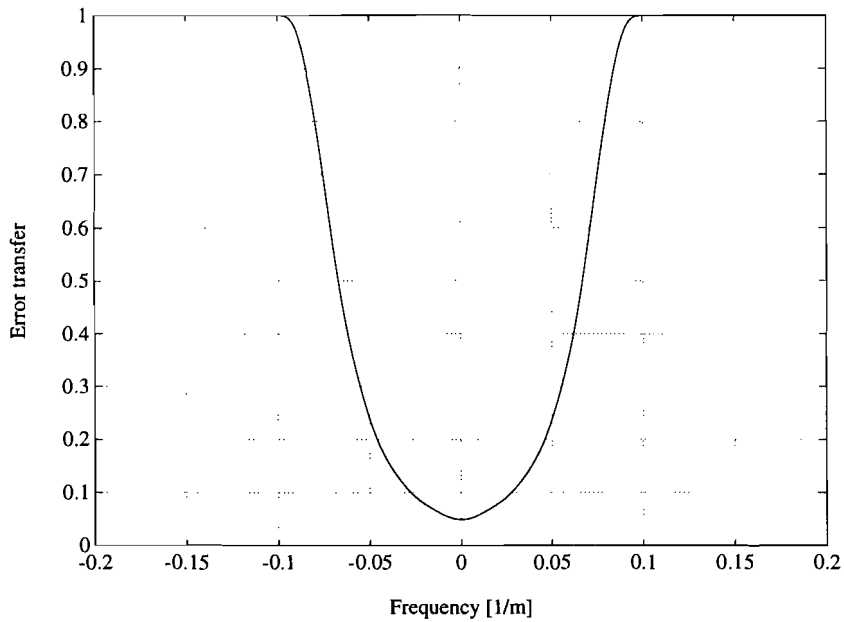


Figure 4.12 : *The error filter for a too low estimated SNR.*

It is obvious that the image frequencies will influence the error considerably, which results in an error depicted in figure 4.13 on the next page.

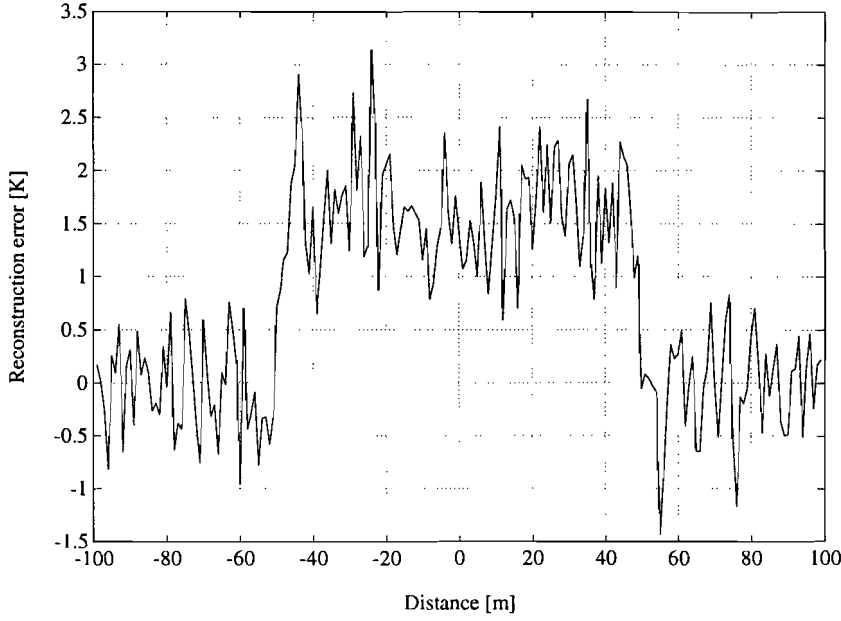


Figure 4.13 : *The error for a too low estimated SNR.*

The image is indeed clearly present in the error.

When the estimate of the SNR is too high, the error transfer function will be more square which means that the error will still be uncorrelated with the image and only the noise outside the image band will be present and the inband noise has propagated into the estimated object.

Appendix A illustrates the correspondence with matrix techniques.

4.2 Sharpness-constrained Wiener filter.

The oscillatory blurring of the reconstruction can be reduced by adding a constraint to the error criterion. This constraint will have to result in a smoothing of the image.

This can be achieved by minimizing the total edge-gradient "content", given by the *sharpness* S [14]:

$$S \triangleq \left\langle \int_{-\infty}^{\infty} \left| \frac{d\hat{o}(x)}{dx} \right|^2 dx \right\rangle = \left\langle \int_{-\Omega}^{\Omega} \omega^2 |\hat{O}(\omega)|^2 d\omega \right\rangle \quad (4.10)$$

The new, net criterion now becomes, with $\hat{O}(\omega)=Y(\omega)I(\omega)$:

$$\int_{-\Omega}^{\Omega} \langle |O(\omega) - Y(\omega)I(\omega)|^2 \rangle d\omega + \lambda \int_{-\Omega}^{\Omega} \omega^2 \langle |Y(\omega)I(\omega)|^2 \rangle d\omega = \text{minimum} \quad (4.11)$$

From this relation it is clear that more or less emphasis on sharpness control is exercised by choice of the Lagrange multiplier λ .

After elaborating this expression in the same way as in the previous paragraph, it follows that:

$$Y(\omega) = \frac{S^*(\omega)\Phi_o(\omega)}{|S(\omega)|^2\Phi_o(\omega) + \Phi_n(\omega)} \cdot \frac{1}{1 + \lambda\omega^2} \quad (4.12)$$

Obviously, the derived filter consists of two parts. The first part is the Wiener filter, minimizing the mean squared error, and the second part is sharpness-control filter; for a choice $\lambda > 0$ it attenuates high frequencies, smoothing the estimate, and for a choice $\lambda < 0$ it boosts the high frequencies.

The smoothing filter with a λ of 4 is shown in figure 4.14.

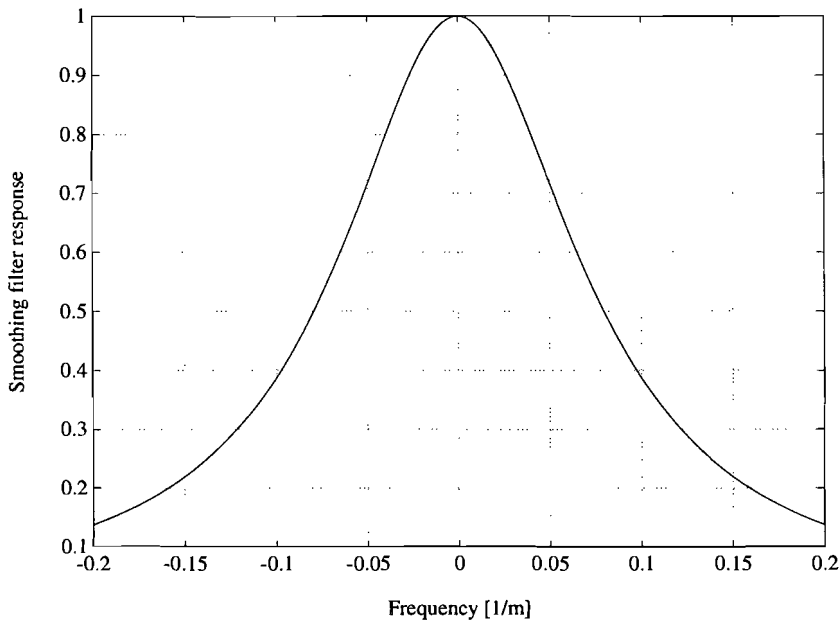


Figure 4.14 : The smoothing filter.

The overall point spread function (returning to a SNR of 23 dB) achieved by this smoothing is shown in figure 4.15.

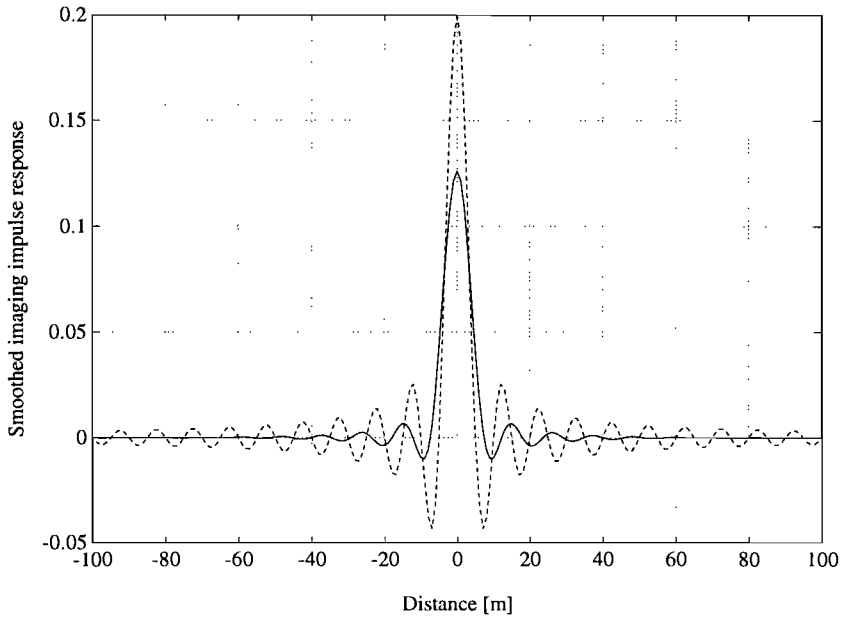


Figure 4.15 : *The smoothed impulse response (---- rectangular, ——— smoothed).*

Apparently, the ringing effect has practically disappeared but the price that had to be paid is a significant loss of resolution (width of the main lobe).

When the value of λ will be increased, too much high-frequency information would be lost, resulting in poor resolution. Decreasing of λ would lead to a more abrupt transition at the edges resulting in blurring of the image.

The effect on the reconstruction is illustrated in figure 4.16 on the next page.

This constrained method appears to yield very good results: the reconstruction is considerably smoothed while the loss in resolution is hardly noticed in practice.

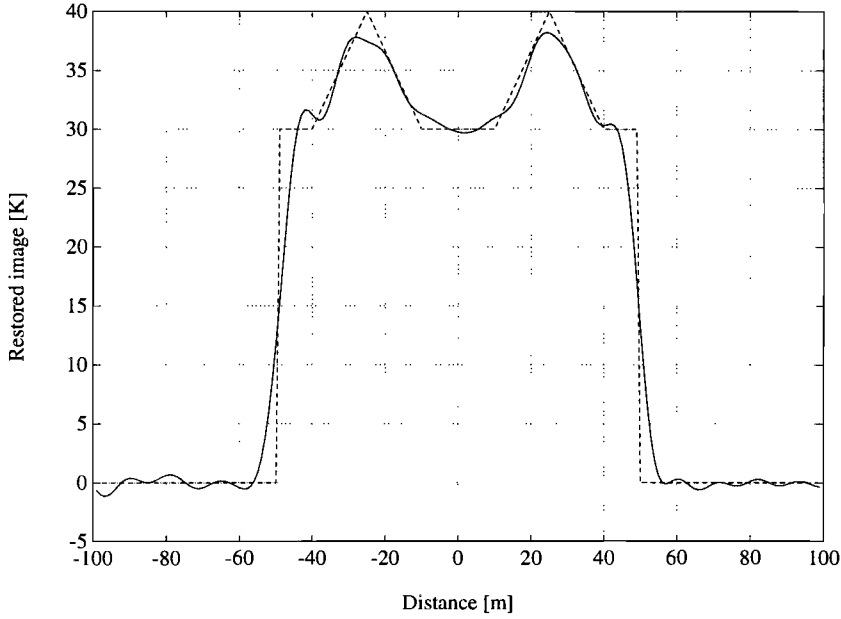


Figure 4.16 : The effect of the "sharpness" filter on the reconstruction for $\lambda=4$ (---- object, — reconstruction).

4.3 Backus-Gilbert optimization approach.

Another suggestion is to *separately* minimize, in some convenient sense, the output noise and the output departure of signal restoration from true object [14].

The total mean square output noise is

$$\eta^2 \triangleq \left\langle \int_{-\infty}^{\infty} |Y(\omega)N(\omega)|^2 d\omega \right\rangle = \int_{-\infty}^{\infty} |Y(\omega)|^2 \Phi_n(\omega) d\omega \quad (4.13)$$

A convenient measure of the second feature is the mean square output departure of the filter output $Y(\omega)S(\omega)O(\omega)$ from a required, windowed estimate $W(\omega)O(\omega)$:

$$\mu^2 \triangleq \left\langle \int_{-\infty}^{\infty} |W(\omega)O(\omega) - Y(\omega)S(\omega)O(\omega)|^2 d\omega \right\rangle \quad (4.14)$$

The window $W(\omega)$ is therefore the *desired* overall imaging filter $Y(\omega)S(\omega)$ (antenna plus reconstruction filter); it can be a rectangular window when the object under study is a smooth signal, which means that it has no excessive high-frequency components that cannot be restored.

The restoring filter $Y(\omega)$ on one hand takes care of noise suppression in η^2 while on the other hand it attempts to approximate the desired overall imaging filter as close as possible in μ^2 .

The Backus-Gilbert criterion becomes

$$\lambda_1 \eta^2 + \lambda_2 \mu^2 = \text{minimum} \quad (4.15)$$

Parameters λ_1 and λ_2 are chosen by the user so as to provide emphasis on either noise suppression (λ_1/λ_2 large) or resolution enhancement (λ_2/λ_1 large).

Using the same method as for the Wiener filter, the obtained filter is:

$$Y_{BG}(\omega) = \frac{S^*(\omega)\Phi_o(\omega)W(\omega)}{|S(\omega)|^2\Phi_o(\omega) + (\lambda_1/\lambda_2)\Phi_n(\omega)} = \frac{S^*(\omega)W(\omega)}{|S(\omega)|^2 + (\lambda_1/\lambda_2)\Phi_n(\omega)/\Phi_o(\omega)} \quad (4.16)$$

The resemblance to the unconstrained Wiener filter is remarkable: when the desired window $W(\omega)$ is rectangular and no discrimination is made between noise suppression and resolution enhancement, it is even the same. Apparently, when resolution is strongly emphasized, the filter approximates a windowed inverse-filter.

In the following illustration a λ_2/λ_1 is chosen to be 10 (resolution enhancement). The Backus-Gilbert filter (without the window) will then look like as shown in figure 4.17 on the next page.

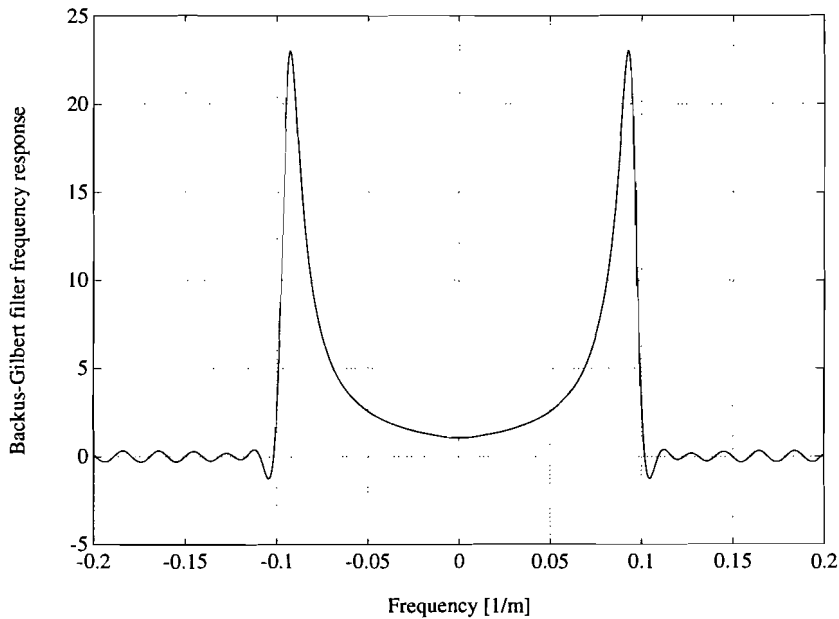


Figure 4.17 : The Backus-Gilbert filter for a resolution emphasis of 10 dB.

This is exactly the same filter as if the signal-to-noise ratio were 10 dB higher so it nothing more than the Wiener filter for a SNR of 33 dB.

The overall imaging filter without the window would look like as depicted in figure 4.18.

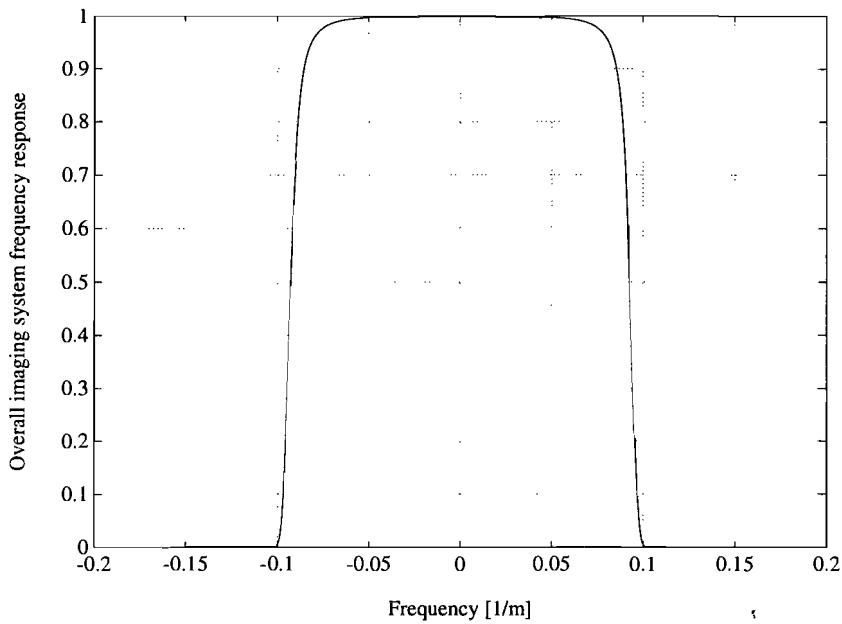


Figure 4.18 : *The overall imaging filter.*

In reality, the signal-to-noise ratio is not 10 dB higher, though, so this would lead to enormous noise amplification.

A possible realization of the desired overall filter is a raised-cosine window [28] as depicted in figure 4.19.

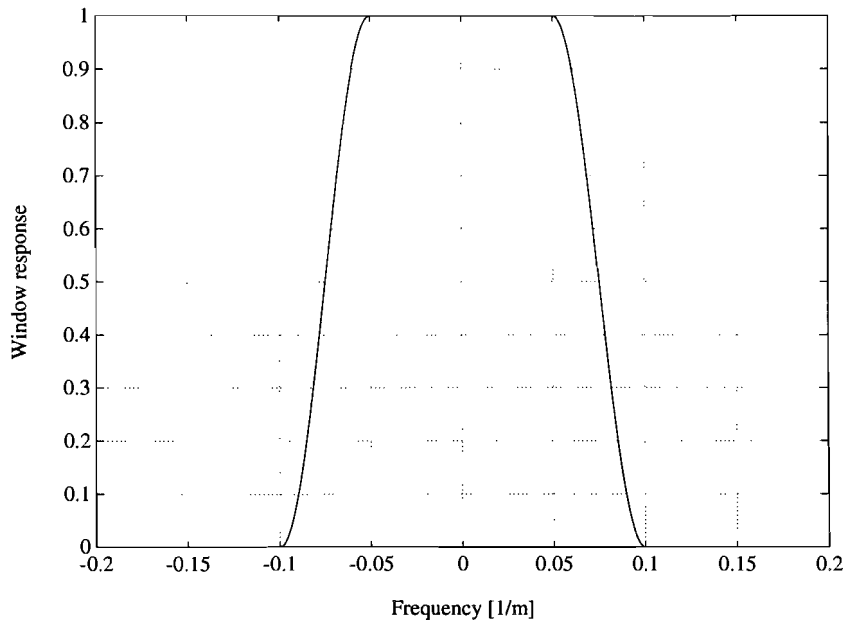


Figure 4.19 : *The raised-cosine window.*

This window has been used because its sidelobe level is very low.
The result of this restoration technique is illustrated in figure 4.20.

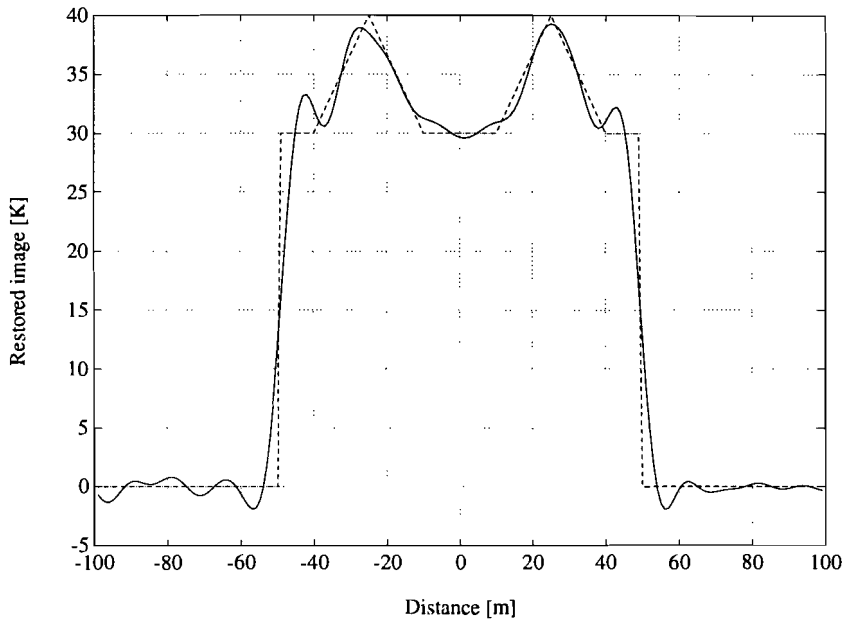


Figure 4.20 : *The Backus-Gilbert reconstruction with resolution emphasis.*

The result is not very much different from the sharpness-constrained Wiener filtering approach, since the only thing that is done is firstly boosting the high frequencies, and then attenuating them again with the window. In fact, a sharpness filter can be used as the desired transfer, and the Backus-Gilbert approach can be applied.

In the previous example resolution enhancement was emphasized by a λ_2/λ_1 of 10. In figure 4.21 noise suppression is emphasized by using a λ_2/λ_1 of 0.1.

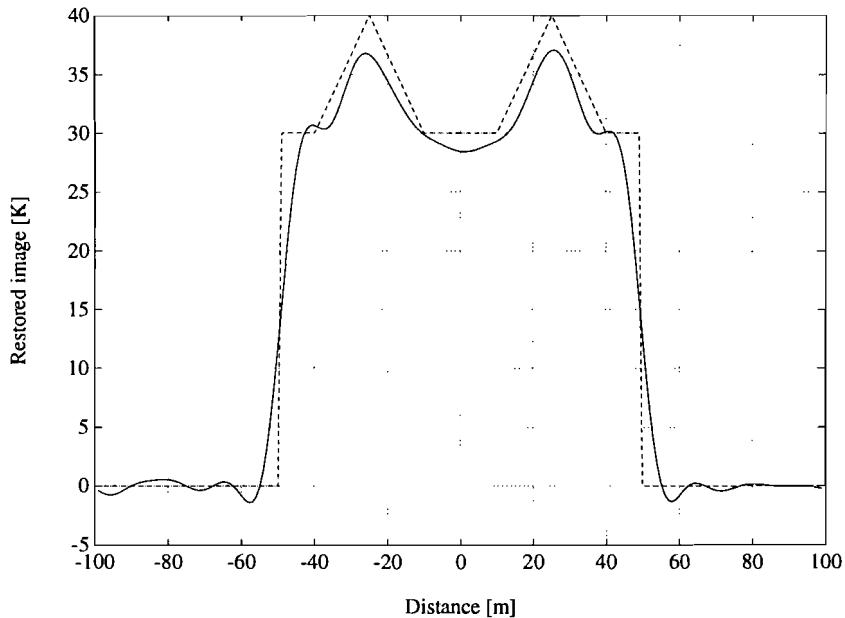


Figure 4.21 : *The Backus-Gilbert reconstruction with noise suppression.*

As expected, the reconstruction is smoother, but the price of resolution loss had to be paid.

4.4 Information aspect of optimum filtering.

A related parameter to the signal-to-noise ratio, and one that directly varies with it in the specific case of Gaussian statistics, is the Shannon information content. This quantity enjoys a rich background of development, analysis and interpretation and is widely regarded as the proper measure of what we intuitively call *information* [14,15].

When unconstrained Wiener filtering is regarded, the filter $Y(\omega)$ is directly related to the Shannon information content in spectral image data $I(\omega)$.

The Shannon information density $SI(\omega)$ in the frequency domain in bits per m^{-1} is:

$$SI(\omega) = {}^2\log \left[1 + \frac{|S(\omega)|^2 \Phi_o(\omega)}{\Phi_n(\omega)} \right] \quad (4.17)$$

In this equation, the term added to unity, is simply the image signal spectrum over the noise spectrum. This information density is also called the channel capacity for image formation. The information content for the used system is depicted in figure 4.22, where the spectral signal-to-noise ratio $\Phi_o(\omega)/\Phi_n(\omega)$ is replaced by the overall energy signal-to-noise ratio of 23 dB.

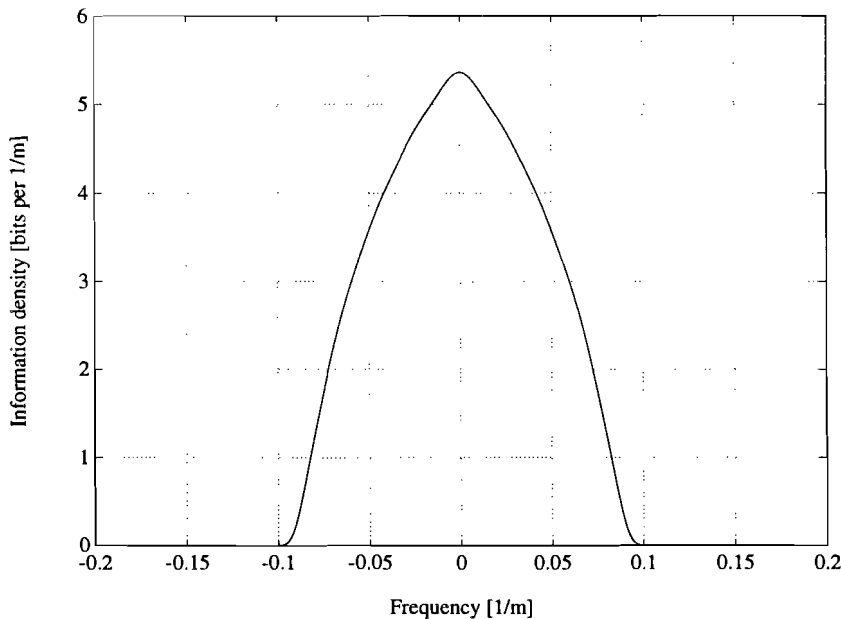


Figure 4.22 : The Shannon information density of the imaging system for a SNR of 23 dB.

And again can be concluded that all information beyond cut-off is lost.

After combining (3.6) and (3.10), the following result is obtained:

$$Y(\omega) = \frac{1}{S(\omega)} (1 - 2^{-SI(\omega)}) \quad (4.18)$$

Thus, the full compensation factor $1/S(\omega)$ is modulated by a function of the information SI . Full compensation (maximum resolution) is only allowed when the signal to noise ratio is infinite. When it approaches zero, no restoration is permitted.

The use of the optimum filter $Y(\omega)$ produces a minimized mean square error, according to Eq.(4.4), of

$$\epsilon^2 = \frac{1}{2\pi} \int_{-\infty}^{\infty} \frac{\Phi_n(\omega) \Phi_o(\omega)}{|S(\omega)|^2 \Phi_o(\omega) + \Phi_n(\omega)} d\omega = \frac{1}{2\pi} \int_{-\infty}^{\infty} \frac{\Phi_n(\omega)}{|S(\omega)|^2 + \Phi_n(\omega)/\Phi_o(\omega)} d\omega \quad (4.19)$$

Using relation (4.17), it is found that

$$\epsilon^2 = \frac{1}{2\pi} \int_{-\infty}^{\infty} \Phi_o(\omega) 2^{-SI(\omega)} d\omega \quad (4.20)$$

This shows that the *mmse* attenuates exponentially with information content.

Chapter 5

Real Time Digital Filter Implementation

In the previous chapter the frequency-domain Wiener filtering and discrete matrix techniques were treated. The problem of both methods however is that the reconstruction algorithm needs to have the entire measurement series at its disposal while it is favourable to perform *real time processing*, i.e. process a sample as soon as it is taken.

Since this chapter deals with real time, reality will be met firstly in the treatment of the object.

5.1 Atmospheric brightness temperature simulation.

In Ref.[6], P. Basili et al. investigated selected strong scintillation events which occurred on the *Orbital Test Satellite* experimental space-earth downlink. Statistical properties of the fluctuations of the sky temperature were measured with a radiometer operating at a frequency of 11.4 GHz with a 2-m antenna.

The result of the measurement is the atmospheric brightness temperature spectrum shown in figure 5.1.

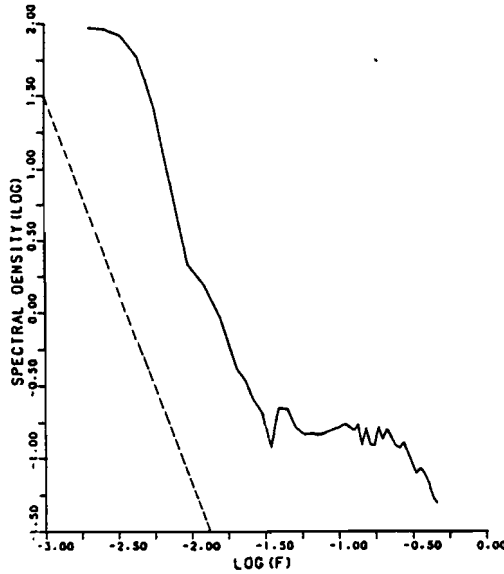


Figure 5.1 : *The atmospheric brightness temperature spectrum (double ¹⁰logarithmic).*

Apparently, there is a rather flat area around DC followed by a region that exhibits a slope of $-8/3$, indicated by the dashed line. The other (lower) flat region represents the system noise.

These measurements can be used to simulate clouds in a more realistic way than with the worst-case object used in chapters 3 and 4.

The realization of a cloudy sky from a known spectrum can be done by the following method.

The spectrum of figure 5.1 is used as an envelope for a series of harmonic components with a random, uniformly distributed phase. This means that the amplitude of the harmonics decreases with a slope of $-4/3$ until it is negligible above a certain frequency. This frequency is chosen to be 0.2 m^{-1} , according to Ref.[25] in which a minimum resolution of 5 m is presented. The flat region ends at 0.01 m^{-1} .

This signal is a slightly varying signal with zero mean. Adding a DC component of 3 K (to prevent the signal from going negative) leads to a situation that simulates a clear sky condition with a small amount of water vapour. A local cloud is created by using the same signal, but amplified with a window, to create an envelope with a continuous transition to zero at the cloud's edges, and adding one strong positive half-period of a harmonic with a frequency of 0.005 1/m , multiplied with the window, also to prevent the signal from going through zero. The window is chosen to be a Blackman window [17], but it could be any window lacking discontinuities at its edges.

This simulation leads to a sky brightness temperature as shown in figure 5.2.

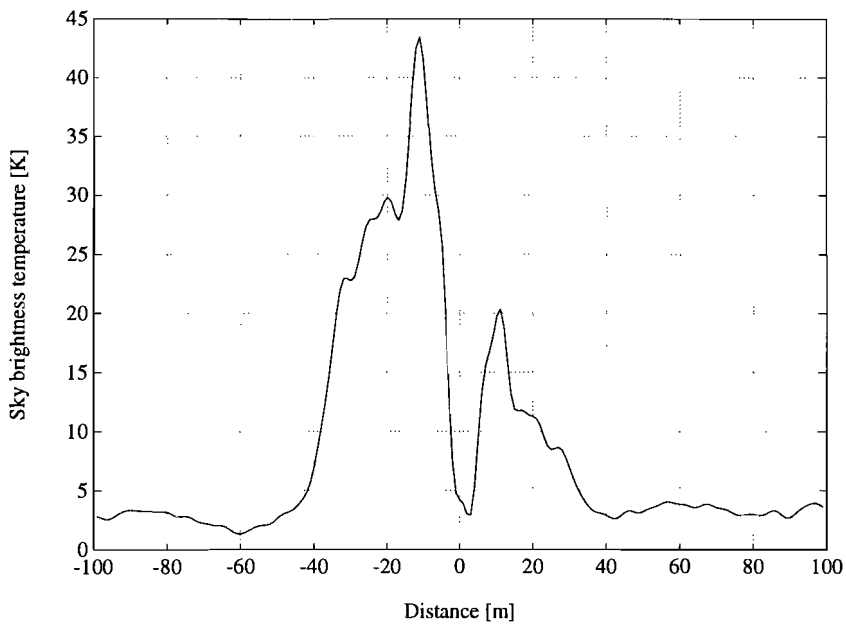


Figure 5.2 : *The simulated sky brightness temperature.*

The estimated spectrum of the brightness temperature is depicted in figure 5.3.

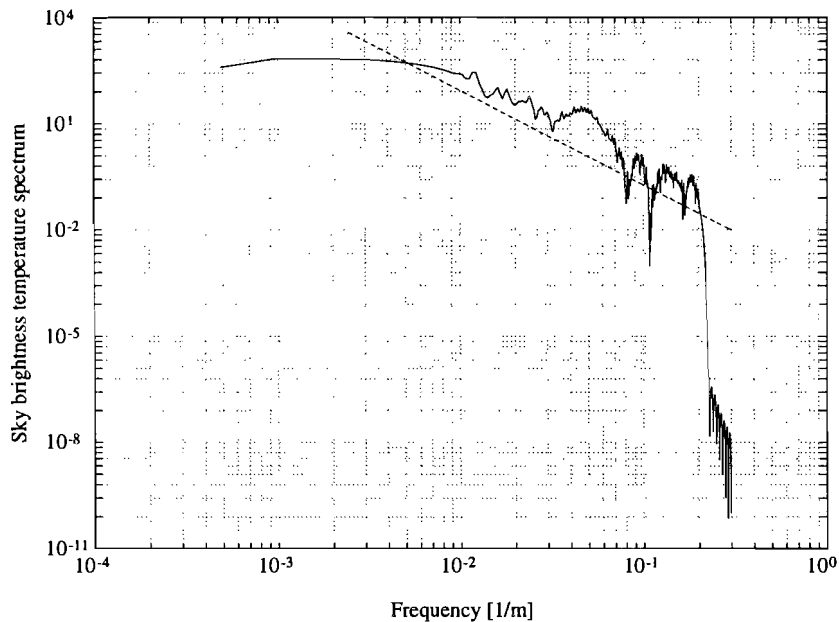


Figure 5.3 : *The simulated scenery spectrum.*

As expected, the spectrum has an envelope with a slope of $-8/3$.

This signal is processed by the radiometer and the image is created in the same way as described in chapter 2, i.e. the object is filtered by the antenna filter and noise is subsequently added by the radiometer receiver, as shown in figure 2.3, with a variance of 0.12 K^2 , corresponding to a detection error of 0.345 K .

In the same way as described in Chapter 3, the imaging quantities can be described by two ratios: one signal variance-to-noise ratio for the cloud scene in the interval from -54 m to 46 m which is 33 dB and one variance-to-noise ratio for the very small brightness temperature changes outside the cloud scene which is 7 dB . These ratios are *variance* SNR's because the value of a DC component should have no influence on the reconstruction algorithm since the imaging filter (the radiometer antenna) leaves DC signals unchanged.

The total measurement series is still 2048 m long.

This image is illustrated in figure 5.4.

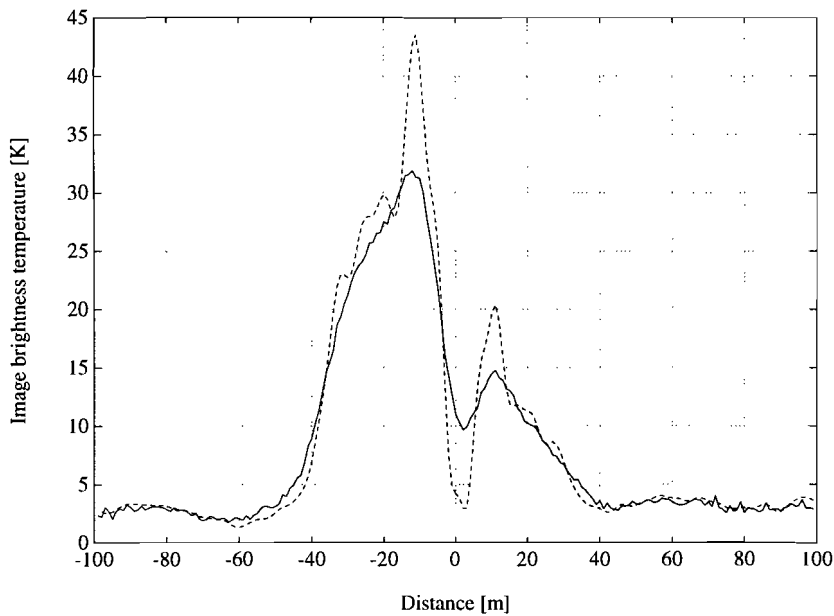


Figure 5.4 : The received image (--- object, — image).

Again it is obvious that the antenna is nothing more than a low-pass filter; the signal part of the image is a smoothed version of the object.

The spectra of both signals are presented in figure 5.5 on the next page where the object spectrum is the dashed graph.

The cut-off at 0.1 1/m is clearly visible; only noise spectral components are present there.

With this kind of object the second cause of ringing, the presence of discontinuities or other sharp edges, has been taken away since the object spectrum bandwidth is limited to 0.2 1/m .

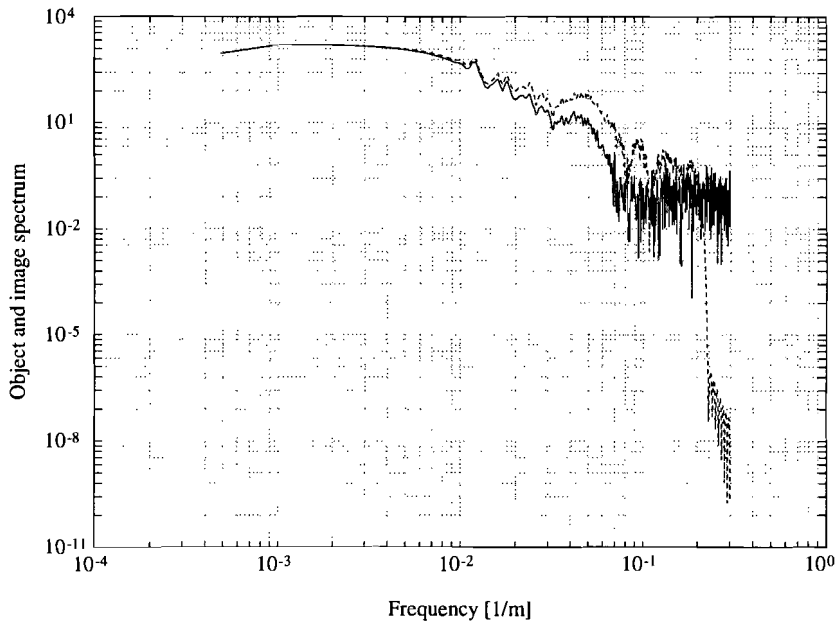


Figure 5.5 : The object and image spectrum (---- object, ——— image).

For comparison with the reconstruction methods to follow, the Wiener filtering as described in the previous chapter is applied to this object for the SNR of 33 dB. The result is shown in figure 5.6.

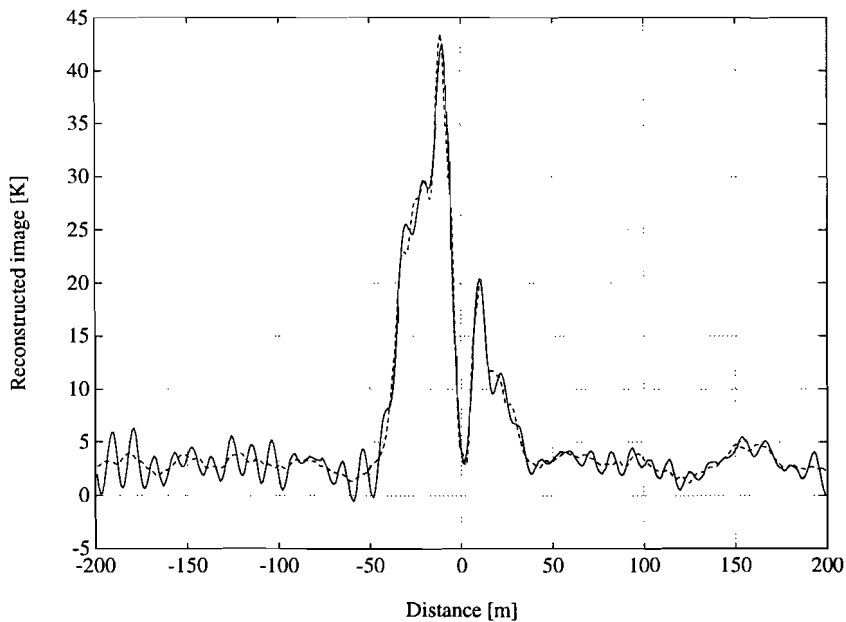


Figure 5.6 : Wiener filtering for the discussed cloud scene (---- object, ——— reconstruction).

The smoothness (limited bandwidth) of this object does not lead to excessive blurring of the reconstruction with the event SNR of 33 dB, unlike for the restoration of the previously used

object. The blurring outside the event is unacceptable however, so the SNR will be adapted. The average SNR, discussed in Chapter 3, the weighted average (lengthwise) between event SNR and non-event SNR, is 20 dB for this case. However, because of the smooth low-pass character of the object the actual SNR used can be higher; a value of 23 dB would be a good value to achieve a trade-off in restoration accuracy outside and inside the event interval.

The Wiener reconstruction for a SNR used of 23 dB is illustrated in figure 5.7.

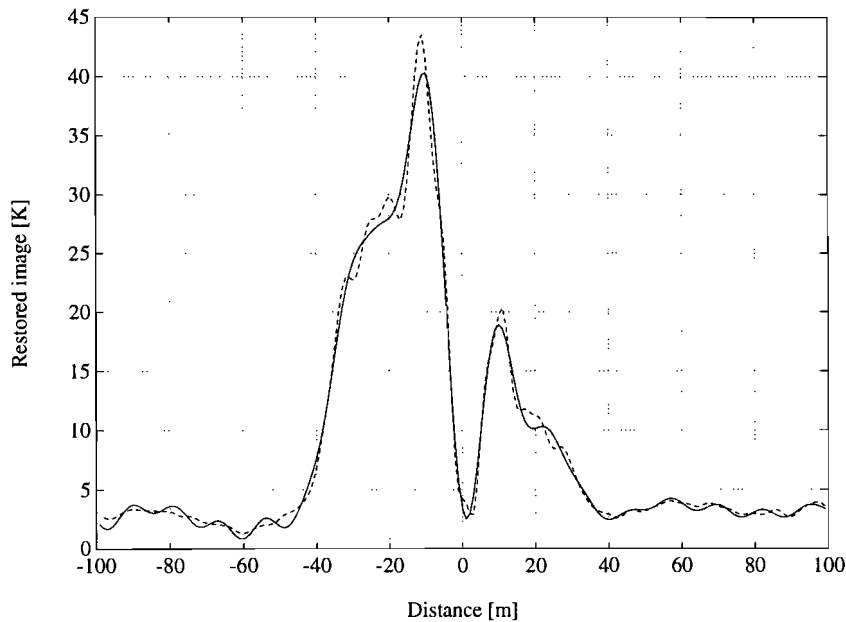


Figure 5.7 : Wiener filtering reconstruction for an SNR of 23 dB (---- object, — reconstruction).

The ringing outside the event has become acceptable.

Apparently the determination of the SNR used is a delicate case for single-event reconstructions like these. This problem will be dealt with in the next chapter, but first the designed filter will be realized with a digital filter.

5.2 Infinite Impulse Response Filtering.

The goal is to design a digital filter that processes the radiometric data in real-time in the same way the optimized analog Wiener reconstruction filter does.

The general structure of a digital filter is shown in figure 5.8.

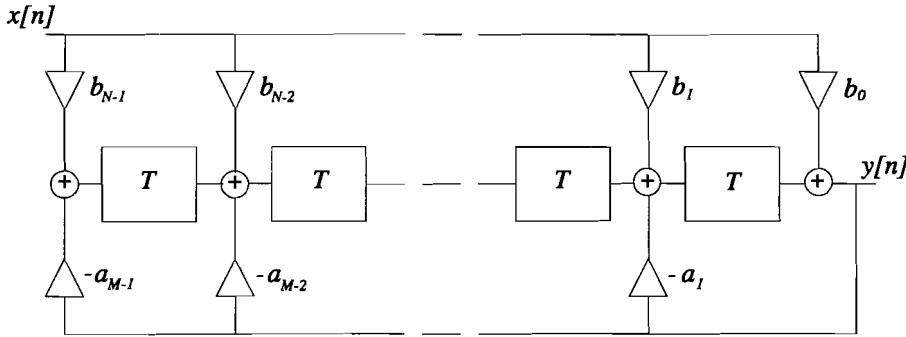


Figure 5.8: A digital filter.

This form is also called the *transposed direct form II structure*, generally referred to as the *tapped delay line*.

The filter is described by the difference equation:

$$y[n] = b_0 x[n] + b_1 x[n-1] + \dots + b_{N-1} x[n-N+1] - a_1 y[n-1] - a_2 y[n-2] - \dots - a_{M-1} y[n-M+1] \quad (5.1)$$

This general form of digital filter (all a_i 's non-zero) is also called an *Infinite Impulse Response (IIR) filter*, because the feedback of the output y_n causes an infinitely long impulse response, or the *AutoRegressive Moving Average (ARMA) filter*.

The z -transform of a discrete signal $x[n]$ is defined as

$$X(z) = \sum_{n=0}^{\infty} x[n] z^{-n} \quad (5.2)$$

The z -transform of the difference equation yields the frequency domain or transfer function model description

$$Y(z) = \frac{b_0 + b_1 z^{-1} + \dots + b_{N-1} z^{-N+1}}{1 + a_1 z^{-1} + \dots + a_{M-1} z^{-M+1}} X(z) \quad (5.3)$$

To evaluate this frequency domain, one has to realize that the z -transform is the discrete approach to the Fourier transform of the sampled version $x(nT)$ of the continuous signal $x(t)$, which leads to the following expression

$$z = e^{j\omega T} = e^{j2\pi f T} = e^{j\theta} \quad (5.4)$$

Thus, the frequency response is evaluated at the upper half of the unit circle, because the angle π corresponds to half the sample frequency, where a new period of the Fourier transform begins.

The goal is to design a digital filter that approaches the optimal reconstruction filter in the frequency domain as close as possible. Appendix A shows that the Wiener filter is an optimal feedback filter so the general feedback IIR filter seems to have promising features.

This means that the b_i 's and a_i 's have to be chosen in such a way that the response of the digital filter is fitted in a least squares way to the impulse response of the model filter.

The method used is the *Yule-Walker Method of ARMA Spectral Estimation*. The denominator coefficients are computed by the so-called "modified Yule-Walker" equations, using correlation coefficients computed by inverse Fourier transformation of the specified frequency response. The numerator is computed by a four step procedure. First, a numerator polynomial corresponding to an additive decomposition of the power frequency response is computed. Next, the complete frequency response corresponding to the numerator and denominator polynomials is evaluated. Then a spectral factorization technique is used to obtain the impulse response of the filter. Finally, the numerator polynomial is obtained by a least squares fit to this impulse response.

Since the used object no longer possesses sharp edges (which means high-frequency content) the "edge gradient" discussed in 3.2 will be very small so a window will not be necessary, because in this case it will only cause loss in resolution. The filter to be simulated will therefore be the standard Wiener filter with a signal-to-noise ratio of 23 dB.

After several try-outs, a 40th order IIR filter proved to have a magnitude frequency response that matched the specified magnitude frequency response closely enough.

This is illustrated in figure 5.9 (only for positive frequencies) on the next page. The dashed line indicates the Wiener filter.

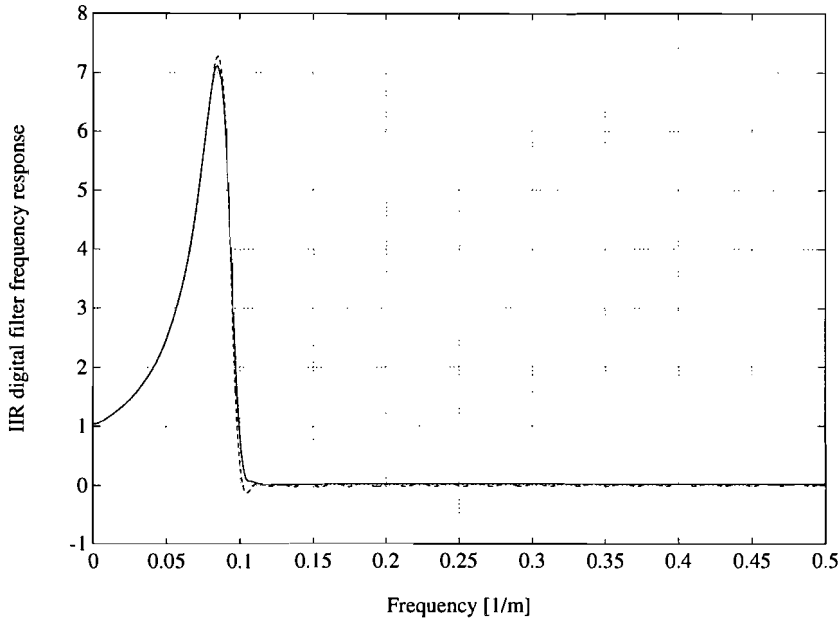


Figure 5.9 : The IIR filter frequency response (---- Wiener, — IIR).

Apparently the Yule-Walker method creates an IIR filter whose frequency response matches the specified frequency response very closely.

This filter can also be described with its pole-zero diagram, depicted in figure 5.10.

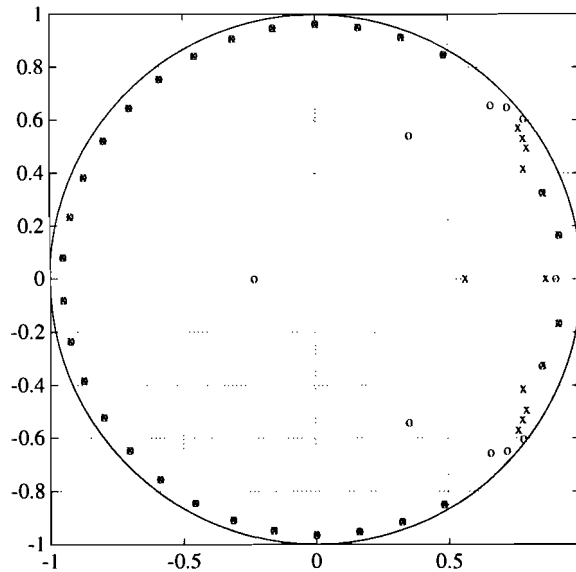


Figure 5.10 : The pole-zero diagram of the IIR filter.

The realization of the peaks and the quick drop to zero immediately afterwards is clearly visible.

Above cut-off it looks as if poles and zeros are placed upon each other, so they eliminate each other. This is not true however; the poles and zeros are placed in such a way that the frequency response remains zero without perturbations which would occur when only zeros were used above cut-off.

The IIR filter frequency response seems to match the desired response very well, but before we thrust ourselves into blind deconvolution, the main disadvantage of IIR filters has to be considered: *non-linear phase*.

The phase frequency response $\varphi(f)$ of the digital filter is shown in figure 5.11.

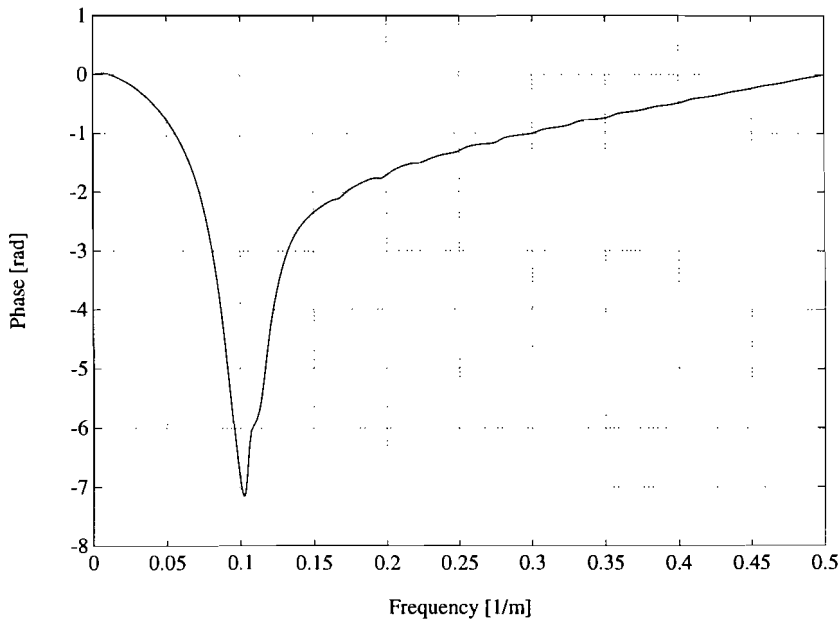


Figure 5.11 : The phase frequency response.

It is very obvious that this phase is highly non-linear which will result in significant dispersion.

The phase delay is defined as

$$\tau_p(f) = -\frac{\varphi(f)}{2\pi f} \quad (5.5)$$

and the group delay as

$$\tau_g(f) = -\frac{1}{2\pi} \frac{d\varphi(f)}{df} \quad (5.6)$$

These equations show that phase- and group delay will be equal when the phase is linear.

To indicate the effects of non-linearity the phase- and group delay of the filter are shown in figure 5.12.

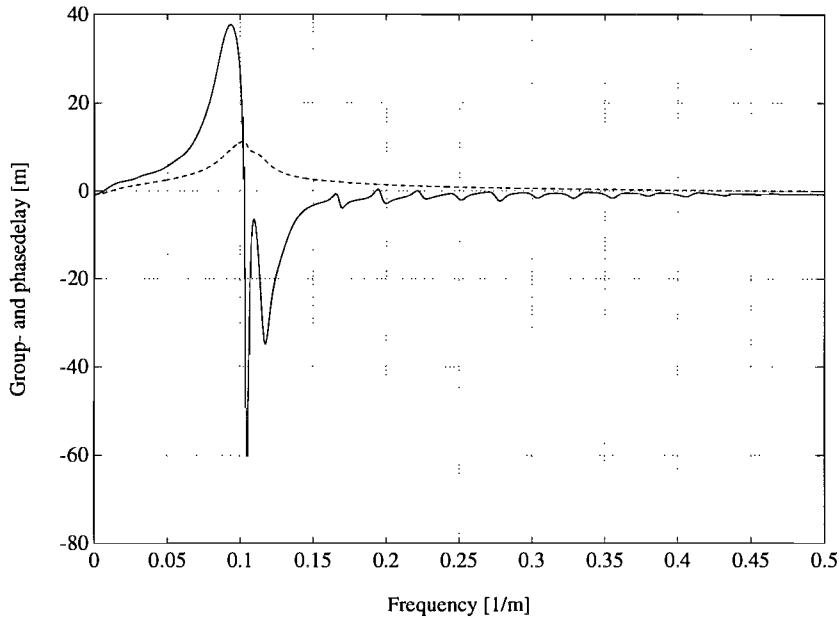


Figure 5.12 : The phase- and group delay of the IIR filter (---- phase delay,—— group delay).

The frequencies near cut-off will be delayed much more than the low frequencies and the behaviour above cut-off is a little bit capricious. The non-linearity is also the cause of the large difference between phase- and group delay.

It can therefore be expected that the reconstruction will not be as good as it would be in the continuous domain, although the phase nonlinearity will not be disastrous because combining figures 5.3 and 5.12 it appears that long before the group delay peak begins, the spectrum of the object has already dropped an approximate 30 dB.

The reconstruction using the IIR digital filter is shown in figure 5.13 on the next page.

As expected, the reconstruction is not as good as the Wiener filtering caused by the phase nonlinearity. Therefore, the other digital filtering method will be investigated.

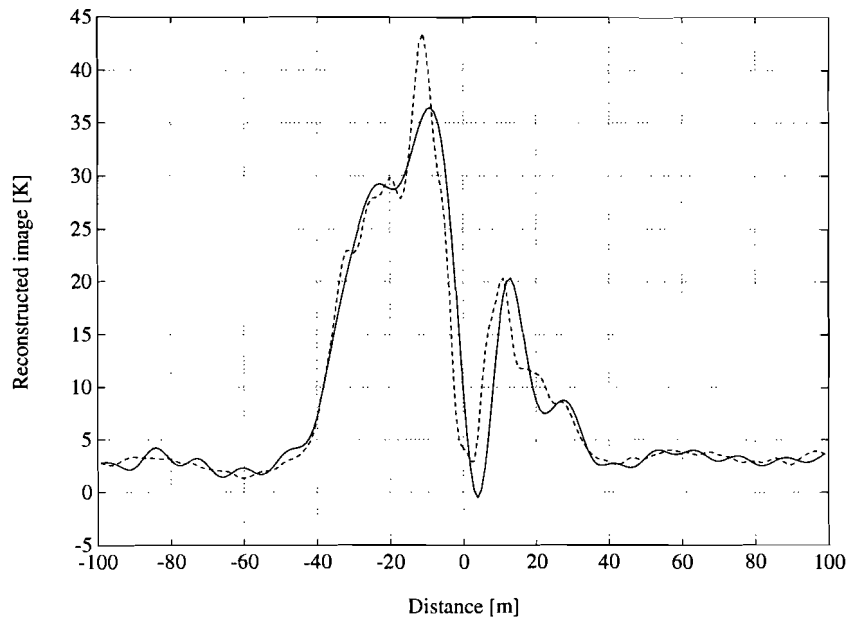


Figure 5.13 : The IIR reconstruction (---- object, ——— reconstruction).

5.3 Finite Impulse Response Filtering.

The IIR filtering seemed to be a good approach since it only needed a fortieth order filter to approach the specifications good enough. The phase nonlinearity however caused the reconstruction to fail.

A *Finite Impulse Response (FIR)* filter will be employed to overcome this problem.

The FIR is nothing but a simplification of the general IIR filter, because the only difference is that all a_i 's are zero: there is no feedback which means that the impulse response length will equal the filter length, i.e. the filter order N , which explains its name.

The FIR filter structure is depicted in figure 5.14.

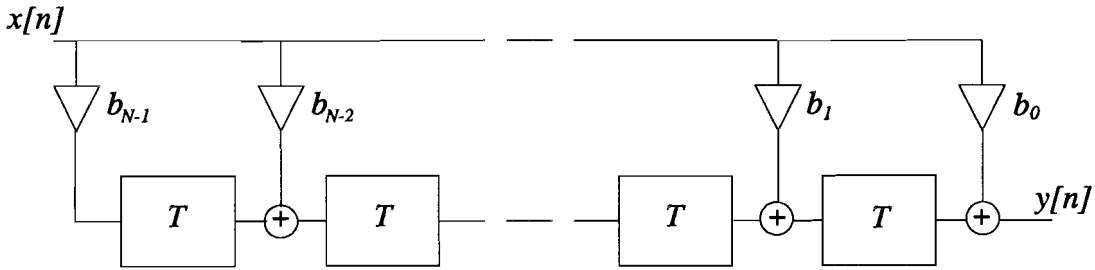


Figure 5.14 : The FIR filter.

The difference equation that describes the filter is

$$y[n] = b_0 x[n] + b_1 x[n-1] + \dots + b_{N-1} x[n-N+1] = \sum_{i=0}^{N-1} b[i] x[n-i] \quad (5.7)$$

which is the discrete convolution of the b_i 's with the input signal. This means that $b[n]$ is the impulse response.

The advantages of FIR filters are the following:

- They can have exactly linear phase.
- They are always stable.
- The design methods are generally linear.
- They can be realized efficiently in hardware.
- The filter startup transients are of finite duration.

The primary disadvantage of FIR filters is that they require a much higher filter order than IIR filters to achieve a given level of performance.

The filter coefficients are obtained by applying an inverse Fast Fourier Transform to the model filter and multiplying by a window, Hamming by default, but a rectangular window is chosen to avoid loss in resolution.

A good criterion to specify the fitting of the FIR filter to this kind of model filter is the *stopband attenuation* and the ripple on it. This is the filter transfer where the latter should be zero. This quantity is the stopband amplitude of the filter in dB's relative to the passband transfer. Other criteria would be the passband ripple and the transition width [34], but since this is no ordinary low-, high-, or bandpass filter these do not apply.

The model Wiener filter is depicted in dB's in figure 5.15.

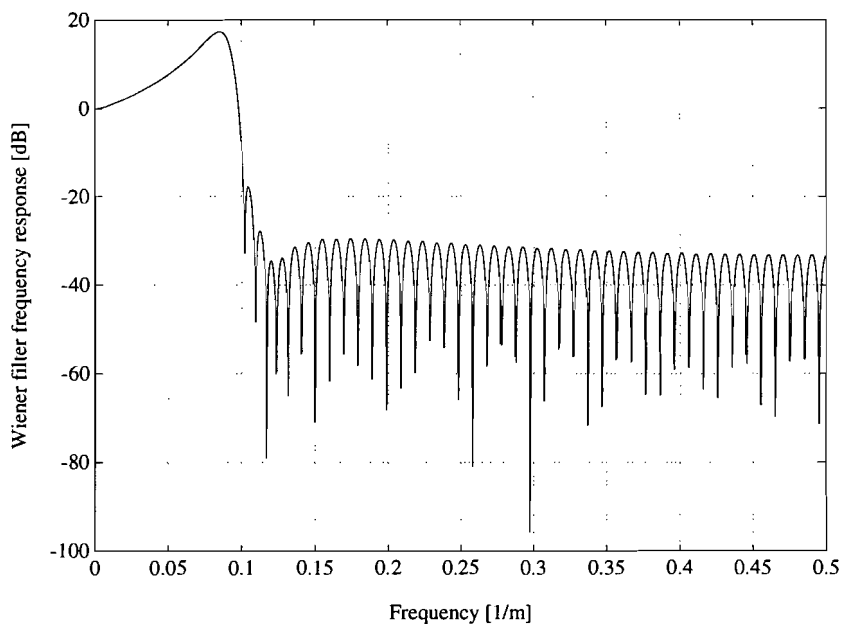


Figure 5.15 : The Wiener filter in dB's.

For simplicity the passband transfer will be taken as the DC transfer, which is unity.

From this figure it can be seen that the standard Wiener filter has an stopband equiripple of -30 dB.

Firstly, a 100th order FIR filter is used to approximate the model filter.

The FIR filter frequency response is depicted in figure 5.16 on the next page.

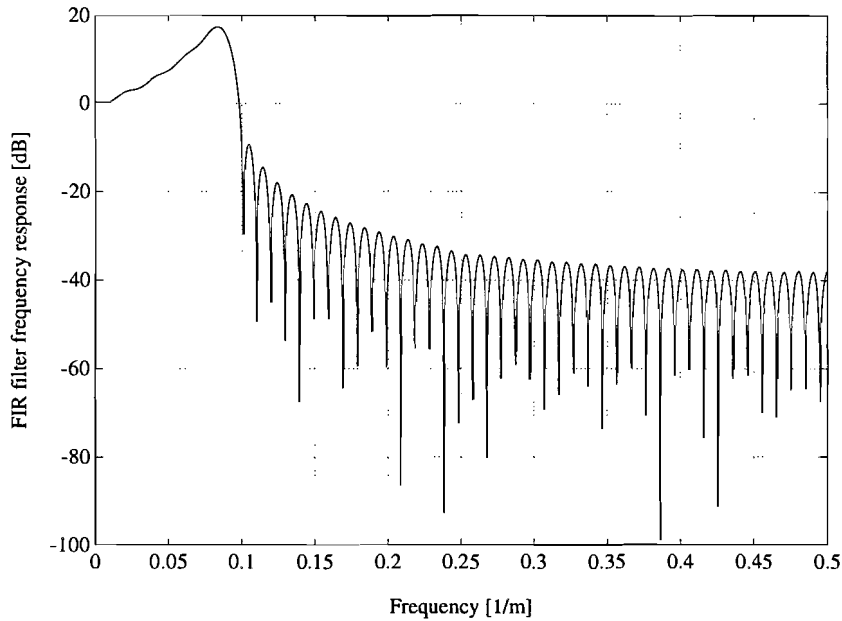


Figure 5.16 : The 100th order FIR filter frequency response.

This figure shows that the passband transfer differs slightly from the model filter, but the stopband ripple is too high just above the cut-off frequency and it is not an equiripple.

Therefore a 150th order FIR filter is tested as well on this behaviour. Its frequency response is illustrated in figure 5.17.

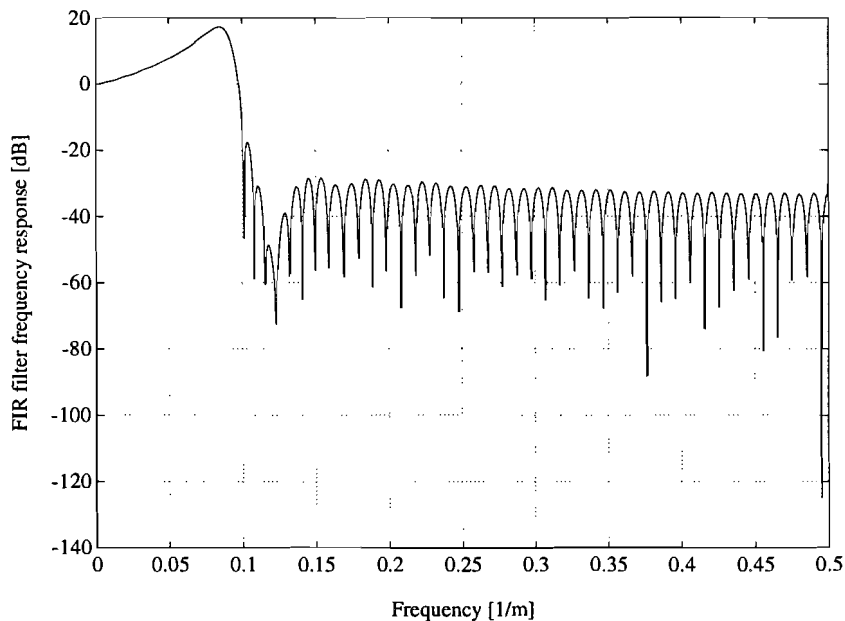


Figure 5.17 : The 150th order FIR filter frequency response.

Apparently this filter satisfies the stopband equiripple demands of -30 dB.

The frequency response of the 150th order FIR filter is, together with the Wiener filter response, shown in figure 5.18, linearly.

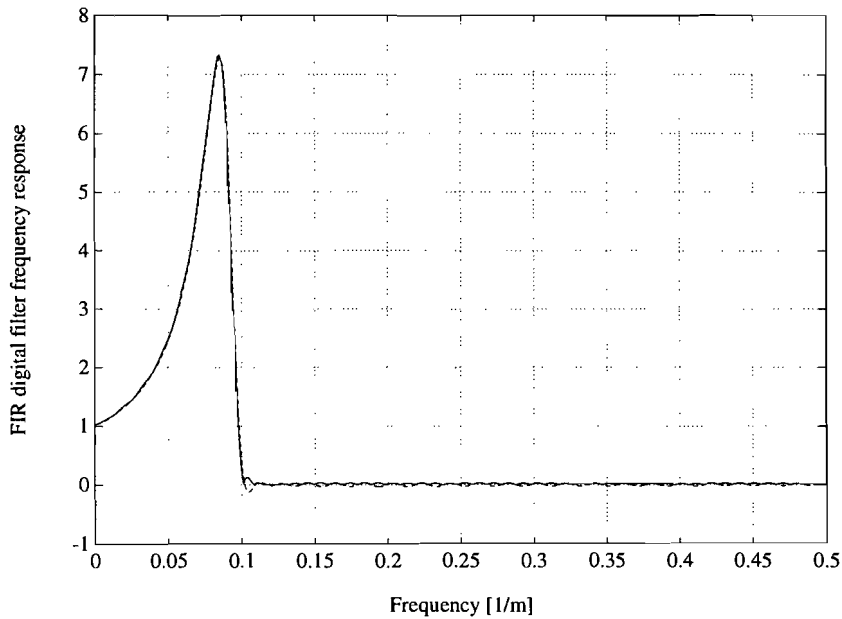


Figure 5.18 : The FIR filter frequency response (---- Wiener,— FIR).

The description in the form of the pole-zero diagram of this filter is shown in figure 5.19.

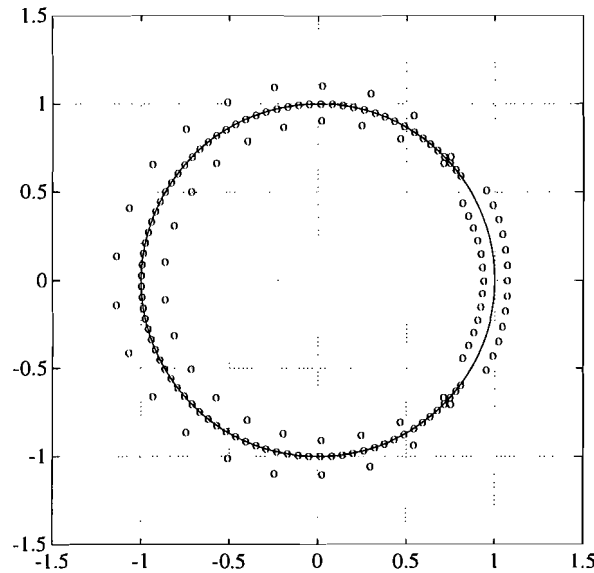


Figure 5.19 : The pole-zero diagram of the FIR filter.

Of course, this kind of filter only has zeros; that is why the order has to be so much higher because the same performance has to be achieved without having the disposal of pole-zero pairs.

The b_i 's (the impulse response) corresponding to this filter are shown graphically in figure 5.20.

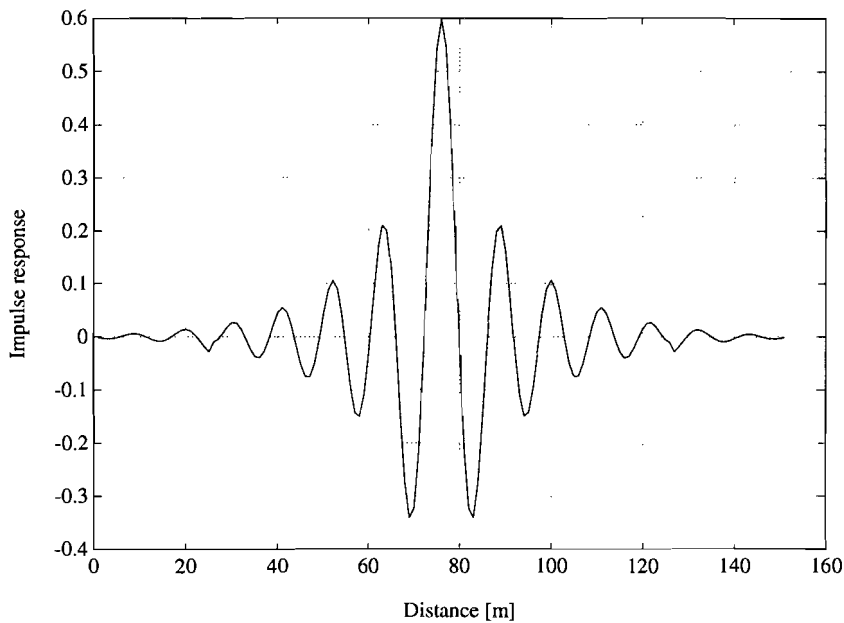


Figure 5.20 : The FIR filter impulse response.

From this impulse response can already be concluded that the FIR will cause a delay of 75 m.

To illustrate the statement that FIR filters exhibit linear phase, the phase frequency response of the filter is shown in figure 5.21.

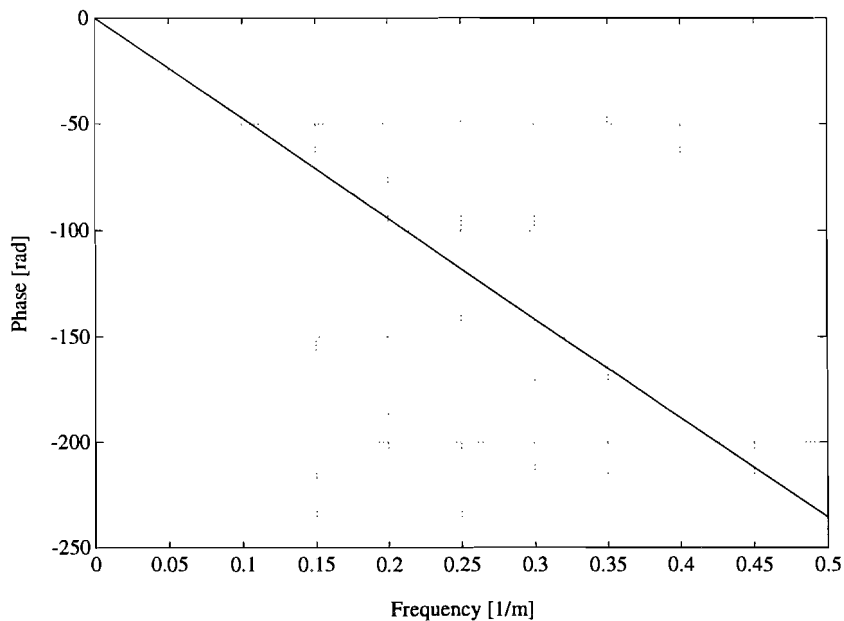


Figure 5.20 : The phase frequency response.

As a result of the phase linearity group- and phase delay are the same, namely 75 m, which is exactly half of the filter order (assuming a sample distance of 1 m).

The reconstruction will therefore not fail because all frequency components will be delayed by the same amount.

This reconstruction is shown in figure 5.22.

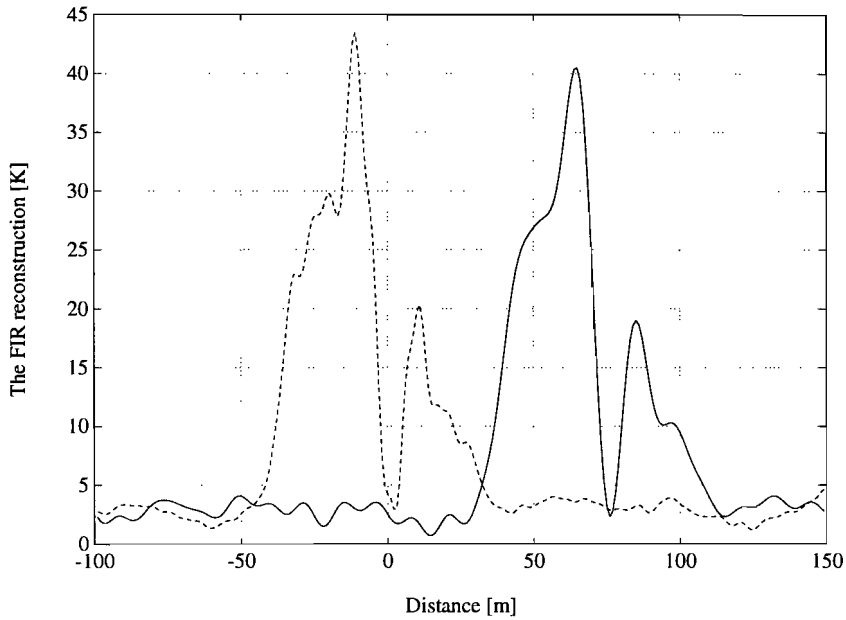


Figure 5.22 : *The FIR filter reconstruction (---- object, — reconstruction).*

As expected, the reconstruction is as good as continuous Wiener filtering with a delay of 75 m.

For a more fundamental insight into the reconstruction, it is interesting to see what the algorithm affected the spectrum of the image (shown in figure 5.5).

The spectrum of the reconstructed object and the spectrum of the object itself are represented in figure 5.23 on the next page.

Within the image bandwidth, the spectrum of the reconstructed object approximates the object spectrum very well, but beyond the cut-off frequency the only thing that is present is noise, but its amplitude is strongly attenuated.

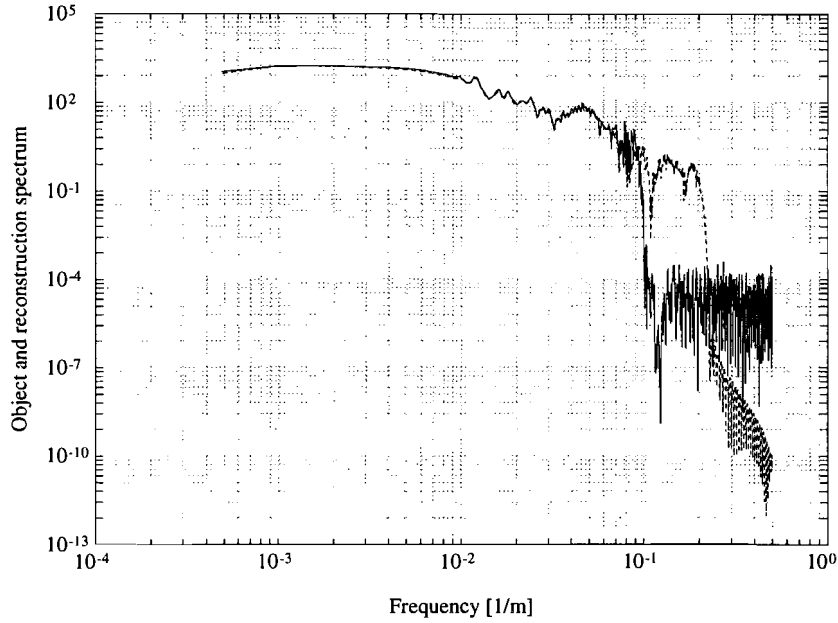


Figure 5.23 : The spectrum of the object and its reconstruction (---- object, ——— reconstruction).

The reconstruction has been performed as well for other realizations of the object with the spectrum defined in Chapter 5.1.

Figures 5.24 and 5.25 show the result of their reconstruction.

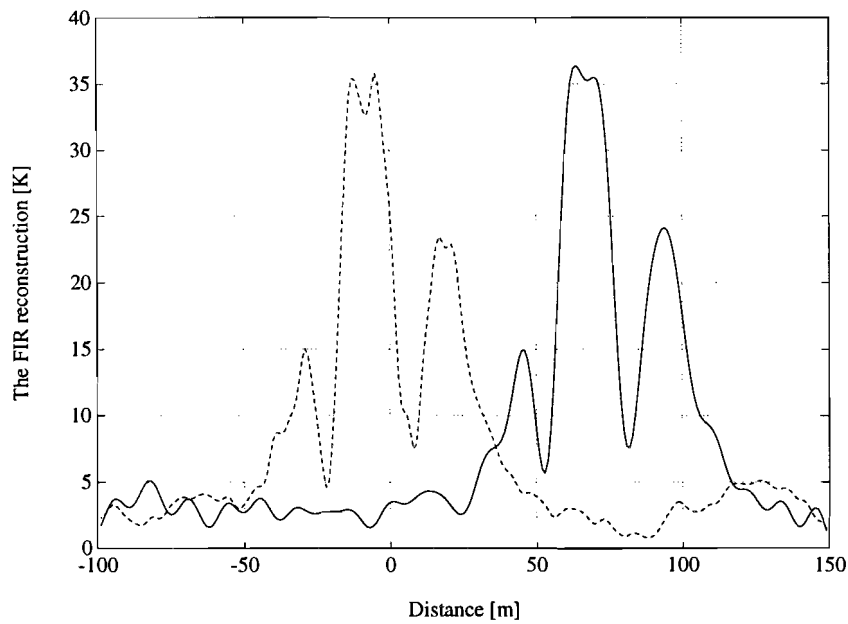


Figure 5.24 : The FIR reconstruction on another realization of the object (---- object, ——— reconstruction).

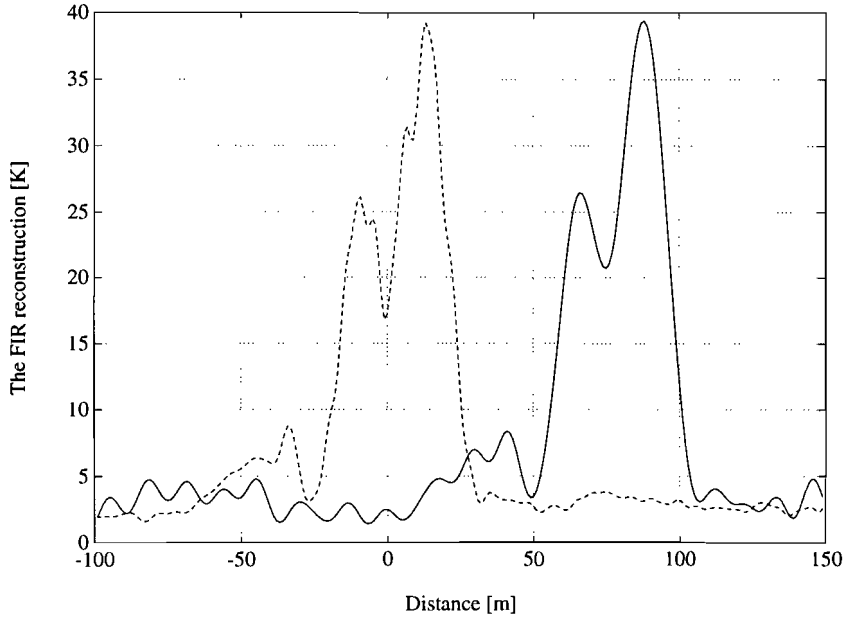


Figure 5.25 : The FIR reconstruction on another realization of the object (---- object, ——— reconstruction).

5.4 The reconstruction error.

After the conclusion of Chapter 3 that for this (almost) triangular transfer function the resolution enhancement is maximally 2, it is also interesting to throw a glance at the theoretical reconstruction error between the object and its estimation (not to be confused with the measurable reconstruction error between the image and the estimated image discussed in the previous chapter).

This error is given by Eq.(4.3):

$$\epsilon_o^2 = \int_{-\infty}^{\infty} \left\{ |1 - S_{net}(f)|^2 \Phi_o(f) + |Y(f)|^2 \Phi_n(f) \right\} df \quad (5.8)$$

The absolute minimum reconstruction error that can be made by the reconstruction is the error made when the signal-to-noise ratio approaches infinity; the reconstruction will then fully restore all frequency components in the image band as in inverse filtering where Ω_p will approximate Ω . Since there is no noise, the reconstruction error discussed in Chapter 3.3, Eq.(3.20), will just be the missing signal power (with $\Omega = 2\pi f_c$):

$$\epsilon_o^2 = 2 \int_{f_c}^{\infty} \Phi_o(f) df \quad (5.9)$$

When this calculation is performed on the object discussed, the result is that the error ε_o will be 0.23 K.

It will be interesting to see how the relation of the total reconstruction error and the signal-to-noise ratio is. With the help of Eq.(4.3) this relation is analyzed, also for a cut-off frequency which is twice as high (i.e. an antenna of double size), i.e. for $f_c=0.1 \text{ m}^{-1}$ and $f_c=0.2 \text{ m}^{-1}$. The result is shown in figure 5.26.

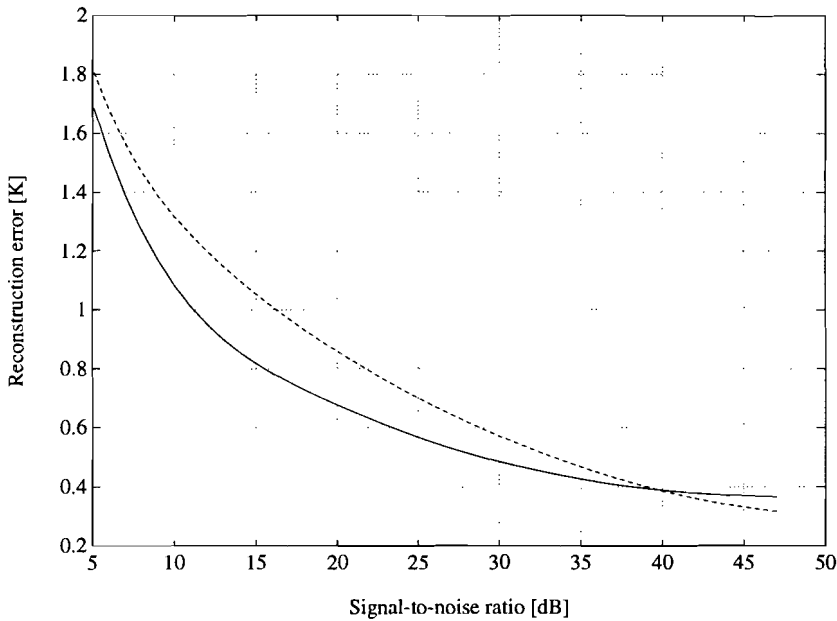


Figure 5.26 : The reconstruction error as a function of SNR (— $f_c=0.1 \text{ 1/m}$, --- $f_c=0.2 \text{ 1/m}$).

This result was to be expected: the less noise, the more in-band frequency components can be restored. The absolute minimum discussed earlier will never be reached, however, because for extremely high signal-to-noise ratios (in the order of 80 dB) the very small amount of noise that is present will be amplified by the huge peaks in the restoring Wiener filter so the error will increase again. This effect is tested by calculating the error using only the second integrand in Eq.(5.8). When only the first integrand is used, the error asymptotically reaches the absolute minimum of 0.23 K.

This noise effect for high SNR's is not shown in the figure, because SNR's like these do not apply.

This in-band noise is also the reason that the error for a double cut-off frequency is not remarkably less. It is even higher in the first region. This is due to the double noise bandwidth that is allowed into the estimation which cancels the gain of signal frequency components between 0.1 and 0.2 m^{-1} because these represent only small rapid variations of the signal; their power is only a fraction of the power that is contained in the frequency band up to 0.1 m^{-1} . As the SNR increases this noise influence will decrease so the error due to missing signal frequency components will dominate the reconstruction error, which will lead to lower values of the reconstruction error for a cut-off frequency of 0.2 m^{-1} . This is very interesting, because it implies that a higher resolution obtained by a bigger antenna will

not necessarily lead to a better reconstruction! An optimum antenna size, leading to an optimum trade-off between in-band noise propagation and resolution enhancement has to be used.

The absolute minimum error in Eq.(5.9) for this specific cut-off frequency will be zero since the imaging bandwidth will include just the whole object bandwidth of 0.2 m^{-1} .

Figure 5.27 illustrates the abovementioned noise effect for a doubled cut-off frequency. The fact that the error for double cut-off frequency tends to go lower for high SNR's.

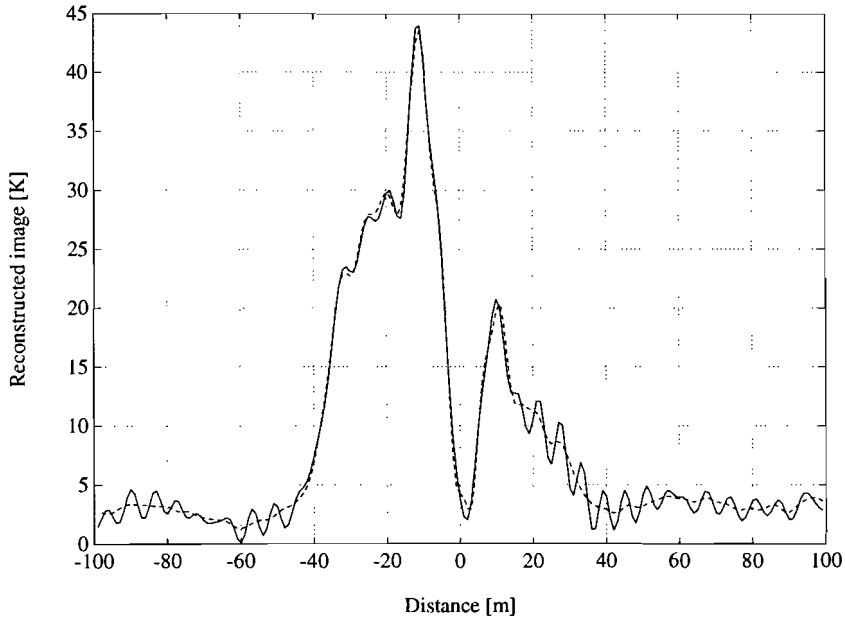


Figure 5.27 : The Wiener reconstruction for double cut-off frequency
(---- object, ——— reconstruction).

This error can also be calculated directly from the reconstruction itself in the spatial domain. For a finite interval, the error between the object $o(x)$ and its reconstruction $\hat{o}(x)$ is defined as follows:

$$\epsilon_o = \sqrt{\left\langle (o(x) - \hat{o}(x))^2 \right\rangle} \quad (5.10)$$

When this is applied to the object and image of figure 5.4 (thus pretending as if the image is the estimation of the object), assuming ergodicity to be able to perform the calculation, the error is 0.8 K; this was calculated however for the *whole* measurement interval of 2048 m. When the same is done for the event interval [-54 m, 46 m] the error is 3.1 K. This is explained by the fact that before deconvolution the error is contributed to mainly in the image, see figure 5.4. The error *energy* would of course remain practically the same then.

Wiener filtering with the SNR of 23 dB yields an error of 0.64 K for the long interval, which could already be seen from figure 5.26 (the error obtained by the two methods has to be the same according

to Parseval's theorem), and 1.26 K for the event interval. In contrast to the image, where the error is mainly made in the event, the error energy after deconvolution is spread over the entire interval. That is why the error for the long interval is not very much smaller than for the short interval as could be expected since it is divided by a larger interval. The error energy will thus be much larger for the long interval.

Performing the same calculation on the FIR filter, with correction for the delay, the error is also 0.6 K for the long interval and 1.1 K for the short interval.

These calculations have been performed on several realizations of the object, and the result was every time practically the same.

Apparently the discretization did not result in loss of reconstruction capacity. Since the nonlinearity of the IIR filter makes it impossible to correct for the delay, the error cannot be calculated in an illustrative way.

The quite big difference between minimum error and the actual error is due to the not-rectangular overall filter, causing in-band frequency components to be missing and the presence of noise which is even amplified by the Wiener filter peaks. This is also the reason that the error is higher than the noise variance of 0.345 K.

Chapter 6

Adaptive Filtering

Judging from figure 5.23, the FIR reconstruction is as good as the Wiener reconstruction, but the reconstruction can be better.

From the previous analysis can be concluded that the noise is the main evil in the reconstruction algorithm, the noise which is represented in the filter in the signal-to-noise ratio used. For single-event cases this leads to ambiguity: should the SNR corresponding to the event only or to the whole measurement interval be used? The length of the interval that is used to determine the SNR should have no influence on the reconstruction.

The use of an average SNR yielded satisfying results, but the trade-off between restoring accuracy inside and outside the event was a limiting constraint.

When the low-signal part (a clear sky part) is regarded it appears that oscillatory blurring occurs, stemming from the amplification of low-frequency noise. This means that the signal-to-noise ratio used in the Wiener filter is too high for that part of the signal.

On the other hand, when the high-signal part (a cloud) is regarded, it can be seen that too rapid changes cannot be followed. This is mainly caused by the fact that frequencies above cut-off can never be retrieved (loss in resolution), but also because the signal-to-noise used ratio is too low for that part of the signal causing only partial restoration of the frequencies below cut-off (see figure 4.2).

The maximum resolution gain of 2, discussed in chapter 3, will therefore never be reached with a FIR filter using a fixed signal-to-noise ratio. The abovementioned observations however give a clue of how to achieve better reconstruction: adapt the signal-to-noise ratio used to the momentary value of the received signal in order to achieve a continuous optimal trade-off between resolution enhancement and noise suppression.

This means that a possible single-event case will be converted into smaller sections within which the choice of the interval does not influence the value of the corresponding SNR.

The principle of this kind of adaptive filtering is easy: the signal variance-to-noise ratio of a sequence of samples W is calculated (the DC component is firstly removed for the reasons mentioned earlier), the FIR Wiener filter tapset based on that ratio is installed and the received signal is filtered with it.

The first method is a non-moving average adaptive filtering technique.

After W samples a new set of W samples is received, the signal-to-noise ratio is again calculated and the taps change into the new filter.

The sequence W has to be as small as possible to prevent the signal from changing too much in that interval to calculate a representative signal-to-noise ratio. The length of the sequence used will then be much smaller than the length of the impulse response, N .

Let's take a closer look at the FIR filtering principle, which is nothing more than the discrete convolution

$$\hat{o}[n] = \sum_{k=0}^{N-1} h[k] i[n-k] \quad (6.1)$$

in which $i[n]$ is the sampled received image, $h[n]$ is the impulse response of the FIR reconstruction filter and $\hat{o}[n]$ is the reconstructed object.

This convolution can be represented graphically like in figure 6.1 on the next page.

The signal $h[k]$ represents the values of the taps of the filter. The signal $i[n-k]$ is depicted as a function of k on the left, here for $n=0$, and it moves for increasing n into the filter in the direction of the arrow. Eq.(6.1) shows then that for every n only the non-zero $h[k]$'s and $i[n-k]$'s contribute to $\hat{o}[n]$. This means that the tapset corresponding to the indicated sequence W will be the most effective when the sequence W finds itself in the main lobe of the impulse response, which is nothing more than an explanation of the delay of half the filter length of an FIR filter.

The question is: what should the value of W be?

On one hand it should be so large that it covers the main lobe of the filter's impulse response. When the width of the impulse response's main lobe is defined as the distance between the two first minima, this width will be 14λ (i.e. 15 samples). On the other hand it should be so small that the signal doesn't change appreciably. When for this distance is chosen the inverse of the maximum signal

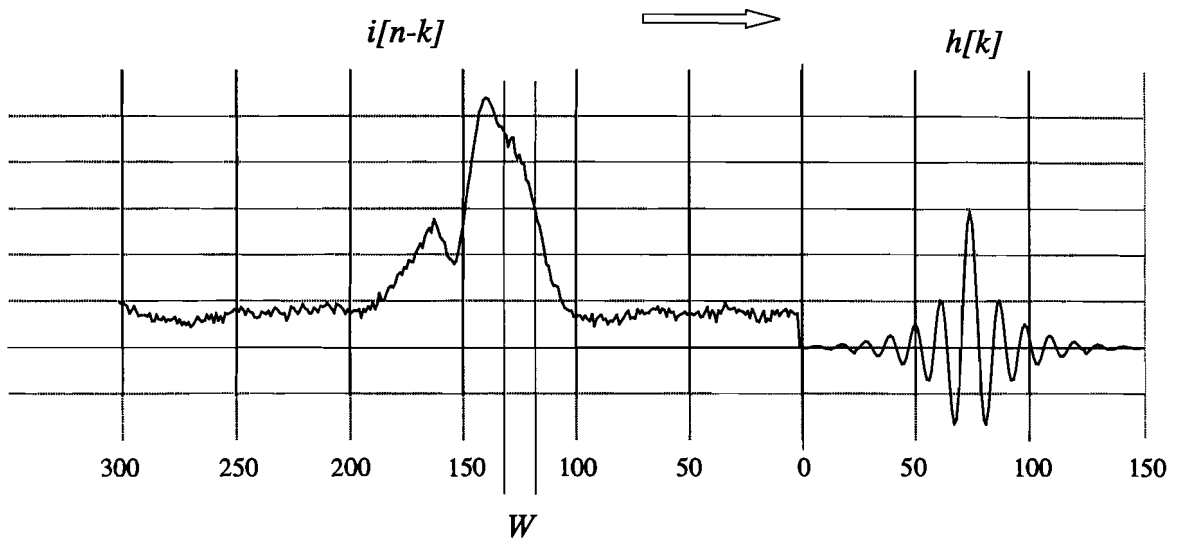


Figure 6.1 : Graphical discrete convolution.

frequency it is $1/0.2=5$ $m=5$ samples. A good value for W would be 10 then. This is also more realistic than 5 because the signal from which the signal-to-noise ratio is extracted is the image whose maximum frequency is the cut-off frequency of the imaging filter, which is 0.1 1/m.

The other question is: how are the tapsets to be adjusted to the received signal-to-noise ratio?

The solution is to dispose of a number of tapsets from which one is to be chosen if the received signal-to-noise ratio lies between a corresponding upper and lower limit. To achieve a not too abrupt transition between two successive tapsets, which would lead to discontinuities in the reconstruction, not too few different tapsets are chosen. The design of the filters is such that the different impulse responses are evenly spaced. A criterion for this even spacing could be that the maximum of these responses increase linearly.

The smaller W will be, the higher the highest signal-to-noise ratios will be. When a W of 10 is chosen, the highest signal-to-noise ratios are in the order of 40 dB for the kind of signals that are used. It can be expected that the filter characteristics will not react significantly to changes in signal-to-noise ratios as high as this. Therefore the division of the signal-to-noise ratio domain will not be linear to create a set of evenly spaced impulse responses.

The primary goal of the adaptive filter is to distinguish between a high power event and the small brightness temperature variations outside an event, in such a way that they are both accurately reconstructed.

After several experiments the SNR of the non-event area of the object never exceeded 17 dB. Therefore the first tapset is for every SNR below 17 dB and the SNR used in the filter is 10 dB because the only thing the filter has to do is suppress the strongly present noise.

For the next SNR class the SNR used is closer to the lower interval boundary in order to achieve noise suppression. The higher the SNR's will be, the more the SNR used will be closer to the upper interval boundary to stimulate resolution enhancement, because there is practically no noise that can be disturbingly amplified. For extremely high SNR's the SNR used can be even higher than the upper limit. This approach can be compared to an adaptive Backus-Gilbert approach where the Lagrange multiplier is constantly adapted to the signal.

It appeared that a linear increase of the SNR interval boundaries in dB's yielded a satisfactory linear spacing of the impulse responses.

The division to be used is represented in table 6.1.

Table 6.1 : The tapset division (all values in dB's).

Tapset	Lower SNR limit	Upper SNR limit	Used SNR
1	$-\infty$	17	10
2	17	20	17
3	20	23	21.8
4	23	26	24.8
5	26	29	27.8
6	29	32	31.5
7	32	35	35
8	35	38	38.5
9	38	41	41.5
10	41	∞	44.5

The remark has to be made that the calculated signal-to-noise ratio is not the real one, because the signal power is the image power, which is the object power filtered by the antenna, plus noise power. This noise power can be easily removed by subtracting unity from the calculated SNR. Thus, the true SNR would be higher because of the antenna low-pass filtering effect. The high frequencies are mainly in the high signal area however, and for this area the SNR used is chosen higher.

These tapsets or impulse responses are shown in figure 6.2, where the higher impulse responses represent the tapsets with the higher SNR's.

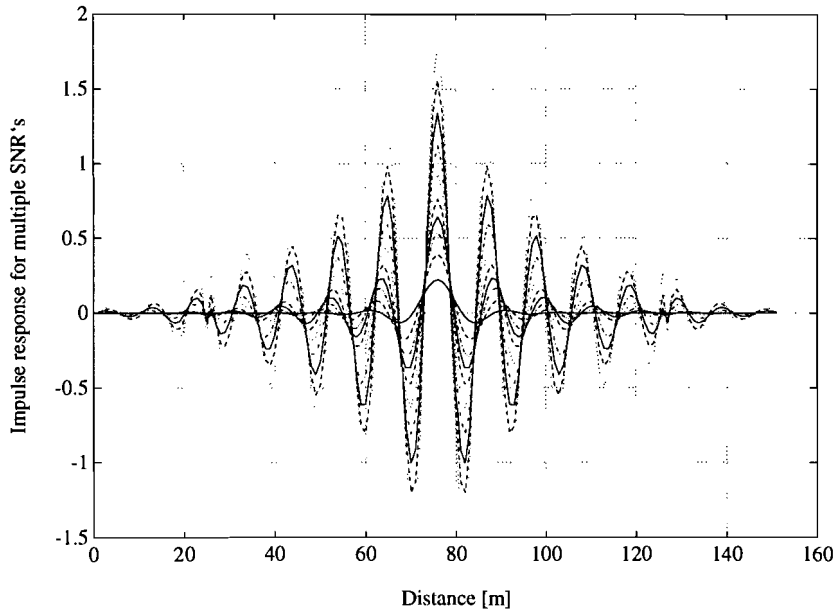


Figure 6.2 : *The used FIR tapsets.*

As expected the impulse responses at high SNR's do not respond much to changes in the SNR and the impulse responses are linearly spaced.

Firstly, an adaptive reconstruction with a W of 10 samples is performed. The result of this reconstruction is shown in figure 6.3.

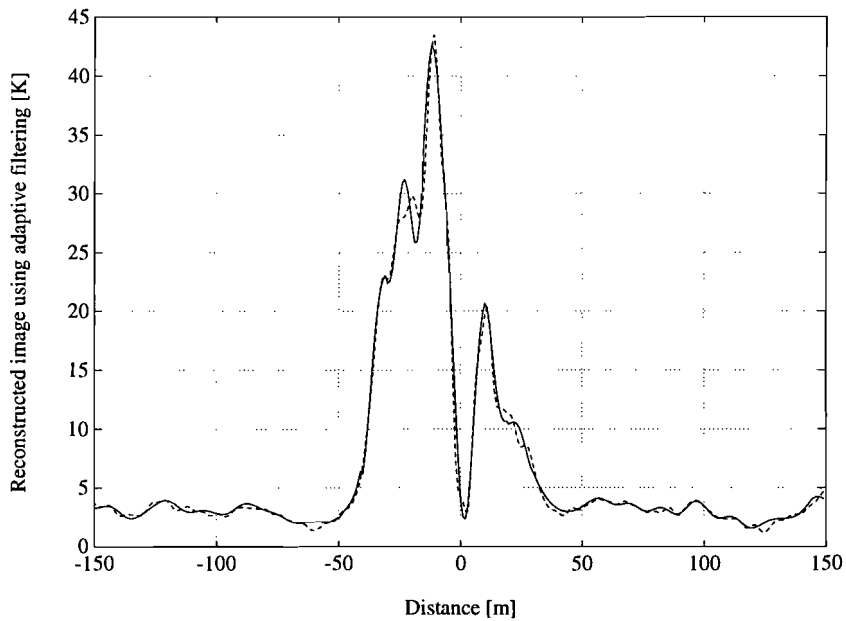


Figure 6.3 : *The adaptive reconstruction with $W=10$ (---- object, ——— reconstruction).*

This shows that this value of W leads to a very good reconstruction.

The reconstruction error over the whole interval is 0.47 K, which comes closer to the minimum than for non-adaptive filtering. The error over the shown interval is 0.8 K. This is caused because the error outside the event hardly contributes to the overall error.

According to figure 5.26, when this result of 0.45 K would be obtained by Wiener filtering the corresponding SNR would be 31 dB, a gain of 8 dB!

When W will be increased the transition between two succeeding tapsets will be more abrupt (one or more classes can be skipped), leading to discontinuities at the beginning of a new sequence.

In figure 6.4 the result of an adaptive reconstruction with a W of 25 is represented.

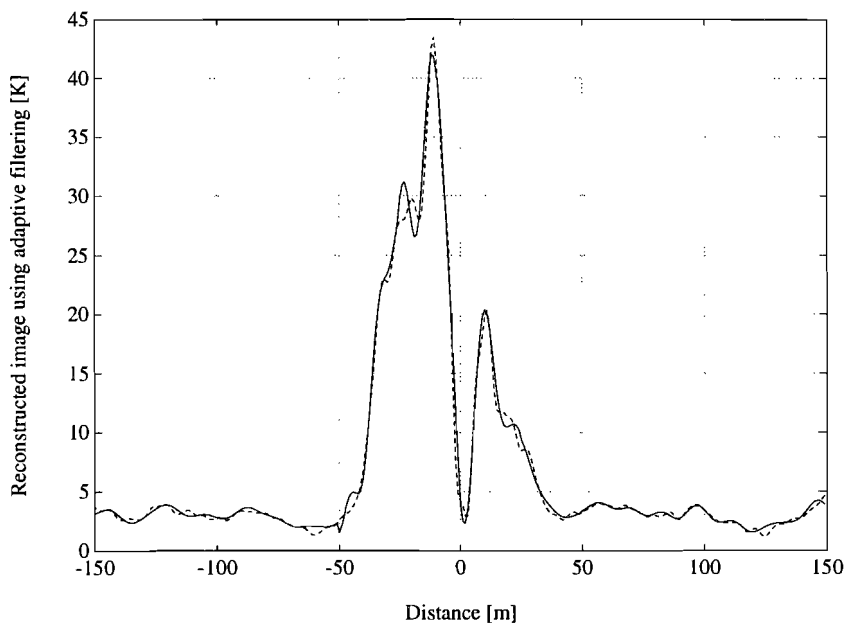


Figure 6.4 : The adaptive reconstruction with $W=25$ (---- object, — reconstruction).

The discontinuities (e.g. at -50 m) caused by the abovementioned abrupt filter transitions are becoming visible. The reconstruction error in this case is 0.48 K for the whole interval and 0.83 K for the shown interval.

For comparison, the reconstruction with a W of 50 has been performed as well, as shown in figure 6.5 on the next page.

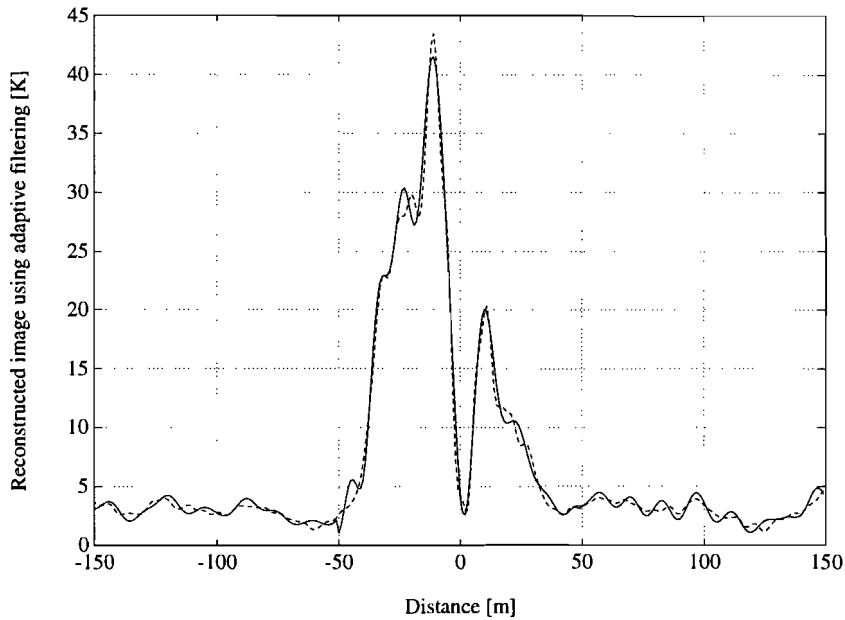


Figure 6.3 : The adaptive reconstruction with $W=50$ (--- object, — reconstruction).

Now the discontinuities have become very conspicuous, The reconstruction error is 0.52 K for the whole interval and 0.9 K for the shown interval.

In this method, the transition between two chosen classes can be quite large: the next chosen tapset is not necessarily the next one in line, but one or more classes can be skipped. For $W=10$ this will hardly be the case, but there is a more elegant way to avoid this.

This way is to use pure *moving average* adaptive filtering, which means that for *every* newly received sample the SNR for the last W samples is calculated and that the corresponding tapset is installed when the middle of the regarded interval finds itself in the middle of the filter. In this manner, the next chosen tapset is *always* (for continuous low-pass signals like the one used) one higher or lower, so discontinuities will not visibly occur. When even more tapsets are used, which means that they will be more closely spaced, the reconstruction will be free of any kind of discontinuity.

Figure 6.6 shows this kind of reconstruction for $W=10$.

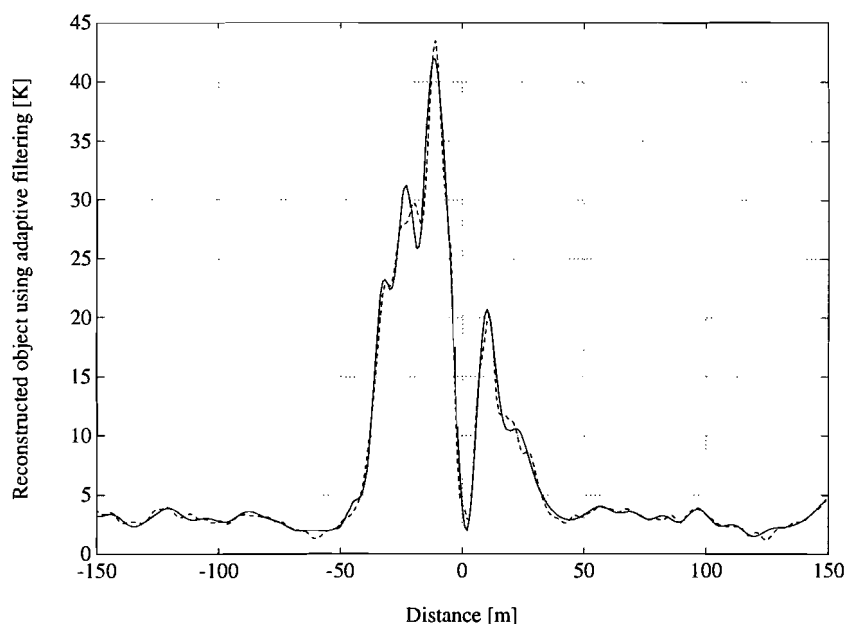


Figure 6.6 : The moving average adaptive reconstruction for $W=10$ (---- object, — reconstruction).

Apparently there is very little difference between this kind of adaptive filtering and the one discussed earlier. The reconstruction error is 0.46 K for the whole interval and 0.82 K for the shown interval.

Figure 6.7 shows the reconstruction for $W=25$.

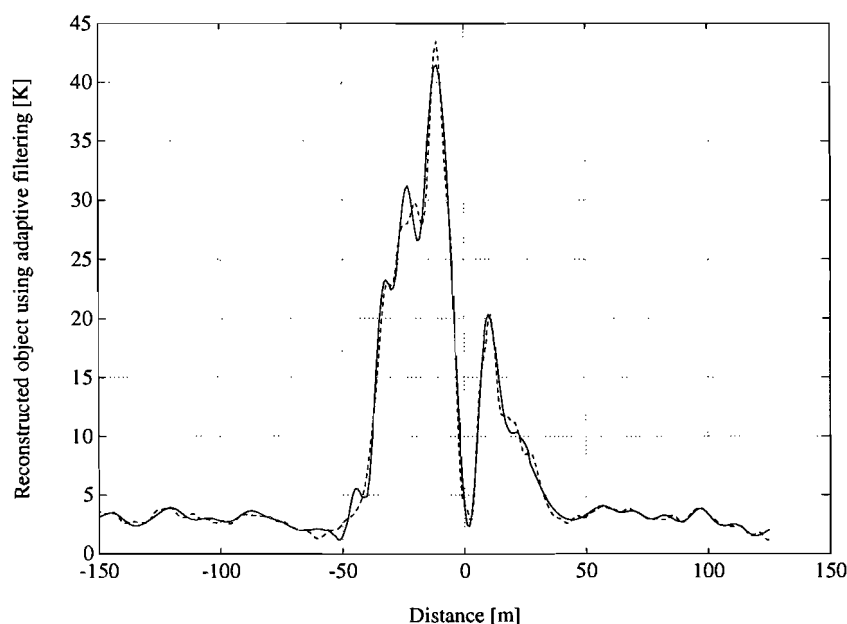


Figure 6.7 : The moving average adaptive reconstruction for $W=25$ (---- object, — reconstruction).

The reconstruction error is 0.47 K for the whole interval and 0.83 K for the short interval.

Apparently, there is negligible difference between the adaptive reconstruction for $W=10$ and $W=25$.

Figure 6.8 shows the moving average reconstruction for $W=50$.

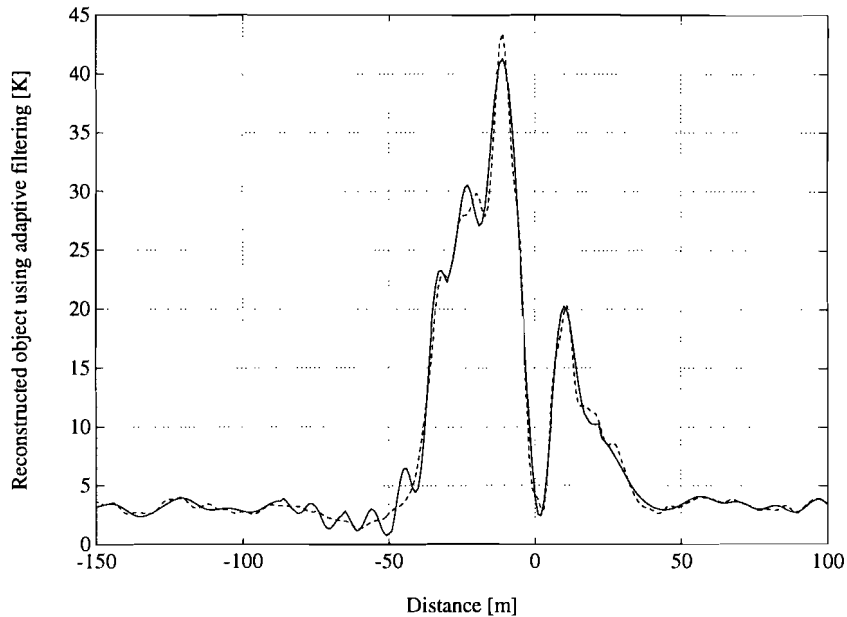


Figure 6.8 : The moving average adaptive reconstruction for $W=50$ (---- object, ——— reconstruction).

The reconstruction error is 0.51 K for the long interval and 0.91 K for the short one.

As could be expected, the discontinuities in these estimations have disappeared.

Both methods show that a W of 50 yields not as good a result as a W of 25 or 10. This was to be expected because within a width of 50 m the interval ambiguity is clearly present.

When both methods are identical in their reconstruction quality, it seems better to use the moving average adaptive filtering since it is more elegant, easier to implement and it will respond more smoothly to sudden variations in signal strength.

Since both methods yield practically the same result, only the spectrum of the moving average adaptive filtering with $W=10$ is calculated. The result is shown in figure 6.9 on the next page.

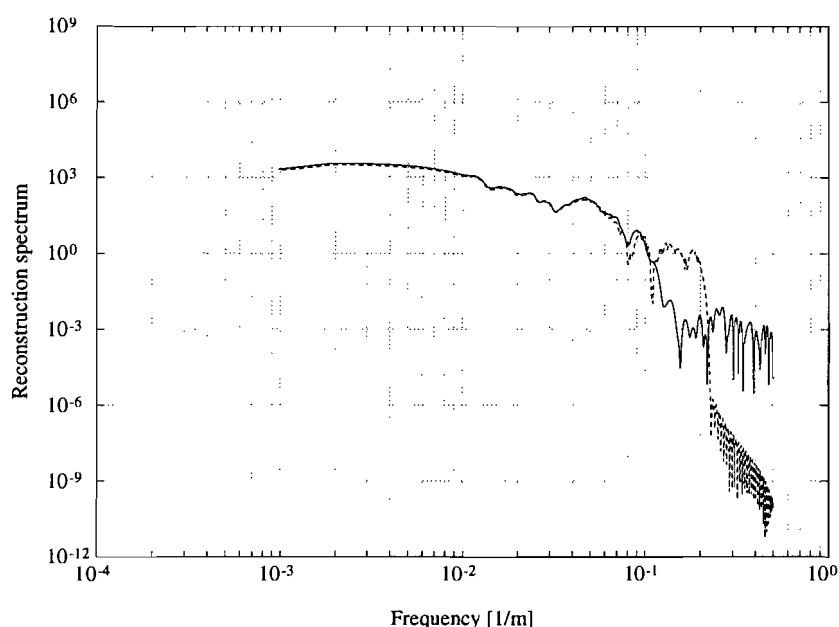


Figure 6.9 : The spectrum of the adaptive reconstruction (---- object, — reconstruction).

Frequency components below the cut-off frequency are restored very well, noise is hardly to be seen in the imaging band and the noise outside the imaging band has been successfully depressed.

For comparison the moving-average adaptive reconstruction for $W=10$ is performed for two other object realizations as well, assuming the same noise variance of 0.345 K. The results are depicted in figures 6.10 and 6.11.

For both, the reconstruction error for the whole interval is approximately 0.5 K and for the shown interval it is approximately 0.9 K.

Apparently the adaptive filtering technique leads to very good results, independent of the object realization. The best feature of the adaptive filtering is that single events in the brightness temperature can be retrieved without problems.

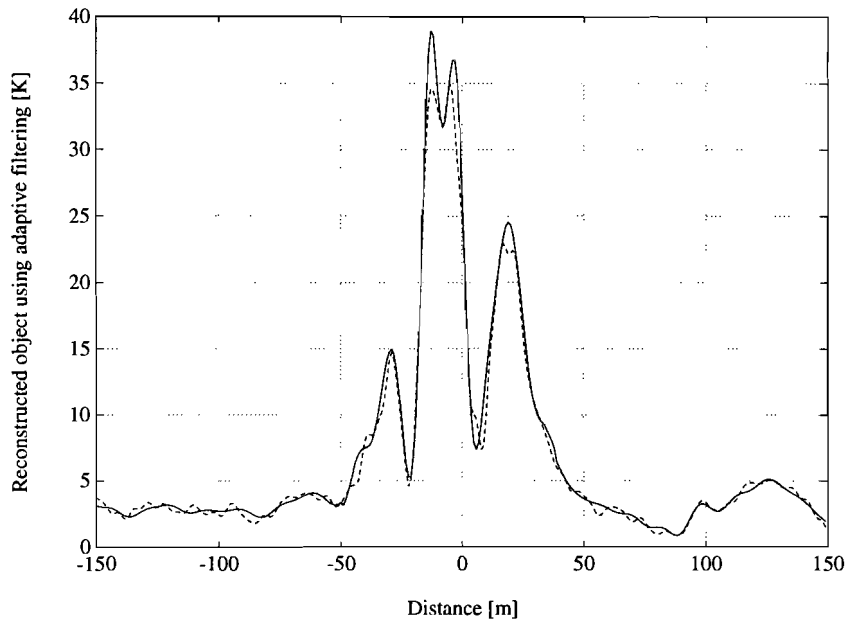


Figure 6.10 : The moving average adaptive reconstruction of another object (---- object, — reconstruction).

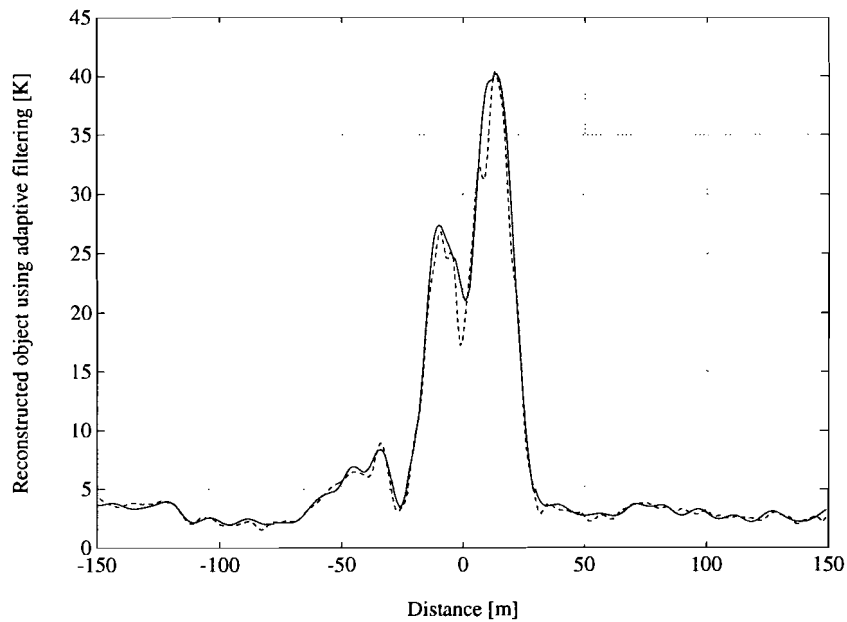


Figure 6.11 : The moving average adaptive reconstruction of another object (---- object, — reconstruction).

Chapter 7

Conclusions and Recommendations

A spatial filtering reconstruction technique has been presented to deconvolve the true atmospheric brightness temperature distribution over a cloudy sky out of the antenna noise temperature of the radiometer receiver.

The first conclusion that can be drawn is that frequency components above the antenna cut-off frequency cannot be retrieved, unless special extrapolation methods are used.

Inverse filtering seemed to be the most straightforward method to perform the deconvolution. It is shown that this will yield the best resolution, but that the resolution *gain* will be maximally two for the antenna used. This is not a spectacular gain, though.

The main limitation in attaining maximum reconstruction *accuracy* is the ever-present trade-off between noise suppression and resolution enhancement that has to be met.

For a worst case analysis, the first object chosen is an object with sharp edges (discontinuities), implying high-frequency content.

Inverse filtering is theoretically able to achieve the maximum *resolution* gain, but its noise regulation is very poor due to the in-band noise amplification and the rectangular overall filter.

The blurring of the image is also caused by sharp edges of the object, resulting in high-frequency content to be missing in the estimate.

The statistical method, Wiener filtering, results in a "smoothed" inverse filter, characterized by lower peaks and an overall filter with a roll-off which leads to a reconstruction that is not very much better yet, so it can be concluded that the blurring is mainly caused by the sharp edges of the object used.

The application of a sharpness constraint leads to a smoothed estimate, but at the expense of resolution. For objects like the one used this is the best method though.

The scalable trade-off between resolution enhancement and noise suppression of the Backus-Gilbert approach offers great flexibility in the Wiener reconstruction algorithm.

When a realistic, random, continuous object based on measurements is used, no constraint on the Wiener filter is necessary to make a good estimate of the object, thanks to the natural low-pass character of nature's phenomena.

The conversion of the designed Wiener filter to a real-time digital IIR filter has not been very successful due to the non-linear phase of this kind of filter in spite of its similarities. A FIR filter design leads to a negligible difference with the Wiener approach which means that real-time processing can be done without loss of quality in the reconstruction procedure.

A reconstruction error analysis shows that noise is *the* limiting factor in the striving for maximum restoring accuracy; it even causes the reconstruction error for an antenna used with double resolution to be higher for a range of SNR's than the error made by the standard antenna.

It can be concluded that Wiener filtering in general yields satisfying results in restoring the image, but the signal-to-noise ratio used causes ambiguity in single-event signals. This problem is taken care of by adaptive filtering: dividing the image in intervals and applying the filter corresponding to the interval's energy signal-to-noise ratio, or, more elegantly, by a moving average adaptive filter to achieve smooth transitions between two chosen filter tapsets. This yields very good results; the estimation of the object approximates the object very closely and discontinuities are completely removed by the moving average adaptive filter. The error made is such that the method is comparable to normal Wiener filtering with a SNR of 8 dB higher. Whatever the object will look like, this kind of deconvolution will always yield good results. It can therefore be concluded that this will be the only way to deconvolve radiometric imaging data with optimum resolution and accuracy when no information whatsoever about the object is present.

When the spatial frequencies of the object are of interest in the analysis of cloud structures and turbulences convolution *always* has to be applied to undo the effect of the "triangular" shape of the antenna transfer function.

For a accurate reconstruction of objects one has to be careful with the dependence of resolution and accuracy: it appeared that doubling the size of the antenna does *not* necessarily lead to a better reconstruction due to the in-band receiver noise. There is probably a relation between the optimum beamwidth (antenna size), which minimizes the reconstruction error, and the signal-to-noise ratio recieved; this will be a essential feature to investigate.

One of the problems in this kind of approach is that the altitude and the speed of the object have

to be known. This can be dodged by defining the imaging system in a spherical coordinate system and using two antenna beames to deduce the object speed from the correlation between the two received signals.

This completion can be a basis for the next step: the two-dimensional reconstruction. This can be done easily by using a two-dimensional Fourier transform approach, but the goal is on-line processing, so a FIR filter is to be designed that takes into account the overlap between antenna footprint and scanpath of the radiometer antenna.

In the very end, the two-dimensional reconstruction technique can then also be used for remote sensing and imaging of the earth's surface.

Chapter 8

References

- [1] Arai,I., M.Kazuhiko, K.Motomara, T.Suzuki, "Improvement in the spatial accuracy of the MOS-1 microwave scanning radiometer by signal processing",
Noise and clutter rejection in radars and imaging sensors, Proceedings of the 2nd International Symposium, Kyoto, Japan, 14-16 November 1989.
Ed. by Suzuki,T., H.Ogura, and S.Fujimora. Amsterdam: Elsevier Science Publishers,1990. P.341-346.
- [2] Arai,I., "Microwave remote sensing: On the effect of signal processing by inverse filter",
Navigation (Japan), Vol.107 (1991), p.65-70.
- [3] Arguello,R.J., H.R.Sellner, J.A.Stuller, "Transfer function compensation of sampled imagery",
IEEE Transactions on computers, vol.C-21 (1972), p.812-818.
- [4] Barnes,C.W., "Object restoration in a diffraction-limited imaging system", *Journal of the Optical Society of America*, vol.56 (1966), nr.5, p.575-578.
- [5] Basili,P., P.Ciotti, G.d'Auria, "Antenna corrections for increasing spatial resolution of microwave radiometric observation: synthetic antenna", *URSI International Symposium on electromagnetic theory, Part A*, Budapest, Hungary, 25-29 August 1986.
Ed. by Berceli,T.. Amsterdam: Elsevier,1986. P.168-170.
- [6] Basili,P., P.Ciotti, G. d'Auria, e.a., "Case study of intense scintillation events on the OTS path",
IEEE Transactions on Antennas and Propagation, vol.AP-38 (1990), no.1, p.107-113.

- [7] Bergland,G.D., "A guided tour of the fast Fourier transform", *IEEE Spectrum*, July 1969, p.41-51.
- [8] Bracewell,R.N., J.A.Roberts, "Aerial smoothing in radio astronomy", *Australian Journal of physics*, vol.7 (1957), p.615-670.
- [9] Buck,G.J., "Radar mapping: prolate spheroidal wave functions versus truncated inverse Fourier transforms", *IEEE Transactions on Antennas and Propagation*, vol. AP-20 (1972), no.2, p.188-193.
- [10] Buck,G.J., J.J.Gustincic, "Resolution limitations of a finite aperture", *IEEE Transactions on Antennas and Propagation*, vol. AP-15 (1967), no.3, p.376-381.
- [11] Ciotti,P., D. Solimimi, P.Basili, "Spectra of atmospheric variables as deduced from ground-based radiometry", *IEEE Transactions on Geoscience Electronics*, vol. GE-17 (1979), no. 3, p.86-77.
- [12] Considine,P.S., R.A.Gonsalves, "Optical image enhancement and image restoration", *Topics in Applied Physics*, vol.23: Optical data processing applications.
Ed. by Casasent,P.. Berlin: Springer-Verlag, 1978. P.53-65.
- [13] d'Auria,G., D.Solimini, "Effects of the atmosphere on image resolution in microwave radiometry", *Wave propagation and remote sensing; Proceedings of URSI Commission F Symposium*, Louvain, Belgium, 9-15 June 1983, ESA SP-194, p.2859-267.
- [14] Frieden,B.R., "Image enhancement and restoration", *Topics in Applied Physics*, vol.6: Picture processing and digital filtering.
Ed. by Huang,T.S.. Berlin: Springer-Verlag, 1975. P.177-247.
- [15] Frieden,B.R., "Information, and the restorability of images", *Journal of the Optical Society of America*, vol.60 (1970), p.575-576.
- [16] Frieden,B.R., "Band-unlimited reconstruction of optical objects and spectra", *Journal of the Optical Society of America*, vol.57 (1967), no.8, p.1013-1019.
- [17] Harris,F.J., "On the use of windows for harmonic analysis with the discete Fourier transform", *Proceedings of the IEEE*, vol.66 (1978), no.1, p.51-83.
- [18] Harris,J.L., "Diffraction and resolving power", *Journal of the Optical Society of America*, vol.54 (1964), no.7, p.931-936.

- [19] Harris,J.L., "Image evaluation and restoration", *Journal of the Optical Society of America*, vol.56 (1966), no.5, p.569-574.
- [20] Helstrom,C.W., "Image restoration by the method of least squares", *Journal of the Optical Society of America*, vol.57 (1967), no.3, p.297-303.
- [21] Huang,T.S., W.F.Schreiber, O.J.Tretiak, "Image Processing", *Proceedings of the IEEE*, vol.59 (1971), no.11, p.1586-1609.
- [22] Hughes,P., S.F.A.Ip, J.Cook, "Adaptive filters : a review of techniques", *British Telecom Journal*, vol.10 (1992), no.1, p.28-48.
- [23] Kusama,K., I.Arai, K.Motomura, M.Tsunoda, X.Wu,T.Suzuki, "Compression of radar beam by deconvolution", *Noise and clutter rejection in radars and imaging sensors, Proceedings of the 2nd International Symposium*, Kyoto, Japan, 14-16 November 1989.
Ed. by Suzuki,T., H.Ogura, and S.Fujimora. Amsterdam: Elsevier, 1990. P.767-772.
- [25] Maagt,P.J.I. de, H.G. ter Morsche, J.L.M. van den Broek, *A spatial reconstruction technique applicable to microwave radiometry*, EUT Report, 92-E-257, ISBN 90-6144-257-5, Eindhoven University of Technology, Faculty of Electrical Engineering, 1992.
- [26] Rhodes,D.R., "The optimum line source for the best mean-square approximation to a given radiation pattern", *IEEE Transactions on Antennas and Propagation*, Vol.AP-11 (1963), p.440-446.
- [27] Rino,C.L., "Bandlimited image reconstruction by linear mean-square estimation", *Journal of the Optical Society of America*, Vol.59 (1969), no.5, p.547-553.
- [28] Sam Shanmugam, K., *Digital and analog communication systems*.
New York: John Wiley and Sons, 1979.
- [29] Sezan,M.I., A.M.Tekalp, "Survey of recent developments in digital image restoration", *Optical Engineering*, Vol.29 (1990), no.5, p.393-404.
- [30] Slepian,D., H.O.Pollak, "Prolate spheroidal wave functions, Fourier analysis and uncertainty - I", *The Bell System Technical Journal*, Vol.40 (1961), p.43-63.
- [31] Srinisavan,R., "Destriping of Landsat data using power spectral filtering", *Proceedings of the SPIE International Society of Optical Engineering*, Vol.757: Methods of handling and processing imagery (1986), p.34-39.
- [32] Srinisavan,R., "Image restoration by spatial filter design", *Proceedings of the SPIE*

International Society of Optical Engineering, Vol.707: Visual communications and image processing (1986), p.193-197.

- [33] Wiener, N., *The extrapolation, interpolation and smoothing of stationary time series*. New York: John Wiley & Sons, 1949.
- [34] Little, J.N., L. Shure, *Signal Processing Toolbox for use with MATLABTM, User's Guide*, South Natick: The MathWorks, Inc., 1988.

Appendix A

Matrix Techniques

In Chapters 3 and 4 it is assumed that the measurement series are infinite to justify Fourier analysis. This is in general not the case, since the interest lies more in single events, which already has been briefly discussed in Chapter 2 when the energy content of a finite series was introduced.

If the minimized mean square error method is used in discrete data processing on finite time series, the best way is to use matrix techniques, since filters are implemented in a simple multiplicative way, like in the frequency domain method.

It can be expected of course that the results will be very similar to the results of the previous chapter.

A.1 Minimum variance estimation.

Figure A.1 on the next page represents the imaging system, but now in a discrete signal approach.

The indices of the signals have been omitted for convenience, they are all vectors.

The signals o and n are random processes, and g , h and c are linear filters (convolution operators).

These may be represented by general matrix operators for discrete finite time series.

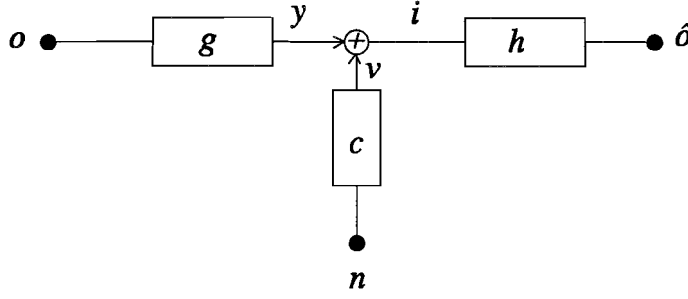


Figure A.1 : The imaging system in matrix approach.

The image i satisfies the following expression:

$$i = go + cn \quad (A.1)$$

Where

$i, y, v \in \mathbb{R}^M$: M measurements.
$o \in \mathbb{R}^N$: N object points.
$g \in \mathbb{R}^{M \times N}$: gain matrix
$c \in \mathbb{R}^{M \times K}$: noise filter
$n \in \mathbb{R}^K$: k noise observations.
$h \in \mathbb{R}^{N \times M}$: reconstruction filter.

The signals o , y , i , v and n are all column vectors.

The filter h provides an estimation of the object such that the autocorrelation matrix of the error between the object and the estimate is minimum:

$$\hat{o} = hi \quad (A.2)$$

In such a way that

$$\langle (o - \hat{o})(o - \hat{o})^T \rangle = \text{minimum} \quad (A.3)$$

This error equals

$$\begin{aligned} \langle oo^T - oo^T g^T h^T - on^T c^T h^T - hgoo^T - hcno^T + hgoo^T g^T h^T + hgon^T c^T h^T \\ + hcno^T g^T h^T + hcnn^T c^T h^T \rangle \end{aligned} \quad (A.4)$$

The process n is assumed to be zero-mean, random and uncorrelated with o .

Eq.(A.4) will then result in:

$$R_e = R_o - R_o^T h^T - h g R_o + h g R_o g^T h^T + h c R_n c^T h^T \quad (A.5)$$

The R 's in this equation are the autocorrelation matrices of the respective signals.

Differentiating Equation (A.5) to every term of h and h^T and setting the result to zero will lead to

$$h = R_o g^T (g R_o g^T + c R_n c^T)^{-1} = R_o g^T (g R_o g^T + R_v)^{-1} \quad (A.6)$$

This is the minimum-variance estimator.

If o and v are uncorrelated, random processes, their autocorrelation matrices will be identity matrices, scaled by their respective powers.

The minimum-variance estimator will then satisfy:

$$h = g^T (g g^T + \zeta I)^{-1} \quad (A.7)$$

The quantity ζ is the noise-to-signal ratio or the relative noise power.

Apparently, the minimum variance estimator is the Wiener solution, found in the previous chapter. This is very logical, because the same criteria are used and the filters are in both situations represented in a multiplicative form.

Eq.(A.6) may also be written as

$$h = (R_o^{-1} + g^T R_v^{-1} g)^{-1} g^T R_v^{-1} \quad (A.8)$$

If R_o^{-1} is very small, then the minimum-variance estimator reduces to

$$h = (g^T R_v^{-1} g)^{-1} g^T R_v^{-1} \quad (A.9)$$

This is the *maximum-likelihood estimator*, which is the *least-squares* solution of a system of linear equations.

The least-squares (maximum likelihood) estimator follows from the criterion

$$\langle (i - \hat{i})^T R_v^{-1} (i - \hat{i}) \rangle = \text{minimum} \quad (A.10)$$

This estimator is only good as a minimum-variance estimator for very high signal-to-noise ratios.

The error of the minimum-variance estimator is given by the covariance matrix

$$R_e = \langle (o - \hat{o})(o - \hat{o})^T \rangle = (R_o^{-1} + g^T R_v^{-1} g)^{-1} \quad (A.11)$$

For uncorrelated random processes o and v :

$$R_e = \epsilon^2 I^N = \sigma_o^2 (I^N + \frac{1}{\epsilon^2} g^T g)^{-1} \quad (A.12)$$

The general expression for the error in Eq.(A.11) is very similar to the expression for the spectrum of the error derived in Chapter 4:

$$\Phi_e(\omega) = \frac{\Phi_n(\omega)\Phi_o(\omega)}{|S(\omega)|^2\Phi_o(\omega) + \Phi_n(\omega)} = \frac{1}{|S(\omega)|^2\Phi_n^{-1}(\omega) + \Phi_o^{-1}(\omega)} \quad (A.13)$$

A.2 Analogy with the "de Maagt" method.

Another matrix method is the approach proposed by Ref.[25].

The solution of the inversion problem is a weighed sum of shifted radiation patterns:

$$\hat{T}(x) = \sum_{i=1}^N a_i G_i'(x) \quad (A.14)$$

The a_i 's form a vector \underline{a} , called the *innovation sequence*.

A matrix G is constructed from the shifted radiation patterns as follows:

$$G_{ij} = \frac{1}{4\pi} \int_{-\infty}^{\infty} G_i(x) G_j(x) dx \quad (A.15)$$

The matrix G is apparently a self-convolution of the radiation pattern.

The eigenvalues of the matrix G are given by the set $\lambda_1, \lambda_2, \dots, \lambda_N$, and the eigenvectors of G by the set $\underline{e}_1, \underline{e}_2, \dots, \underline{e}_N$.

The aim is to minimize the mean square error between the image, the antenna temperature T_a and the estimated image, which is the estimated object convolved again with the antenna pattern.

It is shown that this criterion can be translated to:

$$||G\underline{a} - \underline{T}_a||^2 = \epsilon^2 \quad (A.16)$$

where ϵ is the radiometer temperature resolution or the radiometer sensitivity mentioned earlier in Chapter 3.

The vectors \underline{a} and \underline{T}_a are decomposed into the eigenvectors of the matrix G :

$$\underline{a} = \sum_{i=1}^N \xi_i \underline{e}_i \quad \text{and} \quad \underline{T}_a = \sum_{i=1}^N \tau_{ai} \underline{e}_i \quad (\text{A.17})$$

The solution of the criterion, the vector \underline{a} , is calculated to be

$$\underline{a} = \sum_{i=1}^N \frac{-\alpha \tau_{ai}}{(1 - \alpha \lambda_i)} \underline{e}_i = \sum_{i=1}^N \frac{\beta \tau_{ai}}{(1 + \beta \lambda_i)} \underline{e}_i \quad (\text{A.18})$$

The β can be found by solving the following equation:

$$\sum_{i=1}^N \left(\frac{\tau_{ai}}{1 + \beta \lambda_i} \right)^2 = \epsilon^2 \quad (\text{A.19})$$

For a very high β the vector \underline{a} equals

$$\underline{a} = \sum_{i=1}^N \frac{\tau_{ai}}{\lambda_i} \underline{e}_i = G^{-1} \underline{T}_a \quad (\text{A.20})$$

The matrix G stands for double filtering with the radiation pattern G' so the solution is according to Eq.(A.14) is (in illustrative notation) $G'/(G' G') = 1/G'$, which is just inverse filtering.

The question soon arises what the correspondence is between this reconstruction technique and the Wiener filtering method and which role β and the signal-to-noise ratio ζ play in it.

The vector \underline{a} can be interpreted as a sampled version of an image $a(x)$ and the $G'_i(x)$ are nothing more than shifted versions of $G'(x)$ so Eq.(A.14) is a discrete convolution, which can be written continuously as follows:

$$\hat{T}(x) = \int_{-\infty}^{\infty} a(\xi) G'(x - \xi) d\xi \quad (\text{A.21})$$

Again using the same notation as mentioned before, Eq.(A.21) will be:

$$\hat{o}(x) = \int_{-\infty}^{\infty} a(\xi) s(x - \xi) d\xi \quad (\text{A.22})$$

Thus, the last block in the overall system will be the same as the first: the antenna transfer function.

What remains to be found is the prefilter after the antenna. Its output signal $a(x)$ is given by Eq.(A.18).

Two things can be observed from this expression. Firstly, the resemblance to a feedback filter, and secondly, the even stronger resemblance to the Wiener filter, which is given by

$$H_w(\omega) = \frac{S^*(\omega)}{|S(\omega)|^2 + \Phi_n(\omega)/\Phi_o(\omega)} \quad (\text{A.23})$$

The overall system can then be depicted as in figure A.2.

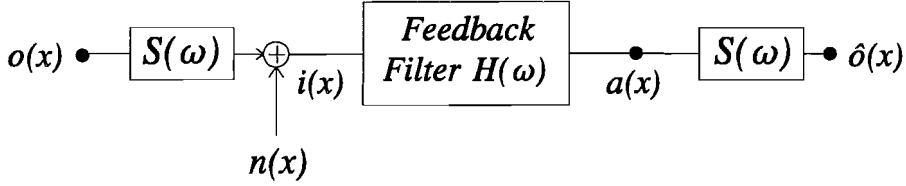


Figure A.2 : The overall imaging system.

The feedback filter $H(\omega)$ will consist of a gain ζ to regulate the noise reduction as β does in Eq.(A.18) and a filter $|S(\omega)|^2$ in the feedback loop to compensate for the double antenna transfer function in such a way that when ζ approaches infinity the overall transfer will be unity, conform to perfect inverse filtering. The feedback filter is the optimum filter for normal Wiener filtering when both noise and object are considered white ($\Phi_o(\omega)/\Phi_n(\omega)=\zeta$).

A feedback filter that satisfies these demands is the filter depicted in figure A.3.

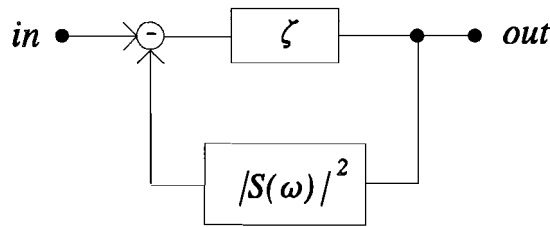


Figure A.3 : The noise regulating feedback filter.

The transfer function of this filter is

$$H(\omega) = \frac{\zeta}{1 + \zeta |S(\omega)|^2} = \frac{1}{\zeta^{-1} + |S(\omega)|^2} \quad (\text{A.24})$$

The analogy with frequency domain Wiener can be seen very clearly in the innovation sequence $a(x)$. In the Fourier analysis $a(x)$ is according to figure A.3 and Eq.(A.24) given by

$$a(x) = \frac{1}{2\pi} \int_{-\infty}^{\infty} \frac{I(\omega)}{\zeta^{-1} + |S(\omega)|^2} e^{j\omega x} d\omega \quad (A.25)$$

The matrix approach results in a vector \underline{a} , given by

$$\underline{a} = \sum_{i=1}^N \frac{\tau_{ai}}{\beta^{-1} + \lambda_i} \underline{e}_i \quad (A.26)$$

Apparently the two methods are completely equivalent since the τ_{ai} 's represent the image as in Eq.(A.17) and the λ_i 's represent the squared antenna filter as in Eq.(A.15), with β being equal to the signal-to-noise ratio ζ .

The total imaging filter transfer thus will be

$$H_{im}(\omega) = \frac{S(\omega)}{\zeta^{-1} + |S(\omega)|^2} \quad (A.27)$$

The antenna pattern $s(x)$ is even so its Fourier transform $S(\omega)$ will be real. Equation (4.19) can then be written as follows:

$$H_{im}(\omega) = \frac{S^*(\omega)}{|S(\omega)|^2 + \zeta^{-1}} \quad (A.28)$$

This completes the equivalence of the two methods.

The difference is illustrated in figure A.4.

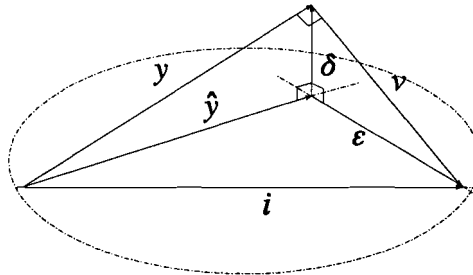


Figure A.4 : The imaging quantities in vector notation.

The depicted quantities are the same quantities as in figure A.1.

The estimated image \hat{y} is the projection of y on the image plane and, as already stated in Chapter 3, for a correct estimated SNR the difference between the two is uncorrelated with \hat{y} . The error caused by noise in this estimation is the projection of v on the image plane.

The image y is of course not correlated with the noise v .

Figure A.4 shows that the error ε between image and estimated image (analyzed in Chapter 3) is smaller or equal to the radiometer error (noise) v , while Ref.[25] assumes that $|\varepsilon| = |v|$.

This can also be seen from figure 4.10 in Chapter 4, which represents the error transfer function which, multiplied by the image Fourier transform, yields the error ε . This filter acts as a high-pass filter, removing all frequency components in the image band, so what is left is just the noise v , since it is the only signal in the image possessing frequency components above the cut-off frequency, stripped of its frequencies in the image band. The power of this error is therefore smaller than the noise power.